Clays and Clay Minerals, Vol. 62, No. 2, 89–101, 2014.

TEMPERATURE EFFECTS ON THE CRYSTALLINITY OF SYNTHETIC NONTRONITE AND IMPLICATIONS FOR NONTRONITE FORMATION IN COLUMBIA RIVER BASALTS

LESLIE L. BAKER[1,2,]* AND DANIEL G. STRAWN[2]

[1] Department of Geological Sciences, University of Idaho, Moscow, ID 83844-3022, USA
[2] Department of Plant, Soil, and Entomological Sciences, University of Idaho, Moscow, ID 83844-2339, USA

Abstract—The formation conditions of the ferric smectite nontronite are not fully understood. The present study couples experimental and analytical data with field observations in an attempt to constrain the rate and temperature of formation of naturally occurring nontronites from Columbia River Basalt flows. Synthetic Fe-Al-Si gels were incubated at temperatures ranging from 4 to 150ºC for 4 weeks. Samples were analyzed using Fe K-edge X-ray fluorescence spectroscopy (XAFS). Spectra of the synthesized nontronites were compared with spectra of natural samples collected from weathered Columbia River Basalt flows. Cation ordering in the synthetic samples increased with incubation temperature, but the synthetic clays did not approach the degree of crystal ordering of the natural nontronite samples. These observations suggest that highly ordered natural nontronites require longer crystallization times than are typically used in laboratory experiments. The natural samples were found filling open cracks near flow surfaces, indicating that the clays formed at temperatures below the boiling point of water. A comparison of experimental and field timescales with other estimates of nontronite growth rates suggests that natural nontronite crystallization in the region must have occurred at ambient, near-surface temperatures over timescales of up to millions of years.

Key Words—Columbia River Basalts, Fe K-edge XAFS, Nontronite.

INTRODUCTION

Nontronite is a dioctahedral ferric smectite with an ideal mineral formula of $Na_{0.4}Si_{3.6}Al_{0.4}Fe_2O_{10}(OH)_2$. In nature it is most commonly found as a weathering product of mafic volcanic rocks such as basalt (Allen and Scheid, 1946; Benson and Teague, 1982; Jakobsson and Moore, 1986; Meunier *et al.*, 2008), but is also observed in metamorphic rocks (Eggleton, 1977; Keeling *et al.*, 2000) and in sediments associated with seafloor hydrothermal vents (Cole and Shaw, 1983; Köhler *et al.*, 1994; Ueshima and Tazaki, 2001; Severmann *et al.*, 2004; Dekov *et al.*, 2007). Nontronite has been identified as a potentially important phase on Mars, where its presence in deep canyons provides direct evidence for aqueous alteration of Martian crustal rocks in the ancient past (Bishop *et al.*, 2008; Ehlmann *et al.*, 2011). Natural nontronites range from nearly pure Fe endmember phases to mixed Fe-Al phases that are sometimes described as ferruginous smectites. Whatever their composition, most well studied natural nontronites are comparable to one another in terms of their crystallinity (Allen and Scheid, 1946; Manceau *et al.*, 1998; Gates *et al.*, 2002). Although nontronite occurrence and properties are well documented, the formation conditions of this clay mineral are not well understood.

To study nontronite formation and properties, the mineral has been synthesized in the laboratory using various methods. Ferric smectites were synthesized (Harder, 1976, 1978) by aging co-precipitates of ferrous hydroxides and silica at 3−22ºC. The formation of ferric smectites was observed only (Harder, 1976, 1978) from starting products containing Fe(II) and aged in the presence of sodium dithionite, a reductant. Under these conditions, synthetic products that had XRD peaks indicative of clay minerals after synthesis times as short as 2 weeks were described, although the clays were described as being very poorly crystalline. Harder (1976, 1978) also noted that the formation of Fe-rich clay minerals was promoted by synthesis at pH > 7, and that nontronite formed in solutions with Fe:Si between 1:10 and 1:3. These synthesis conditions are similar to conditions observed for nontronite formation in seafloor hydrothermal sediments, where ferric hydroxide-silica co-precipitates recrystallize to nontronite (Cole and Shaw, 1983; Köhler *et al.*, 1994; Ueshima and Tazaki, 2001; Severmann *et al.*, 2004).

Aluminous nontronites were also synthesized by Farmer *et al.* (1991, 1994) at 23 and 89ºC and pH 8, from solutions of $AlCl_3$, $FeCl_2$, and silicic acid. Those authors obtained poorly ordered, hisingerite-like materials at the lower temperature, but at the higher temperature, ordered nontronitic layer silicates were

---

* E-mail address of corresponding author:
lbaker@uidaho.edu
DOI: 10.1346/CCMN.2014.0620202

formed after 8 weeks. Natural nontronites were proposed by Farmer *et al*. (1991, 1994) to form by initial precipitation of a trioctahedral Fe(II) silicate, which transforms to dioctahedral nontronite through oxidation of Fe and ejection of excess octahedral cations, but they noted that crystallization in their experimental systems occurred primarily after oxidation of Fe(II) to Fe(III).

Synthesis of ferric smectites from gels under reducing and oxidizing conditions, were investigated by Decarreau and Bonnin (1986) and Decarreau *et al.* (1987), respectively. In contrast to the results of Harder (1976, 1978), those authors observed growth of ferric smectites only under oxidizing conditions. Decarreau and colleagues also observed smectite growth to be very slow except at elevated temperatures. From measurements of crystal growth at several temperatures, they derived an Arrhenius relationship for nontronite formation, indicating that a ferric smectite with coherent domains ~100 Å in size should form in ~10 y at 25ºC and in ~200 years at 2ºC. Decarreau *et al.* (2008) extended these methods to synthesize high-charge Fe-endmember nontronites. Clays synthesized by those authors displayed a high level of tetrahedral Fe substitution, estimated at 30% of total Fe. The crystallinity of the synthetic nontronites increased with increasing temperature up to 150ºC, above which aegirine ($NaFeSi_2O_6$) formed rather than nontronite.

Previous experimental studies on nontronite synthesis have provided insight into conditions required for nontronite formation, but many questions remain. Application of these studies to nontronite formation from mafic precursors suggests that the formation of highly crystalline nontronites in nature may require long formation times at relatively low temperatures. The present study further investigated this hypothesis by examining the crystallinity of a set of synthetic nontronites incubated at 23, 95, and 150ºC. Poorly crystalline phases are often difficult to study using techniques such as XRD. In the present study, synthetic nontronites were analyzed using Fe K-edge XANES and EXAFS methods, which provide information on the shells of atoms immediately surrounding a central iron atom and, therefore, allow for insights into the molecular structure of nontronite samples that have limited (XRD-amorphous) structure. The XAFS spectra from synthetic samples were compared to spectra of natural nontronite samples formed by weathering of Columbia River Basalts (CRB). These data on the relative crystallinities of the synthetic and natural samples, coupled with field constraints on natural nontronite occurrences, help to constrain the physical parameters of nontronite formation by basalt weathering.

METHODS

Natural and synthetic sample acquisition/preparation

A single batch of nontronite precursor gel was synthesized using a method modified from the nontronite-synthesis procedures of Farmer *et al.* (1994) and Decarreau and Bonnin (1986), and the allophane-synthesis procedure of Montarges-Pelletier *et al.* (2005). This gel had an Fe:Al molar ratio of 1:1 and a Si:(Fe,Al) molar ratio of 3:1. To synthesize the precursor material, 0.1 M $Fe(NO_3)_2$ and 0.1 M $Al(NO_3)_3$ were mixed with tetraethyl orthosilicate and one drop of hydrazine, and stirred rapidly on a magnetic stir plate. A solution of 0.1 M NaOH was titrated into the solution at a rate of 1 mL min^{-1} under rapid stirring, forming a dark blue-green gel. The final pH of this gel suspension was 7.6 after titration. The suspension was adjusted to pH 12.25 with 1 M NaOH. The gel was then separated into aliquots for further incubation at different temperatures.

All samples were incubated for a period of 28 days. One aliquot of the initial gel (nontronite 1) was washed twice in deionized water and stored under refrigeration at 4ºC, and remained a dark green gel. A second aliquot (nontronite 2) was incubated under stirring at room temperature (23ºC); the final product was a suspension of brown gel with a final pH of 11.37. A third aliquot (nontronite 3) was incubated at 95ºC on a temperature-controlled stirring hot plate and turned to a thick, tan suspension with a final pH of 10.64. A fourth aliquot (nontronite 4) was incubated at 150ºC in a Teflon cup inside a stainless steel bolted-closure autoclave in the presence of liquid water, and remained a dark blue-green color; its final pH was not measured. At the end of the 28-day incubation period, all samples were stored under refrigeration. A small amount of each synthetic nontronite was dried for analysis. The dried synthetic nontronites were all light tan in color.

Naturally occurring nontronitic clays were collected near the towns of Garfield and Trinidad in the state of Washington, USA. These sites were the original collection localities for the widely used but now commercially unavailable reference standards, Garfield nontronite (API#33a, formerly available from Wards Natural Science, Rochester, New York, USA) and SWa-1 ferruginous smectite (formerly available from the Source Clays Repository of The Clay Minerals Society). Nontronite from Garfield was collected from the sampling location described by Kerr and Kulp (1949). Green, waxy nontronite was found filling narrow (~1 cm) cracks in the Priest Rapids Member of the Wanapum Basalt of the Columbia River Basalt Group (Reidel *et al.*, 2013). This is the capping basalt in this locality and the nontronite-filled cracks were located within 1 m of the basalt surface. This sample is designated as UI-Garfield here to distinguish it from the original Garfield nontronite.

The site at Trinidad, from which the original SWa-1 sample was collected, is located on Washington State Highway 28 just east of the town of Trinidad and was described in the field notes and maps of J.A. Kittrick that are archived in the Department of Crop and Soil Sciences, Washington State University and available from the journal's data depository: www.clays.org/JOURNAL/JournalDeposits.html. The nontronite at this locality formed at the contact between a basalt flow of the Frenchman Springs Member of the Wanapum Basalt of the Columbia River Basalt Group and an underlying paleosol developed on underlying Grand Ronde Basalt (Reidel *et al.*, 2013). The Frenchman Springs flow is the capping basalt at this locality, and green, powdery clays were found filling void spaces and coating altered basalt fragments located ~2 m beneath the flow surface.

Once collected, the nontronite samples were crushed gently by hand using an agate mortar and pestle and suspended in deionized water, and the very fine clay fraction (<0.05 µm) was separated by centrifugation. The separated clay fraction was analyzed as described below, without further purification.

Laboratory analyses

The dried nontronite samples were analyzed using diffuse reflectance Fourier-transform infrared spectroscopy (FTIR) and powder X-ray diffractometry (XRD). The FTIR analyses were carried out on a Perkin-Elmer System 2000 (Thermo Scientific, Waltham, Massachusetts, USA), using a mixture of 3 wt.% nontronite in optical-grade KBr. Spectra were processed using the Kubelka-Munk algorithm provided in the Perkin Elmer *Spectrum* 2.0 software (Thermo Scientific, Waltham, Massachusetts, USA). The XRD scans were run on a Siemens D5000 diffractometer (Bruker AXS, Karlsruhe, Germany) and data were analyzed using the *Diffracplus Eva* evaluation program (Bruker AXS, Karlsruhe, Germany). Natural clay samples were fused with lithium metaborate and analyzed on a Thermo Electron iCAP inductively coupled plasma spectrometer (ICP-AES) (Thermo Scientific, Waltham, Massachusetts, USA) for bulk composition (results are shown in Table 1).

Bulk Fe K-edge XAFS data for synthetic and natural nontronite samples were collected on Beamline 7-3 of the Stanford Synchrotron Radiation Laboratory (SSRL). The monochromator for this beamline consisted of two parallel Si(220) crystals with a 6-mm entrance slit. All samples were run in a liquid He-cooled cryostat at a temperature of 7 K. Fluorescence data were collected using a PIPS detector. Step size through the XANES region was 0.35 eV. Powdered samples were smeared on filter paper, which was cut into strips, stacked three layers thick, and sealed in the sample holder with Kapton tape. The synthetic nontronites incubated at 95 and 23ºC were analyzed as gels, which were packed into the sample holder in a layer of uniform thickness and sealed with Kapton tape. Both transmission and fluorescence spectra were collected for all samples; fluorescence spectra were used for all samples because of their higher signal to noise ratio, but the two datasets were comparable and fluorescence data did not show any self-absorption artifacts.

One to three XAFS scans per sample were calibrated to Fe foil and averaged using the program *SixPack* (Webb, 2005). Processing and shell fitting were carried out using the programs *Athena* and *Artemis* (Ravel and Newville, 2005). Raw and normalized intensity data were exported into the plotting program *Origin* 8.6 (OriginLab, Northampton, Massachusetts, USA). Pre-edge peaks were fitted in *Origin*; a spline was fitted to each baseline between 7110 and 7120 eV and subtracted, after which peak locations were identified and peak heights were measured.

Shell fitting of the XAFS spectra was carried out using the 6-shell model described by Baker and Strawn (2012), as modified from a nontronite model described by Manceau *et al.* (1998). The model parameters are given in Table 2. All parameters were set, and fitting was carried out, as described for UI-Garfield nontronite in Baker and Strawn (2012). Briefly, fitting was carried out using backscattering paths to first-shell oxygen, Fe, and Al in the octahedral sheet and six associated oxygen atoms (O3), and Si in the tetrahedral sheet and two associated O atoms (O2). All backscattering path lengths were optimized. To account for possible non-random distribution of octahedral cations, the Fe-Fe and Fe-Al backscattering paths were weighted with parameters that were constrained to sum to three (*e.g.* three total neighboring octahedral cations), and this parameter value was optimized (*N*Fe; Table 2). Debye-Waller parameters were optimized for the first shell and the outer O shells (O2 and O3 paths), and fixed for the octahedral and tetrahedral cation backscattering paths, as

Table 1. Sample compositions of two natural nontronites (purified clay separates) and nominal (as synthesized) composition of synthetic nontronite. Oxide contents are given in weight percent.

	SiO_2	Al_2O_3	Fe_2O_3	MgO	CaO
UI-Garfield	56.3	5.35	35.64	1.39	0.57
Trinidad	57.2	5.39	34.26	1.47	1.69
Nominal synthetic	57.9	16.39	25.67	0	0
Standard Garfield*	51.7	7.54	36.43	0.16	3.52
Standard SWa-1*	56.7	11.04	26.65	1.302	3.16

* from Gates *et al.* (2002).

Table 2. Theoretical paths, coordination numbers, and path lengths for smectite used for shell modeling generated using *Feff*, as described by Baker and Strawn (2012). In fitting, Fe and Al coordination numbers were optimized, but constrained to sum to a total of 3 octahedral cations (*N*Fe is the number of Fe atoms in the structure, less than or equal to three).

Path	CN	R (Å)
Fe–O1	6	1.96–2.04
Fe–Fe1	*N*Fe	3.05
Fe–Al1	3–*N*Fe	3.05
Fe–Si	4	3.26
Fe–O2	2	3.45
Fe–O3	6	3.74–3.82

shown in Table 3.

ANALYTICAL RESULTS

Bulk analyses

Bulk chemical analyses for the UI-Garfield and Trinidad samples (Table 1) revealed compositions typical of nontronites, but different from published analyses of the standard samples from those localities. The analyzed composition of the Trinidad nontronite contained less Al_2O_3 and more Fe_2O_3 than published analyses of the SWa-1 standard that was collected from the same site. The analyzed composition of UI-Garfield nontronite contained more SiO_2, more MgO, and less Al_2O_3 than published analyses of the commercial Garfield nontronite standard. These differences may result from varying composition of the nontronite itself; although the samples in this study were collected from the same outcrops as the standard clays, specific collection sites (individual veins) were unknown and probably differed. Some compositional differences could potentially also result from differences in sample preparation. In this study, as in the study by Gates *et al.* (2002), very fine clay separates were physically separated for analysis in an effort to remove all Fe (oxyhydr)oxides. A slight excess of analyzed SiO_2 in the natural samples (Table 1) may indicate the presence of minor opaline silica. The synthetic nontronites were not analyzed independently due to the small quantity of material available; the composition shown for these samples in Table 1 is the nominal composition expected from the synthesis. As a result of the solution compositions used to synthesize the precursor gels, Na is expected to be the only interlayer cation present.

XRD

The XRD data (Figure 1) showed that none of the synthetic nontronites had achieved the crystallinity of the natural UI-Garfield nontronite sample. The synthetic nontronite incubated at 150ºC displayed reflections at *d* spacings typical of nontronite, with the 001 reflection at 11.8 Å, a peak at 3.8 Å, and inflections at 2.7 and 2.2 Å. These peaks were much less well defined than in the UI-Garfield nontronite. The synthetic nontronite incubated at 95ºC showed little XRD-detectable structure; a minor inflection at the 001 band at 11.8 Å and another at 3.8 Å were present, but much of this material appeared to be amorphous at the scale sensed by XRD. This material appeared to be less crystalline than the nontronite synthesized by Decarreau *et al.* (2008) at 90ºC, and more comparable to their 75ºC sample. No structure was detectable by XRD in the lower-temperature samples (not shown).

FTIR

In agreement with XRD analyses, FTIR data (Figure 2) also showed that none of the synthetic nontronites approached the structural development of either UI-Garfield or Trinidad nontronite. The UI-Garfield sample displayed typical nontronite IR peaks including the Fe–Fe–OH-stretching peak at 3565 cm^{-1}, the main Fe–Si–O stretch near 1005 cm^{-1}, Fe–Fe–OH

Table 3. Fitting results for nontronite samples. All path lengths were optimized independently unless otherwise noted; other variables optimized in fitting are annotated.

Path	UI-Garfield			Trinidad			150ºC synthetic			95ºC synthetic			23ºC synthetic		
	E0 = –1.98			E0 = –1.16			E0 = –3.46			E0 = –3.66			E0 = –4.63		
	R-factor = 0.025			R-factor = 0.024			R-factor = 0.015			R-factor = 0.012			R-factor = 0.027		
	CN	*R* (Å)	σ^2 ($Å^2$)	CN	*R* (Å)	σ^2 ($Å^2$)	CN	*R* (Å)	σ^2 ($Å^2$)	CN	*R* (Å)	σ^2 ($Å^2$)	CN	*R* (Å)	σ^2 ($Å^2$)
Fe–O1	6	2.00	0.006[a]	6	2.00	0.006[a]	6	1.99	0.009[a]	6	1.97	0.009[a]	6	1.96	0.012[a]
Fe–Fe1	3	3.08	0.005	2.48[a]	3.07	0.005	2.05[a]	3.05	0.005	1.66[a]	3.04	0.005	0.88[a]	2.88	0.005
Fe–Al1	0	–	–	0.52[a]	3.01	0.005	0.95[a]	3.05	0.005	1.34[a]	3.03	0.005	2.12[a]	2.92	0.005
Fe–Si1	4	3.23	0.005	4	3.24	0.005	4	3.26	0.005	4	3.26	0.005	4	3.23	0.005
Fe–O2	2	3.42	0.008[b]	2	3.33	0.009[b]	2	3.45	0.008[b]	2	3.46	0.028[b]	2	3.23	0.010[b]
Fe–O3	6	3.80	0.008[b]	6	3.80	0.009[b]	6	3.74	0.008[b]	6	3.81	0.028[b]	6	3.59	0.010[b]

[a] Values optimized in fitting

[b] Values optimized in fitting, but constrained to be equal to one another.

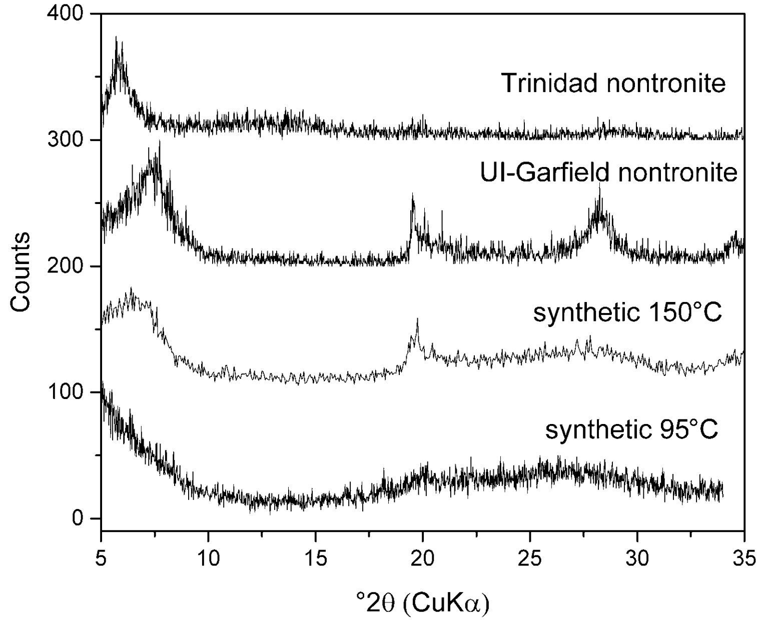

Figure 1. Bulk-powder XRD patterns of UI-Garfield and Trinidad nontronites, and of nontronites synthesized at 95 and 150ºC. Nontronites synthesized at lower temperatures showed no identifiable XRD peaks.

bending feature at 818 cm^{-1}, and Si−O−Fe bending vibration at 675 cm^{-1} (Frost *et al.*, 2002; Gates, 2005). In Fe-substituted smectites, an Fe−Al−OH stretching peak is observed at 3590 cm^{-1} (Frost *et al.*, 2002), and an Fe−Al−OH bend that is present at 890 cm^{-1} in higher-Al clays shifts to 870 cm^{-1} with increasing Fe content (Russell and Fraser, 1994). The latter band was observed in the spectrum of the Trinidad nontronite, but not in the spectrum of the UI-Garfield nontronite (Figure 2). Because the two clay samples had similar bulk composition (Table 1), this suggests a difference in cation ordering between them, with more Fe-Al nearest neighbors being present in Trinidad nontronite than in UI-Garfield nontronite. A band at 844 cm^{-1} was also observed in UI-Garfield nontronite; the presence of this band in combination with the 818 cm^{-1} band is considered diagnostic of nontronite (Gates, 2005; Gates, 2008). This band may arise from Fe-Fe−OH

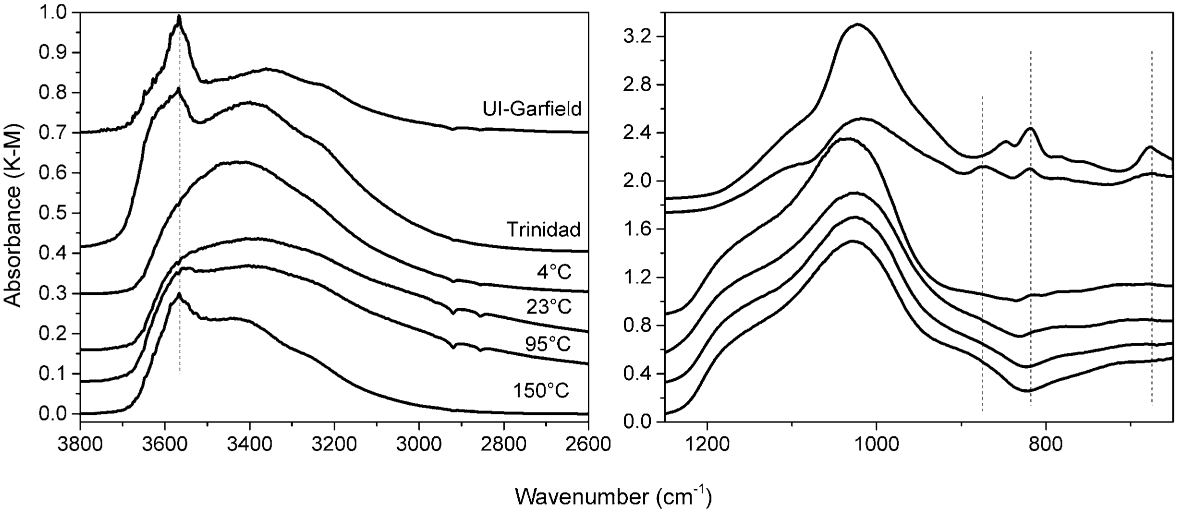

Figure 2. IR spectra of UI-Garfield nontronite and of nontronites crystallized at the temperatures indicated. The locations of characteristic nontronite peaks are indicated by dotted lines at 3565 cm^{-1} (Fe-Fe-OH-stretch), 870 cm^{-1} (Fe−Al−OH bend), 818 cm^{-1} (Fe−Fe−OH bend), and 675 cm^{-1} (Fe−O out of plane vibration). The shoulder near 1100 cm^{-1} in the UI-Garfield and Trinidad samples suggests the presence of amorphous or opaline silica in the sample (Shoji *et al.*, 1993).

bending, like the feature at 818 cm^{-1} (Frost *et al.*, 2002), perhaps due to splitting as a result of tetrahedral Fe substitution (Gates, 2008). A number of the characteristic spectral bands of nontronite or ferruginous smectites are shifted by the presence of Fe(II) in the structure (Neumann *et al.*, 2011). No such characteristic shifts were observed for the synthetic nontronites in the present study, in spite of evidence (discussed below) for some Fe(II) in the sample incubated at 150ºC. A broad shoulder centered near 1100 cm^{-1} in both the UI-Garfield and Trinidad samples suggested the presence of some amorphous or opaline silica (Shoji *et al.*, 1993), in agreement with the high SiO_2 measured for these samples. Opal is a common weathering product of Columbia River Basalts and macroscopic opal deposits were observed at the Trinidad field site, although not at the Garfield site.

The FTIR spectrum of the nontronite incubated at 150ºC was very similar to that of the 150ºC synthetic nontronite of Decarreau *et al.* (1987). Inflections at 844 and 818 cm^{-1} correspond to Fe–Fe–OH bending that are characteristic of nontronite (Gates, 2005; Gates, 2008). A band at 870 cm^{-1} suggests Fe–Al–OH bending, as would be expected for this high-Al composition. All the peaks in the 150ºC sample were weaker and broader than those observed in the natural nontronite samples, indicating a lower overall degree of crystallinity. The broadening and eventual disappearance of characteristic spectral lines in the nontronites synthesized at lower temperatures suggest that they were less crystalline than the nontronites synthesized at higher temperatures. The 95ºC nontronite displayed only a poorly developed Fe–Fe–OH stretching peak at ~3555 cm^{-1}, and an Fe–Si–O stretching peak near 1025 cm^{-1}. The Fe–Si–O stretch was the only one well developed in lower-temperature sample spectra. All the synthetic samples displayed a broad, very weak inflection near 870 cm^{-1} that may have arisen from Fe–Al–OH bending.

XANES pre-edge

The XANES spectra of natural nontronites were very similar to one another (Figure 3), except for a split pre-edge peak in the UI-Garfield nontronite that was not observed for the Trinidad nontronite. This peak splitting is typical of octahedrally coordinated high-spin Fe(III) in a relatively undistorted environment (Westre *et al.*, 1997). The amplitude and shape of the Fe K-edge XANES pre-edge peak arise from the local symmetry environment around the central Fe atom, which is influenced both by the presence of tetrahedrally coordinated Fe and by isomorphic substitution of other cations such as Al- or Mg-for-Fe in surrounding sites. According to Gates *et al.* (2002), the SWa-1 standard nontronite (from the same site as the Trinidad sample) contains no tetrahedral Fe. The Trinidad nontronite had similar Al and Mg content as the UI-Garfield nontronite (Table 1) although, as discussed above, its IR spectrum indicated more Fe–Al–O bonding (Figure 2). The increased distortion around the central Fe atom in the Trinidad sample indicated by the unsplit pre-edge peak may be explained by a difference in cation ordering between this sample and the UI-Garfield sample.

The pre-edge peaks in the XANES spectra of synthetic nontronites are not split. In addition, the peak amplitudes of the pre-edge peak in nontronites synthesized at 95ºC and 23ºC were greater than that in the sample synthesized at 150ºC. As with the Trinidad nontronite, the high Al content of the synthetic samples may account for the absence of splitting in the pre-edge

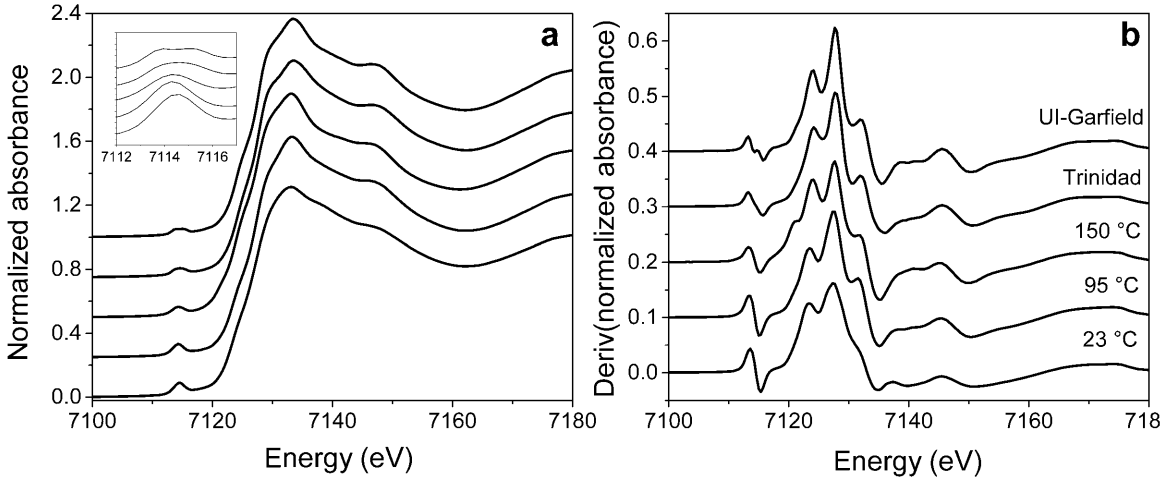

Figure 3. Normalized (a) and first-derivative (b) XANES spectra of UI-Garfield and Trinidad nontronites, and of synthetic nontronites crystallized at 23, 95, and 150ºC. The inset in (a) shows the pre-edge region of the XANES spectrum. The arrow in (b) indicates a low-energy shoulder on the synthetic 150ºC sample discussed in the text. Spectra are offset for clarity. The sample incubated at 4ºC is not shown, but is identical to that at 23ºC.

peaks. The increased pre-edge peak amplitude of the lower-temperature samples may result from the presence of tetrahedrally coordinated Fe (Westre *et al.*, 1997), or from distortion due to a high octahedral Al content (Manceau *et al.*, 1990).

These explanations can be evaluated by examining Fourier-filtered first-shell spectra. Detection limits for tetrahedral Fe are ~3% of total Fe (Manceau *et al.*, 1990; Gates *et al.*, 2002). If tetrahedral Fe is present, the first-shell spectrum will include contributions from the shorter Fe−O bonds in tetrahedral complexes, and the backscattered wave will be out of phase with waves from Fe in purely octahedral coordination, creating a slight shift in the peak positions. Back-transformed spectra of the 95ºC and 23ºC synthetic nontronites (Figure 4) were shifted slightly at high energy relative to spectra of the Trinidad and UI-Garfield nontronites, which do not contain significant tetrahedral Fe (Gates *et al.*, 2002). This suggests that some tetrahedral Fe was present in the lower-temperature synthetic nontronites. The filtered spectrum of the 150ºC synthetic nontronite was in phase with the Trinidad and UI-Garfield nontronite spectra, suggesting that little tetrahedral Fe is present in this sample. These observations suggest that the increased amplitude of the XANES pre-edge peaks for the low-temperature nontronite samples results from the presence of tetrahedrally coordinated Fe in these samples. However, the high Al content of the synthetic samples is probably contributing to their pre-edge peak amplitudes also.

XANES

The main-edge XANES spectra of the synthetic nontronites were similar to those of natural nontronites from Garfield and Trinidad. The 150ºC sample had an extra edge inflection at 7120 eV (arrow in Figure 3b) that was not present in the natural samples or in the other synthetic samples. This inflection suggests the presence of Fe(II) in the 150ºC sample. Unlike the other synthetic samples, which were incubated in air, this sample was incubated in a sealed, unbuffered, stainless-steel pressure vessel. Thus, the presence of Fe(II) suggests that Fe was not completely converted to Fe(III) during incubation under these oxygen-limited conditions. The small size of the inflection feature, however, suggests that the proportion of Fe(II) in this sample is minimal, which is further supported by the overall resemblance of this spectrum to the spectra of the natural nontronites that do not contain Fe(II).

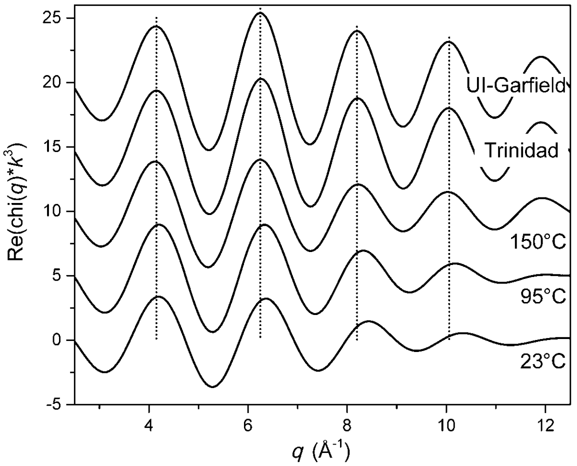

Figure 4. Back-transformed spectra of a first-shell backscattering peak ($\Delta R = 1-2$ Å) in UI-Garfield and Trinidad nontronites, and of synthetic nontronites crystallized at 23, 95, and 150ºC. The sample incubated at 4ºC is not shown, but is identical to that at 23ºC. Vertical dotted lines indicate peak positions for comparison.

The XANES spectra of Fe-bearing clay minerals (Baker *et al.*, 2010) and of Fe-substituted allophanes (Baker and Strawn, 2012) typically display an inflection at 7132 eV, most easily observed in the first-derivative spectrum. This inflection was also present in the spectra of the synthetic nontronites, although relatively poorly developed in the synthetic nontronite incubated at 23ºC.

EXAFS

The EXAFS spectra of natural nontronite samples (Figure 5) displayed many similarities to one another. The Fe−O backscattering peaks located near 2 Å in the Fourier-transformed spectra (Figure 5b) had similar magnitudes, in agreement with the bulk analyses, indicating that the two clay samples have similar octahedral cation compositions (Table 1). The second peak near 3 Å in the Fourier-transform results from backscattering from the three nearest-neighbor cations, and the peak at 4.8 Å results from backscattering by six second-octahedral neighboring Fe cations (Manceau *et al.*, 1998); both these peaks had lower amplitude for the Trinidad sample than for the UI-Garfield sample. This observation supports the suggestion above that the two nontronite samples, although having very similar bulk composition, may exhibit different cation ordering within their octahedral sheets. Small inflections and shoulders in the chi spectra of the natural samples (Figure 5a), such as those near 4, 6, 7.5, 9, and 11 $Å^{-1}$, were slightly different in the two samples, suggesting some minor differences between the two clays. Many of these inflections in the chi spectra result from backscattering by relatively distant atoms, or from multiple scattering (Manceau *et al.*, 1998). Back transformation of the Fourier-transformed spectra to exclude backscatterers beyond 4.5 Å eliminates most of these features, confirming that they were caused by multiple scattering or backscattering from more distant atoms.

The peak amplitude of the 150ºC synthetic nontronite EXAFS spectrum was lower than those of the natural samples, indicating this sample was less crystalline. The second FT peak for nearest-neighbor cation backscattering was shifted to a slightly shorter distance, suggesting that the influence of the high Al content of this sample on average backscattering distances. The presence of

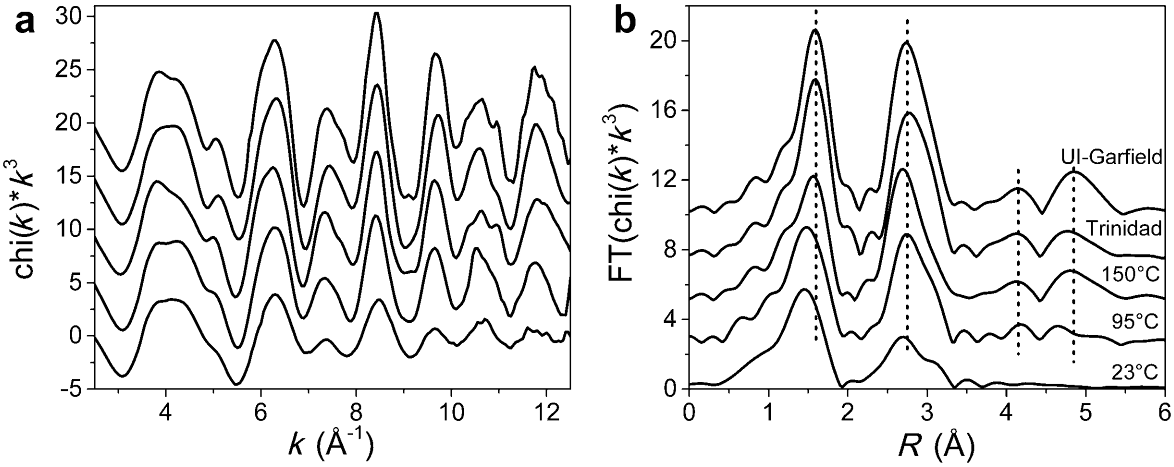

Figure 5. Chi spectra (a) and magnitude of Fourier transforms (b) of UI-Garfield and Trinidad nontronites, and synthetic nontronites crystallized at 23, 95, and 150ºC. The sample incubated at 4ºC is not shown, but is identical to that at 23ºC. Dashed lines in (b) at 1.6, 2.75, 4.15, and 4.85 Å are provided to compare relative peak positions between samples.

well developed FT peaks centered near 4.1 and 4.8 Å, resulting from backscattering by second-neighbor tetrahedral and octahedral cations, indicated that the 150ºC nontronite was well ordered to a distance of at least ~5.3 Å, the distance of the second octahedral neighboring cation in well ordered nontronite (Manceau *et al.*, 1998).

The 95ºC synthetic nontronite spectrum had a lower EXAFS amplitude than either the 150ºC synthetic sample or the two natural nontronite spectra. Many of the fine-scale features associated with the second octahedral neighbor backscattering that were observed in the 150ºC and natural nontronite spectra were absent or poorly developed in the 95ºC nontronite. A small peak was present at 4.6 Å in the Fourier-transformed spectrum, suggesting that the 95ºC synthetic nontronite does not have a well ordered shell of second octahedral cation neighbors. Thus, well ordered domains in this sample appeared to be <5 Å in radius.

The 23ºC and 4ºC synthetic nontronites displayed little structure beyond the first octahedral cation backscattering shell at ~3 Å. The two samples were very similar to one another, and neither appeared to have developed structure beyond that of a gel precipitate, or possibly a hisingerite-like structure.

Shell fitting

Shell fitting was carried out on the synthetic and natural nontronites. The fitting results for the UI-Garfield nontronite spectrum have previously been described by Baker and Strawn (2012), and the methodology described in that paper was used for fitting the synthetic and natural nontronites. The well characterized Garfield nontronite has been modeled out to 6 Å (Manceau *et al.*, 1998). For the less crystalline nontronites examined in the present study, however, fitting of more distant backscatterers and multiple scattering paths was not feasible. Thus, fits in this study focused on contributions of single-scattering paths within 4 Å, and on the relative contributions of Fe and Al nearest-neighbor backscatterers.

Because all the synthetic samples had a bulk composition with Fe:Al = 1, any sample in which the octahedral cations were randomly arranged should have a 1:1 ratio, regardless of synthesis temperature. Cations in phyllosilicate octahedral sheets are frequently distributed non-randomly, however, forming small domains or clusters of Fe or Al. This study, therefore, fitted the number of Fe and Al nearest neighbors around the central Fe atom, constraining the sum to be three total nearest-neighbor octahedral cations. Although natural samples contain small amounts of Mg, concentrations of this element are much lower than Fe and Al concentrations (Table 1), and the synthetic samples were Mg-free, thus the fits did not include Mg.

Fitting of UI-Garfield nontronite using the 6-shell model produced results in agreement with those published by Baker and Strawn (2012) and by Manceau *et al.* (1998) (Figure 6 and Table 3). This high-Fe nontronite contained very little Al (Table 1) and the number of Fe-Al nearest neighbors fit to zero. In Trinidad nontronite (Figure 6), nearest-neighbor octahedral cations were dominated by Fe, with the Al:Fe ratio optimizing to 1:5 (Table 3). This ratio was very close to a previous estimate for SWa-1 made from EXAFS fitting (Vantelon *et al.*, 2003). The actual bulk molar Al:Fe ratio of Trinidad nontronite was ~1:3 (Table 1). Errors in fitting second-shell coordination numbers have been reported to be on the order of 20% for relatively simple structures (O'Day *et al.*, 1994) and up to 40% for structures with moderate isomorphic substitution (Scheidegger *et al.*, 1996). Applying a 20% error to the Fe cation content estimated for Trinidad nontronite results in the Al:Fe ratio ranging from 0 to 1:2, a range

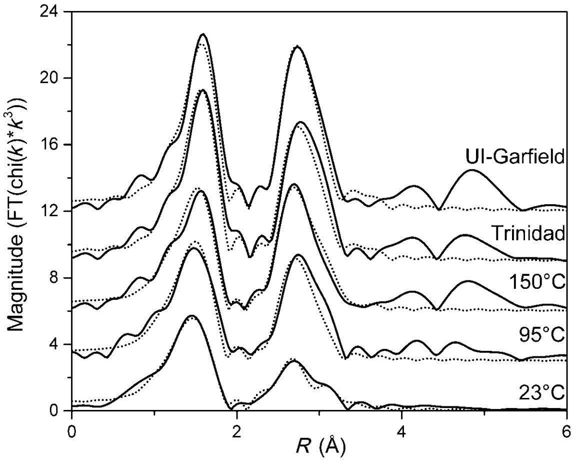

Figure 6. Shell fits to natural and synthetic nontronite samples using the parameters in Table 3.

that includes the fit results, but also suggests Fe could have a clustered distribution in this sample. The FTIR spectrum of the Trinidad nontronite also suggested it contained more Fe-Al nearest neighbors than UI-Garfield nontronite. The influence of Fe-Al backscattering was visible in the Fourier-transformed EXAFS spectrum of Trinidad nontronite as a slight broadening of the Fe-(Fe,Al) backscattering peak at 3 Å. The other fit parameters for Trinidad nontronite were similar to those fit for the UI-Garfield nontronite.

The 150ºC synthetic nontronite EXAFS (Figure 6) fit parameters were nearly identical to the theoretical path lengths for nontronite, and close to those optimized for the UI-Garfield standard (Table 3). The XRD data suggested that this sample had lower long-range crystallinity than the natural nontronites; the XAFS indicated that at the molecular scale, the structure was well ordered, however. The octahedral Fe-Fe and Fe-Al backscattering paths fit to identical distances. The *N*Fe value fitted to 2, suggesting an Al:Fe ratio of 1:2 in nearest-neighbor sites. This suggests some segregation of the octahedral cations into Fe-rich and Al-rich domains within the crystal. This observation is consistent with the observation of both Fe-Al-OH and Fe-Fe-OH features in its FTIR spectrum.

The 95ºC synthetic nontronite (Figure 6) XAFS fit values were also close to the UI-Garfield nontronite fit path lengths, with the exception of a shorter Fe–O1 path length (Table 3). The 0.02 Å difference in path length for the Fe–O1 path between the 95ºC and the 150ºC synthetic nontronites supports the XANES data interpretation that some tetrahedral Fe was present in the synthetic nontronite samples incubated at lower temperatures. The first-shell Debye-Waller parameter for the synthetic samples was greater than in the natural nontronites, which may be caused by both the tetrahedral Fe contribution and a more distorted first shell. The fitted Al:Fe ratio in the 95ºC sample (1.34:1.66) was greater than for the 150ºC sample, and was closer to the bulk composition of the sample, suggesting a random distribution of Fe and Al in the octahedral sheet.

The fit of the 23ºC synthetic nontronite (Figure 6) resulted in significant shortening of some backscattering paths compared to the higher-temperature synthetic samples, and the natural nontronites (Table 3). The fitted first shell Fe–O1 path length in the 23ºC synthetic nontronite was shorter than the 95ºC sample, and the Debye-Waller factor for that path was higher. The shorter distance and increased disorder for the first shell probably resulted from the presence of more tetrahedral Fe than was present in the higher-temperature nontronite samples. The fitted octahedral Al:Fe ratio was ~2:1, an interesting result in that it was greater than the bulk Al:Fe ratio. This may occur because of an ordered distribution of Fe within the octahedral sheet and may also be affected by the presence of tetrahedral Fe in the sample, particularly if Fe and Al do not partition equally into tetrahedral sites. Fe occupancies of up to 0.92 of 8 tetrahedral cations (11.5%) in natural nontronite samples were calculated by Gates *et al.* (2002) who observed that the sample with the greatest tetrahedral Fe content, NG-1, had a pre-edge peak height approximately twice that of Garfield nontronite. In the present study, the pre-edge peak height for the two lower-temperature nontronite samples was approximately twice that of UI-Garfield nontronite (Figure 7), suggesting a tetrahedral occupancy in the low-temperature nontronite gels of 10–20%.

DISCUSSION

Comparison of natural and synthetic nontronites

The results of XRD and FTIR analysis indicate that synthetic nontronites incubated for 4 weeks did not achieve the same degree of ordering as natural

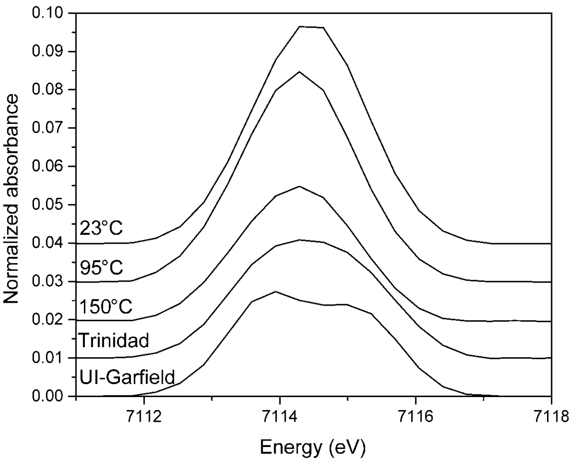

Figure 7. XANES pre-edge peaks (as in Figure 3 inset), with background slope subtracted for measurement of peak amplitudes. Each peak is offset vertically by 0.01 units for clarity, but relative amplitudes are correct.

nontronite clays, even when incubated at 150ºC (Figures 1−2). On the local atomic scale, however, synthetic nontronite incubated at 150ºC for 4 weeks revealed a similar degree of ordering to natural UI-Garfield nontronite (Figures 3, 5). The synthetic nontronite incubated at 95ºC displayed some nontronite-like structure, detectable by FTIR and XAFS (Figures 2, 3, 5), but little longer-range ordering detectable by XRD (Figure 1). On the atomic scale, the 95ºC sample was clearly less well ordered than the natural nontronite samples or the 150ºC sample. An inflection in the XANES at 7132 eV (Figure 3) was observed in all the synthetic samples, but was only weakly developed in samples incubated at lower temperatures. Development of a strong inflection at this energy may result from the presence of well ordered backscattering shells within 4 Å of the target atom (Chen *et al.*, 2002). The well developed peaks at this energy in the two higher-temperature synthetic nontronites suggest that at the molecular scale, the atomic ordering was comparable to that in the natural nontronites.

The synthetic nontronite incubated at 23ºC did not display well formed nontronite structure, and its spectrum was identical to that of the precursor gel incubated at 4ºC (data not shown). This 23ºC nontronite was comparable in terms of atomic ordering to an Fe-substituted allophane gel or to hisingerite (Baker and Strawn, 2012). The XANES peak at 7132 eV (Figure 3) in the 23ºC sample was of comparable size to that in Fe-allophane, suggesting that the limit of the backscattering order was ~4 Å , and thus that coherent domains were <8 Å in diameter. The Fe-Fe peak at 3 Å in this sample was also very poorly developed compared to the higher-temperature samples (Figure 5), indicating a lack of ordering even within this distance of the central backscattering Fe atom. This suggested that well ordered domains within the 23ºC sample may be as small as 4−5 Å in diameter. Assuming this growth rate can be extrapolated meaningfully, coherent domains of ~100 Å in diameter would form in ~2 y. This result is reasonably consistent with the growth rates measured by Decarreau *et al.* (1987), who suggested coherent domains ~100 Å in diameter would form in ~10 y at 23ºC. Given the relatively poor constraints on both estimates, these results agree fairly well, and support the argument that, at ambient surface temperatures, formation of nontronite particles that approached macroscopic crystalline structure would require several years.

The formation temperature of natural nontronites in the CRB can be constrained based on field observations. Because liquid water is necessary for nontronite formation, basalt can be altered at >100ºC only under sufficient confining pressure to condense water. The nontronite localities in the CRB sampled in this study occurred in open cracks in basalt flows within a few meters of the surface, indicating that nontronite formation occurred at or near atmospheric pressure. At Garfield, Washington, for example, nontronite was found <1 m below the surface in vertical cracks open to the basalt flow surface. Thus, although nontronite formation at Garfield may have been accelerated by residual heat from emplacement of the host basalt, it cannot have occurred at temperatures above 100ºC because liquid water in the open cracks would have escaped by boiling. The Trinidad nontronite showed field evidence of having been influenced directly by heat from the emplaced basalt, and by water derived from the underlying paleosols, but it formed only a few meters below the surface and would not have been subject to significant confining pressure. Similar constraints are observed for other nontronite occurrences in the CRB (Baker *et al.*, 2012). Thus, these natural CRB nontronites are all likely to have formed at temperatures of <100ºC.

The synthetic nontronites included a sample incubated at 95ºC, close to the highest temperature likely for the natural nontronite formation conditions. This sample was considerably less ordered than the natural samples, however. Thus, the high degree of crystallinity observed in the natural nontronites is not due to crystallization at high temperatures, in agreement with the conclusions of Decarreau *et al.* (1987, 2008). The high crystallinity of naturally occurring nontronites suggests that these samples formed over long periods of time at ambient near-surface conditions. Variation in natural conditions, such as wetting-drying cycles and winter-summer temperature oscillations, may promote recrystallization of natural nontronites to more ordered forms.

Some nontronitic clays formed in basalts from Mururoa Atoll show textural evidence of having precipitated directly from boiling fluids shortly after basalt emplacement, with the fluids being derived either externally or from a residual magmatic phase (Meunier *et al.*, 2008, 2012). Based on the oxygen isotopic composition of the Mururoa nontronites (Meunier *et al.*, 2008), estimated formation temperatures were between 64 and 109ºC, although higher temperatures for void-filling clays that appeared to have formed by direct precipitation were suggested. The experimental work of Decarreau *et al.* (2008) places a high-temperature limit of 200ºC for the formation of the void-filling clays. No such textural evidence has been observed for CRB nontronites.

Constraining growth rates and conditions for natural nontronites

The UI-Garfield and Trinidad nontronites both occurred in flows of Wanapum age, ~14 m.y. (Swanson *et al.*, 1979) which represents the maximum possible formation time for the natural nontronite samples. This formation time would facilitate slow growth of nontronite, mostly at ambient surface temperatures. Previous studies have suggested that basalt alteration products typically formed at more elevated temperatures such as those measured by Meunier *et al.*

(2008). The formation of palagonite and nontronite *vs.* temperature in a drill hole in basaltic lavas at Surtsey Volcano, Iceland, was calibrated by Jakobsson and Moore (1986) who found that at 100ºC palagonite formed a rim on basaltic glass at a rate of 2.8 μm/y, and that this rate doubled with every 12ºC increase in temperature. At temperatures >120ºC, nontronite formed a rim on olivine crystals at a rate of 0.3 μm/y; this rate doubled with every 8ºC increase, but nontronite growth was not observed at lower temperatures. This growth rate is faster than the rates measured experimentally by Decarreau *et al.* (1987), but drops more rapidly with temperature. A measurable thickness of palagonite was observed forming at Surtsey at ambient water temperatures of 7−10ºC. Palagonite has been shown to consist primarily of nontronite (Summers, 1976; Stroncik and Schmincke, 2002), but the fibropalagonite identified by Jakobsson and Moore (1986) at Surtsey is described as containing more TiO_2, Al_2O_3, and CaO, and less FeO, than nontronite samples collected from the same site. This growth rate is faster than the rates measured experimentally by Decarreau *et al.* (1987), but drops more rapidly with temperature.

The growth rates measured by Jakobsson and Moore (1986) may not be directly applicable to nontronites in the CRB. Olivine is rare in CRB, and nontronite in the basalts coats or fills glass rather than olivine crystals. In addition, the physical environment of CRB nontronites constrains their formation temperatures to be <100ºC. Calculations based on the published nontronite growth rates nonetheless provide some constraints on plausible formation times for CRB nontronites. Nontronites from Garfield, Washington, and at other CRB sites fill cracks up to 1 cm wide, although narrower cracks are more typical. Extrapolating the rate of nontronite formation from olivine at Surtsey at 120ºC (Jakobsson and Moore, 1986) down by a factor of two with every 8ºC decrease in temperature yields an estimate of the rate of nontronite formation at 95ºC of ~0.03 μm/y. Assuming a 1-cm wide crack is filled with pure nontronite that is growing as a rim on the basalt glass on both sides of the crack, formation of 1 cm nontronite veins in the CRB would take 1.67×10^5 y. Palagonite at Surtsey grew at a rate of 2.8 μm/y at 100ºC (Jakobsson and Moore, 1986), and even at this faster growth rate, ~1800 y would be required for a 1 cm crack to fill with palagonite.

In the absence of other heat sources, nontronite growth rates may also be constrained by considering basalt cooling rates. For a CRB nontronite precipitated in an open crack, the temperature of formation must have been below the boiling point of water. Detailed models of basalt cooling suggest that the material within 1 m of a basalt flow surface will take a period of several years to cool from 100ºC to ambient temperatures (Lore *et al.*, 2000). Studies of field constraints on emplacement and cooling of individual Columbia River Basalt flows (Long and Wood, 1986; Reidel, 1998; Thordarson and Self, 1998) estimate cooling timescales on the order of several years, although these studies focus more on cooling to solidification rather than to ambient temperature. If CRB nontronite formation occurred at temperatures close to 100ºC after basalt emplacement and solidification, formation rates would have to be several orders of magnitude higher than those observed by Jakobsson and Moore (1986) to account for the nontronite occurrences observed in the weathered CRB.

If nontronite were to form *via* basalt alteration at high temperatures, then rapid cooling of basalt flows requires that this process occur within a period of years to hundreds of years, more rapidly than has been observed in the studies cited above. Otherwise nontronite formation must continue after the flow has cooled to ambient conditions. Given that reaction kinetics are strongly temperature-dependent, nontronite crystallization at ambient conditions is expected to be a slow process. Extrapolating the measured growth rates of Jakobsson and Moore (1986) down to an ambient temperature of 20ºC suggests a rate of <1 nm/y, fairly comparable to the estimate above for the synthetic sample incubated at 23ºC. This implies formation times on the order of millions of years to develop 1 cm of crack-filling nontronite, suggesting that nontronite formation has been ongoing for much or all of the 14 million y since emplacement of the hosting basalts. Diurnal heating of the host basalts may have accelerated nontronite growth rates somewhat; near-surface temperatures of up to 65ºC have been measured on basalt flows at Craters of the Moon National Monument, Idaho, USA (Day and Wright, 1989).

If nontronite continues to crystallize at ambient surface temperatures, then natural nontronite occurrences would be expected to include samples with a wide range of crystallinity, representing different total times of crystallization and resembling the range of crystallinity observed in the synthetic samples. Clay infill in cracks and void spaces might be predicted in this case to exhibit zoned crystallinity, but this has not been described in CRB. Collection of such samples would represent evidence that nontronite formation is an ongoing process in CRB weathering.

Nontronite has been observed in very old (>3.5 Ga) rocks on Mars by orbiting spacecraft, and this observation has been presented as evidence for water–rock interaction in the ancient Martian past (Bishop *et al.*, 2008; Ehlmann *et al.*, 2011). The presence of this and other clay minerals on Mars may provide information about the Martian climate and hydrosphere at the time of clay formation. As the results of the present study suggest nontronite formation is relatively slow, this suggests relatively long periods of water−rock interaction on Mars. Further information on nontronite-formation conditions on Earth, and on the characteristics of the Martian nontronite occurrences, will help to refine this conclusion.

CONCLUSIONS

Synthetic nontronites incubated for 4 weeks at temperatures up to 150ºC did not achieve the degree of crystallinity observed in natural nontronite samples formed by weathering of Columbia River Basalts. Synthetic nontronites also exhibited lower degrees of cation ordering, and contained more tetrahedral Fe than natural samples. Because previously published studies indicate that nontronite does not form at temperatures >200ºC, this suggests that the formation of well ordered nontronite crystals requires much longer formation times than were used in this experimental study.

Field relations indicate that some Columbia River Basalt nontronites exhibiting good crystalline ordering must have formed at temperatures below the boiling point of water at the Earth's surface. Published estimates of nontronite growth rates suggest very slow growth at low temperature, a result in agreement with the present observations. Estimates of experimental nontronite crystallization rates, coupled with field constraints and published growth-rate estimates, suggest that naturally occurring CRB nontronites formed slowly over millions of years at ambient surface temperatures.

ACKNOWLEDGMENTS

The authors thank Jeff Boyle and Jim Harsh at Washington State University for locating and sharing field notes of J.A. Kittrick indicating the SWa-1 sample-collection locality. Ryan Nickerson assisted with sample synthesis and preparation and with XAFS analyses. Comments from two anonymous reviewers were helpful in improving the manuscript. Partial funding for this project was provided by an Idaho Space Grant Consortium Research Initiation Grant. Portions of this research were carried out at the Stanford Synchrotron Radiation Lightsource, a Directorate of SLAC National Accelerator Laboratory and an Office of Science User Facility operated for the U.S. Department of Energy Office of Science by Stanford University. The SSRL Structural Molecular Biology Program is supported by the DOE Office of Biological and Environmental Research, and by the National Institutes of Health, National Institute of General Medical Sciences (including P41GM103393). The contents of this publication are solely the responsibility of the authors and do not necessarily represent the official views of NIGMS or NIH.

REFERENCES

Allen, V.T. and Scheid, V.E. (1946) Nontronite in the Columbia River region. *American Mineralogist*, **31**, 294–312.

Baker, L.L. and Strawn, D.G. (2012) Fe K-edge XAFS spectra of phyllosilicates of varying crystallinity. *Physics and Chemistry of Minerals* **39**, 675–684.

Baker, L.L., Strawn, D.G., Vaughan, K.L., and McDaniel, P.A. (2010) XAS study of Fe mineralogy in a chronosequence of soil clays formed in basaltic cinders. *Clays and Clay Minerals* **58**, 6, 772–782.

Baker, L., Strawn, D., McDaniel, P., Fairley, J., and Bishop, J. (2012) Hydrologic and geochemical controls on nontronite formation in terrestrial Columbia River Basalts and implications for clay formation on Mars. *LPI Contributions* **1680**, 7011.

Benson, L.V. and Teague, L.S. (1982) Diagenesis of basalts from the Pasco Basin, Washington: I. Distribution and composition of secondary mineral phases. *Journal of Sedimentary Research*, **52**, 595–613.

Bishop, J.L., Dobrea, E.Z.N., McKeown, N.K., Parente, M., Ehlmann, B.L., Michalski, J.R., Milliken, R.E., Poulet, F., Swayze, G.A., Mustard, J.F., Murchie, S.L., and Bibring, J.-P. (2008) Phyllosilicate diversity and past aqueous activity revealed at Mawrth Vallis, Mars. *Science*, **321**, 830–833.

Chen, L.X., Liu, T., Thurnauer, M.C., Csencsits, R., and Rajh, T. (2002) Fe_2O_3 nanoparticle structures investigated by X-ray absorption near-edge structure, surface modifications, and model calculations. *The Journal of Physical Chemistry B*, **106**, 34, 8539–8546.

Cole, T. and Shaw, H. (1983) The nature and origin of authigenic smectites in some recent marine sediments. *Clay Minerals* **18**, 3, 239–252.

Day, T.A. and Wright, R.G. (1989) Positive plant spatial association with Eriogonum ovalifolium in primary succession on cinder cones: seed-trapping nurse plants. *Plant Ecology*, **80**, 37–45.

Decarreau, A. and Bonnin, D. (1986) Synthesis and crystallogenesis at low temperature of Fe (III)-smectites by evolution of coprecipitated gels: experiments in partially reducing conditions. *Clay Minerals*, **21**, 861–877.

Decarreau, A., Bonnin, D., Badaut-Trauth, D., Couty, R., and Kaiser, P. (1987) Synthesis and crystallogenesis of ferric smectite by evolution of Si-Fe coprecipitates in oxidizing conditions. *Clay Minerals*, **22**, 207–223.

Decarreau, A., Petit, S., Martin, F., Farges, F., Vieillard, P., and Joussein, E. (2008) Hydrothermal synthesis, between 75 and 150ºC, of high-charge, ferric nontronites. *Clays and Clay Minerals* **56**, 322–337.

Dekov, V.M., Kamenov, G.D., Stummeyer, J., Thiry, M., Savelli, C., Shanks, W.C., Fortin, D., Kuzmann, E., and Vértes, A. (2007) Hydrothermal nontronite formation at Eolo seamount (Aeolian volcanic arc, Tyrrhenian Sea). *Chemical Geology*, **245**, 103–119.

Eggleton, R. (1977) Nontronite: Chemistry and diffraction. *Clay Minerals*, **12**, 181–194.

Ehlmann, B.L., Mustard, J.F., Murchie, S.L., Bibring, J.-P., Meunier, A., Fraeman, A.A., and Langevin, Y. (2011) Subsurface water and clay mineral formation during the early history of Mars. *Nature*, **479**, 7371, 53–60.

Farmer, V., Krishnamurti, G., and Huang, P. (1991) Synthetic allophane and layer-silicate formation in SiO_2-Al_2O_3-FeO-Fe_2O_3-MgO-H_2O systems at 23ºC and 89ºC in a calcareous environment. *Clays and Clay Minerals*, **39**, 561–570.

Farmer, V., McHardy, W., Elsass, F., and Robert, M. (1994) hk-ordering in aluminous nontronite and saponite synthesized near 90ºC: Effects of synthesis conditions on nontronite composition and ordering. *Clays and Clay Minerals*, **42**, 180–180.

Fialips, C.-I., Huo, D., Yan, L., Wu, J., and Stucki, J.W. (2002) Effect of Fe oxidation state on the IR spectra of Garfield nontronite. *American Mineralogist*, **87**, 630–641.

Frost, R.L., Kloprogge, J.T., and Ding, Z. (2002) The Garfield and Uley nontronites – an infrared spectroscopic comparison. *Spectrochimica Acta Part A: Molecular and Biomolecular Spectroscopy*, **58**, 9, 1881–1894.

Gates, W.P. (2005) Infrared spectroscopy and the chemistry of dioctahedral smectites. Pp. 125–168 in: *Vibrational Spectroscopy of Layer Silicates and Hydroxides* (T. Kloprogge, editor). The Clay Minerals Society, Aurora, CO, USA.

Gates, W.P. (2008) Cation mass-valence sum (CM-VS) approach to assigning OH-bending bands in dioctahedral smectite. *Clays and Clay Minerals*, **56**, 10–22.

Gates, W.P., Slade, P.G., Manceau, A., and Lanson, B. (2002) Site occupancies by iron in nontronites. *Clays and Clay Minerals*, **50**, 223–239.

Harder, H. (1976) Nontronite synthesis at low temperatures. *Chemical Geology*, **18**, 169–180.

Harder, H. (1978) Synthesis of iron layer silicate minerals under natural conditions. *Clays and Clay Minerals*, **26**, 65–72.

Jakobsson, S.P. and Moore, J.G. (1986) Hydrothermal minerals and alteration rates at Surtsey volcano, Iceland. *Geological Society of America Bulletin*, **97**, 648–659.

Keeling, J.L., Raven, M.D., and Gates, W.P. (2000) Geology and characterization of two hydrothermal nontronites from weathered metamorphic rocks at the Uley graphite mine, South Australia. *Clays and Clay Minerals*, **48**, 5, 537–548.

Kerr, P.F. and Kulp, J.L. (1949) Reference clay localities, United States. Pp. 69–73 in: *Reference Clay Minerals;* American Petroleum Institute Research Project **49**, Preliminary Reports no. 1–8 (P.F. Kerr and J.L. Kulp, editors). Columbia University, New York.

Köhler, B., Singer, A., and Stoffers, P. (1994) Biogenic nontronite from marine white smoker chimneys. *Clays and Clay Minerals*, **42**, 689–701.

Long, P.E. and Wood, B.J. (1986) Structures, textures, and cooling histories of Columbia River basalt flows. *Geological Society of America Bulletin*, **97**, 1144–1155.

Lore, J., Gao, H., and Aydin, A. (2000) Viscoelastic thermal stress in cooling basalt flows. *Journal of Geophysical Research: Solid Earth (1978–2012)*, **105**, B10, 23695–23709.

Manceau, A., Bonnin, D., Stone, W.E.E., and Sanz, J. (1990) Distribution of Fe in the octahedral sheet of trioctahedral micas by polarized EXAFS; comparison with NMR results. *Physics and Chemistry of Minerals*, **17**, 363–370.

Manceau, A., Chateigner, D., and Gates, W.P. (1998) Polarized EXAFS, distance-valence least-squares modeling (DVLS), and quantitative texture analysis approaches to the structural refinement of Garfield nontronite. *Physics and Chemistry of Minerals*, **25**, 347–365.

Meunier, A., Mas, A., Beaufort, D., Patrier, P., and Dudoignon, P. (2008) Clay minerals in basalt-hawaiite rocks from Mururoa atoll (French Polynesia). II. Petrography and geochemistry. *Clays and Clay Minerals*, **56**, 730–750.

Meunier, A., Petit, S., Ehlmann, B.L., Dudoignon, P., Westall, F., Mas, A., El Albani, A., and Ferrage, E. (2012) Magmatic precipitation as a possible origin of Noachian clays on Mars. *Nature Geoscience*, **5**, 739–743.

Montarges-Pelletier, E., Bogenez, S., Pelletier, M., Razafitianamaharavo, A., Ghanbaja, J., Lartiges, B., and Michot, L. (2005) Synthetic allophane-like particles: textural properties. *Colloids and Surfaces A: Physicochemical and Engineering Aspects*, **255**, 1–10.

Neumann, A., Petit, S., and Hofstetter, T.B. (2011) Evaluation of redox-active iron sites in smectites using middle and near infrared spectroscopy. *Geochimica et Cosmochimica Acta*, **75**, 2336–2355.

O'Day, P.A., Rehr, J.J., Zabinsky, S.I., and Brown, G.E., Jr. (1994) Extended X-ray absorption fine structure (EXAFS) analysis of disorder and multiple-scattering in complex crystalline solids. *Journal of the American Chemical Society*, **116**, 2938–2949.

Ravel, B. and Newville, M. (2005) ATHENA, ARTEMIS, HEPHAESTUS: data analysis for X-ray absorption spectroscopy using IFEFFIT. *Journal of Synchrotron Radiation*, **12**, 537–541.

Reidel, S.P. (1998) Emplacement of Columbia River flood basalt. *Journal of Geophysical Research: Solid Earth (1978–2012)*, **103**, 27393–27410.

Reidel, S.P., Camp, V.E., Tolan, T.L., and Martin, B.S. (2013) The Columbia River flood basalt province: Stratigraphy, areal extent, volume, and physical volcanology. *Geological Society of America Special Papers*, **497**, 1–43.

Russell, J.D. and Fraser, A.R. (1994) Infrared Methods. Pp. 11–67 in: *Clay Mineralogy: Spectroscopic and Chemical Determinative Methods* (M.J. Wilson, editor). Chapman & Hall, London.

Scheidegger, A.M., Lamble, G.M., and Sparks, D.L. (1996) Investigation of Ni sorption on pyrophyllite: An XAFS study. *Environmental Science & Technology*, **30**, 548–554.

Severmann, S., Mills, R.A., Palmer, M.R., and Fallick, A.E. (2004) The origin of clay minerals in active and relict hydrothermal deposits. *Geochimica et Cosmochimica Acta*, **68**, 73–88.

Shoji, S., Nanzyo, M., and Dahlgren, R. (1993) *Volcanic Ash Soils: Genesis, Properties and Utilization.* Elsevier, New York.

Stroncik, N.A. and Schmincke, H.U. (2002) Palagonite – a review. *International Journal of Earth Sciences*, **91**, 680–697.

Summers, K. (1976) The clay component of the Columbia River palagonites. *American Mineralogist*, **61**, 492–494.

Swanson, D.A., Wright, T.L., Hooper, P.R., and Bentley, R.D. (1979) *Revisions in Stratigraphic Nomenclature of the Columbia River Basalt Group: U.S. Geological Survey Bulletin no. 1457*. U.S. Government Printing Office.

Thordarson, T. and Self, S. (1998) The Roza Member, Columbia River Basalt Group: A gigantic pahoehoe lava flow field formed by endogenous processes? *Journal of Geophysical Research*, **103**, 27411–27427, 27445.

Ueshima, M. and Tazaki, K. (2001) Possible role of microbial polysaccharides in nontronite formation. *Clays and Clay Minerals*, **49**, 292–299.

Vantelon, D., Montarges-Pelletier, E., Michot, L.J., Pelletier, M., Thomas, F., and Briois, V. (2003) Iron distribution in the octahedral sheet of dioctahedral smectites. An Fe K-edge X-ray absorption spectroscopy study. *Physics and Chemistry of Minerals*, **30**, 44–53.

Webb, S.M. (2005) Sixpack: A graphical user interface for XAS analysis using IFEFFIT. *Physica Scripta*, **T115**, 1011–1014.

Westre, T.E., Kennepohl, P., DeWitt, J.G., Hedman, B., Hodgson, K.O., and Solomon, E.I. (1997) A multiplet analysis of Fe K-edge 1s → 3d pre-edge features of iron complexes. *Journal of the American Chemical Society*, **119**, 6297–6314.

(*Received 27 February 2014; revised 26 May 2014; Ms. 853; AE: R. Kukkadapu*)

Clays and Clay Minerals, Vol. 62, No. 2, 102–111, 2014.

STUDY OF LOW-PRESSURE ARGON ADSORPTION ON SYNTHETIC NONTRONITE: IMPLICATIONS FOR SMECTITE CRYSTAL GROWTH

Alain Decarreau[1], Sabine Petit[1,]*, Pauline Andrieux[1], Frederic Villieras[2], Manuel Pelletier[2], and Angelina Razafitianamaharavo[2]

[1] Université de Poitiers, CNRS UMR 7285 IC2MP, HydrASA, 6 rue Michel Brunet, F-86022 Poitiers Cedex, France
[2] Laboratoire Environnement et Minéralurgie, UMR 7569, CNRS Université de Lorraine, BP 40,
F-54501 Vandoeuvre-lès-Nancy, France

Abstract—Because relatively little information about the crystal-growth process of smectite is available, the process was assessed here by studying the size and shape of nontronite particles synthesized at six different temperatures from 75 to 150ºC over a period of 4 weeks.

The morphology of nontronites was studied using low-pressure isotherms of argon adsorption at 77 K, a method which enables the measurement of the basal and edge surface areas of the nontronite particles and of their mean diameter and thickness. During the crystal growth of nontronite, the mean particle length increased whereas their thickness (and the number of stacked layers) did not vary significantly.

A specific two-dimensional crystal-growth process was observed for smectite *via* the lateral extension of the layers. This process also appears to occur during the growth of neoformed natural smectite.

Key Words—Argon Adsorption, Crystal Growth, Crystallinity, Infrared Spectroscopy, Isotherm, Nontronite, Particle Size, Smectite, Surface Area, Synthesis.

INTRODUCTION

The most notable property of smectites, compared to other clay minerals, is the expandability of its layers, which is linked to the nature and number of polar molecules (water, glycol, *etc.*) that surround the interlayer cations (Brindley and Brown, 1980). The *c* crystallographic parameter is variable for layers with a constant chemistry. In smectite, the interlayer cations (*e.g.* Na^+, K^+, Li^+, Ca^{2+}, and Mg^{2+}) are exchangeable and depend on the composition of the last fluid that was in contact with the smectite. Thus, only the 2:1 layer is relatively stable with time, in contrast to the labile interlayer.

Smectites are generally described as thin crumpled sheets (with a few tens of stacked layers), a few hundred nanometers wide, usually anhedral, which form aggregates (Güven, 1988). The study of the morphological evolution of smectites during crystal growth in natural or experimental systems is not straightforward, therefore. Numerous studies of smectite synthesis exist in the literature (for examples see reviews by Kloprogge *et al.*, 1999, and Zhang *et al.*, 2010). In such studies, however, data on the shape and size of the smectite particles are often discussed with respect to synthesis conditions (temperature, pressure, pH, ...) and not with respect to the crystal-growth issue.

Transmission electron microscopy (TEM) and atomic force microscopy (AFM) are useful tools for studying the morphology of clays and many studies have been devoted to imaging in three dimensions clay minerals with euhedral or sub-euhedral character, such as kaolinite, micas, and mixed-layer clays (Meunier, 2010 and references therein). For these clay minerals, crystal growth occurs *via* three-dimensional processes and often exhibits polygonal and spiral-growth patterns (Baronnet, 1972; Meunier, 2010). Researchers have also used TEM and AFM to study smectite dissolution (*e.g.* Bickmore *et al.*, 2001; Bauer *et al.*, 2006; Kuwahara, 2006).

The Crystal Size Distributions (CSDs) of illite and illite-smectite samples were studied by Eberl *et al.* (1998) and Środoń *et al.* (2000) using TEM imaging. The CSDs may have distinctive shapes related to the mineral's crystal-growth history: nucleation, growth in an open or closed system, Ostwald ripening, *etc.* The CSDs method was used by Christidis (2001) to study a bentonite from Greece. Only the length and width of particles were measured, suggesting supply-controlled crystal growth in an open system or random ripening in a closed system.

An alternate approach to studying clay morphology is high-resolution, low-pressure argon adsorption, a method based on surface-energy heterogeneity analysis, using the summation of the local derivative isotherms method (Villiéras *et al.*, 1992, 1997a, 1997b, 2002; Michot and Villiéras, 2006). The validity of this method was first tested on kaolinite and sepiolite *via* comparison of results obtained with those from low-temperature adsorption microcalorimetry (Villiéras *et al.*, 1992, 1997a). More recently, the study of the geometric properties of smectite, kaolinite, and illite using both AFM and argon adsorption (Tournassat *et al.*, 2003, Sayed Hassan *et al.*, 2006) demonstrated the consistency

---

* E-mail address of corresponding author:
sabine.petit@univ-poitiers.fr
DOI: 10.1346/CCMN.2014.0620203

Table 1. Coherent scattering domain size (CSDS) of nontronite particles from powder XRD data.

T (ºC)	(001)		(06,33)
	H (Å)	*N*	D (Å)
150	76	6.3	189
125	63	5.2	190
110	50	4.1	138
100	45	3.8	142
90	48	4.0	114
75	nm	nm	nm

H = crystal coherency along the c* direction (air dry conditions, Na as interlayer cation); *N* = number of stacked layers (assuming d_{001} = 12 Å); *D* = crystal coherency in the (001) layer plane; nm = not measurable (crystallinity too low).

between these two methods. Argon adsorption has also been used to study the shape and size of smectite particles, including saponite (Michot and Villiéras, 2002), montmorillonite, and nontronite (Tournassat *et al.*, 2003; Peronnet *et al.*, 2007; Le Forestier *et al.*, 2010). High-resolution, low-pressure argon adsorption enables the simultaneous investigation of all of the clay particles in a sample, which results in the accurate determination of mean basal and edge surface areas (Sayed Hassan *et al.*, 2006).

The objective of this study was to determine changes in particle shape and size in a series of nontronite samples as a function of synthesis temperature, by applying high-resolution, low-pressure argon adsorption.

MATERIALS AND METHODS

Sample description and characterization

A series of nontronite samples was synthesized by Decarreau *et al.* (2008) from a coprecipitated gel with the composition $Si_2FeNa_2O_6.nH_2O$ over a 4-week period at temperatures that ranged from 75 to 150ºC. Nontronite was demonstrated to be the only mineral that could precipitate under these synthesis conditions (Decarreau *et al.*, 2004, 2008). These synthetic nontronites were studied in detail using X-ray diffraction (XRD), TEM, chemical analyses, differential thermal and gravimetric analysis (DTA-DTG), and Fourier-transform infrared (FTIR), Mössbauer, and X-ray absorption near edge (XANES) spectroscopies (Decarreau *et al.*, 2008). Irrespective of the synthesis temperature, the nontronite samples exhibited the same structural formula of $(Si_{3.25}Fe^{3+}_{0.75})Fe^{3+}_2O_{10}(OH)_2,Na_{0.75}$. An increase in the synthesis temperature increased the crystallinity of samples. The synthesis products consisted of nontronite and some amorphous residual phase. As determined from the DTG data (Decarreau *et al.*, 2008), the proportion of starting gel which crystallized into nontronite increased from 70% to >90% with the increase in synthesis temperature. Taking into account the uncertainties in the DTG data, the samples obtained at 125 and 150ºC were assumed to be of pure nontronite.

From XRD powder data (Decarreau *et al.*, 2008), the coherent scattering domain size (CSDS) (Moore and Reynolds, 1989, p. 87) was measured using the Scherrer equation ($L = K\cdot\lambda/B\cdot\cos\theta$) in the (001) plane and along the [001]* direction (also known as the c* direction) from the widths of the (06,33) and (001) reflections, respectively (Table 1). The K values in the Scherrer equation were 1 for the (001) reflection and 1.91 for the (06,33) composite reflection (Brindley and Brown, 1980, pp. 131, 139). When the synthesis temperature was increased, the CSDS in the plane of the layers was increased at temperatures from 75 to 125ºC, and then remained constant (Figure 1). Along the c* direction, the CSDS remained constant between 75 and 100ºC and then increased slightly (Figure 1). Using a d_{001} value of 12 Å, the number of stacked layers as determined from the XRD data was between 4 and 6.

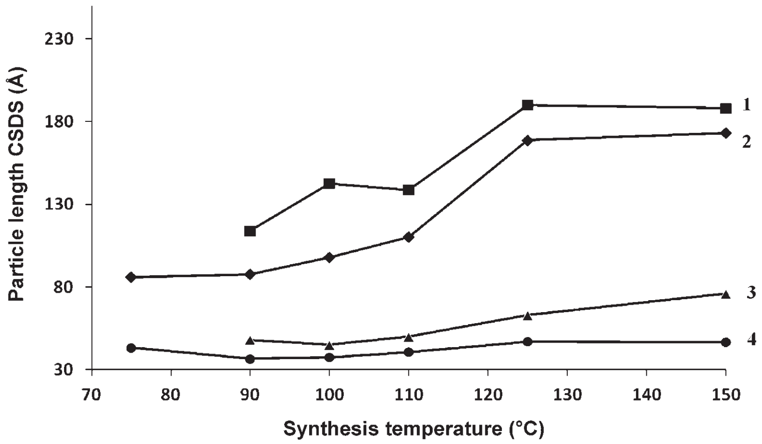

Figure 1. Coherent scattering domain size (CSDS) (from XRD, in the layer plane (2) and in the c* direction (3)) and dimensions (from argon adsorption: particle length (1) and thickness (4)) of particles *vs.* synthesis temperature of nontronites.

In the TEM images (Decarreau *et al.*, 2008), irrespective of the synthesis temperature, isolated nontronite particles appeared as crumpled flakes with rolled edges associated in micron-sized aggregates. The TEM images showed that the aggregates contained numerous particles <10 nm in size. These small particles were less evident in the samples prepared at 125 and 150ºC. The largest observed particles were 400 nm for the sample prepared at 150ºC. Even after strong ultrasonic treatment, the nontronite particles still formed thick aggregates irrespective of the sample: a measurement of the particle-size distribution was not possible.

Low-pressure argon adsorption at 77 K

The fundamentals of the low-pressure argon adsorption approach and the derivative isotherm summation (DIS) method were given by Villiéras *et al.* (1992, 1997a, 1997b, 2002). The low-pressure isotherms of argon adsorption at 77 K were recorded using a lab-built, automatic, quasi-equilibrium volumetric apparatus (Michot *et al.*, 1990; Villiéras *et al.*, 1992, 1997b). Approximately 1 g of the sample was outgassed overnight at 110ºC under a residual pressure of 10^{-4} Pa. After the samples were outgassed, a slow and constant flow of argon was introduced into the adsorption cell through a micro-leak up to the Brunauer-Emmet-Teller (BET) domain ($P/P_0 \geqslant 0.15$). If the flow rate is sufficiently low, the measured pressures are considered to be quasi-equilibrium pressures (in the range of 10^{-3} to 3×10^4 Pa). From the recording of the quasi-equilibrium pressure as a function of time, high-resolution adsorption isotherms were obtained for the apparent filling of the first monolayer (± BET Monolayer capacity, $0.08 \geqslant P/P_0 \geqslant 0.15$) with >2000 experimental data points. The derivative of the adsorbed quantity is calculated as a function of the logarithm of the relative pressure, $\ln(P/P_0)$, which corresponds to the free energy of adsorption in kT or RT units (Villiéras *et al.*, 1992, 1997a). The total derivative adsorption isotherm on a heterogeneous surface is then simulated by the sum of the local theoretical derivative adsorption isotherms using concepts that describe the adsorption phenomena on heterogeneous surfaces and the DIS procedure (Villiéras *et al.*, 1992, 1997a). For each local isotherm, the BET multilayer adsorption model was used and the following parameters obtained: ω, the lateral interaction between two neighboring adsorbed molecules; $\ln(P/P_0)$, the position of the peak; and Vm, the monolayer capacity. The DIS fitting procedure has been described extensively by Villiéras *et al.* (1992, 1997a, 1997b, 2002) and, for swelling clays, by Perronnet *et al.* (2007).

For clay minerals with large cations (*e.g.* K^+) on their external surfaces, the values of the basal surface and edge surface areas measured by low-pressure argon adsorption can be significantly smaller as shown by Sayed-Hassan *et al.* (2005) for kaolinite edge surfaces and by Bardot *et al.* (1998) for illite basal and edge surfaces. Therefore, prior to the adsorption experiments, the clay samples were Na^+-saturated using a 1 M NaCl solution and washed until all excess ions were removed, as indicated by the $AgNO_3$ test.

RESULTS

Irrespective of the synthesis temperature, the derivative isotherms of the low-pressure argon adsorption of the synthesized nontronites exhibited the same features (Figure 2). As typical for phyllosilicates (Sayed Hassan *et al.*, 2006; Villiéras *et al.*, 1992, 1997a, 1997b), the derivative isotherms exhibited a peak at $\ln(P/P_0)$ near −4 to −5, and a shoulder and a tail at greater energy (*i.e.* at lower values of $\ln(P/P_0)$). For kaolinite, the main peak at low energy could be assigned to the adsorption on basal faces while the shoulder at higher energy and high-energy adsorption peaks could be assigned to the adsorption on edge faces (Villiéras *et al.*, 1992). Further studies demonstrated that the DIS peak attribution for kaolinite could be applied to argon adsorption on other clay minerals including smectites (*e.g.* Villiéras *et al.*, 1992; Perronnet *et al.*, 2007; Sayed Hassan *et al.*, 2006).

Each derivative adsorption isotherm could be fitted using the DIS procedure (Villiéras *et al.*, 1997a; Bardot *et al.*, 1998; Sayed Hassan *et al.*, 2005, 2006; Perronnet *et al.*, 2007) with five characteristic adsorption domains (Figure 3, Table 2). The parameters of the DIS procedure were similar for the samples that were synthesized at 125 and 150ºC (Table 2). In the present case, the total derivative isotherms for clay minerals could be modeled using three BET local-derivative isotherms at greater energies (domains 3−5 in Table 2) which were attributed to the adsorption on the edge surfaces, and two local derivative isotherms at lower energies (domains 1 and 2 in Table 2) which were attributed to adsorption on the basal surfaces.

The derivative curve of the starting gel (Figure 2) differed substantially from those of the nontronites synthesized. Most notably, the derivative curve of the starting gel did not exhibit a clear peak at $\ln(P/P_0)$ at approximately −4 to −5, *i.e.* characteristic of poorly crystallized solids, such as amorphous silica (Villiéras *et al.*, 1998; Rudzinski *et al.*, 1999). Observations by TEM of similar gels revealed that they contain rounded particles, with diameters of ~200 Å, organized as diffuse aggregates (Decarreau *et al.*, 1987). The measured total surface area (*TSA*) of the gel was 127 m^2/g (Table 3), a value corresponding to spherical particles with a diameter of 160 Å, in reasonable agreement with the TEM results. Thus, the edge surface area (*ESA*) and basal surface area (*BSA*) estimates from argon adsorption were irrelevant for the starting gel (Table 3).

For all of the other samples, the peak positions at $\ln(P/P_0) \approx -5$ and at $\ln(P/P_0) \approx -7$ were typical of basal and edge surfaces with Na^+ as surface-exchange-

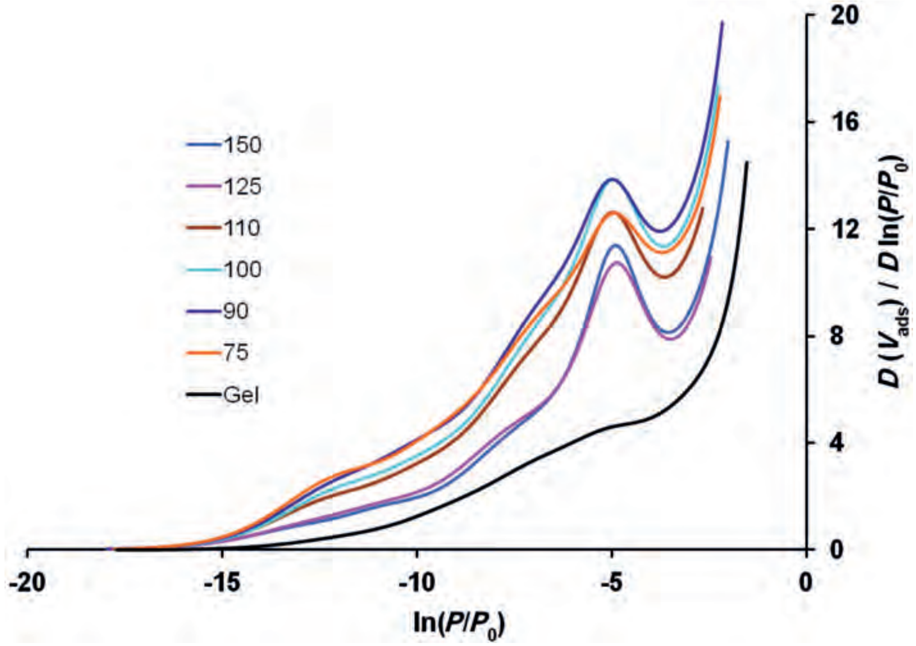

Figure 2. Derivative isotherms of low-pressure argon adsorption at 77 K of synthetic nontronites. The numbers on the key refer to the synthesis temperature (ºC). Gel: starting gel.

able cations (Bardot *et al.*, 1998), as expected given the sample-preparation procedure. The evolution of the lateral interaction parameter ω/kt for domain 2, which ranged from 0.5 for the starting gel to 1.4 for the 150ºC sample, indicated clearly that the surface homogeneity for argon increased with increasing synthesis temperature. Following Villiéras *et al.* (1997b) and Perronnet *et al.* (2007), the number of surface defects or the surface roughness on the basal surfaces of the nontronite samples were assumed to decrease, therefore.

The *BSA*, *ESA*, and *TSA* were calculated on the basis of a 13.8 $\mathring{A}^2$ cross-sectional area for adsorbed argon (Table 3).

Nontronite particles were treated as circular disks to estimate the mean dimensions. The thickness (*H*) and particle length (*D*) of the particles (Table 3) were calculated from the *BSA* and *ESA* using the equations:

$$H = 2/BSA{\cdot}\rho \text{ and } D = 4/ESA{\cdot}\rho \qquad (1)$$

where ρ is the particle density (3.0 g/cm^3 according to the structural formula). Several clear trends appeared

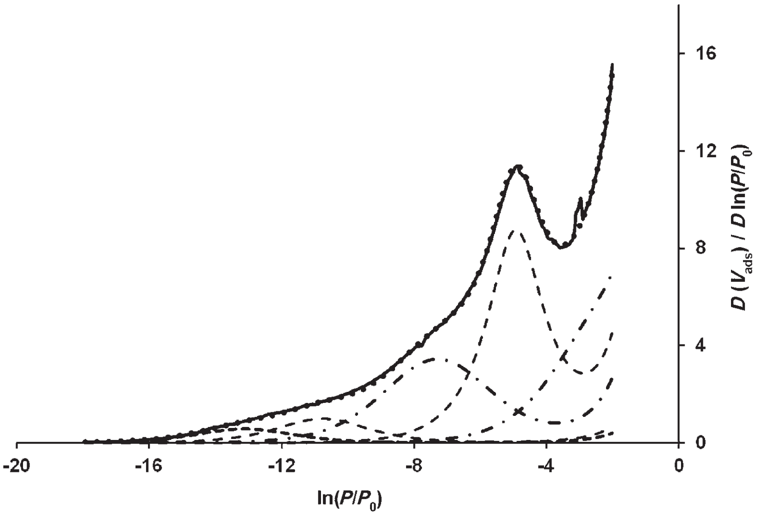

Figure 3. Experimental derivative argon adsorption obtained at 77 K for the nontronite synthesized at 150ºC and its decomposition using the derivative isotherm summation (DIS) method. Solid line: experimental; dotted line: fit; dashed lines: adsorption domains obtained using the DIS procedure.

Table 2. Main parameters obtained from the application of the DIS method to argon adsorption at 77 K on synthesized nontronites.

	DIS domain parameters	Synthesis temperature (ºC)						
		Starting gel	75	90	100	110	125	150
Domain 1	$\ln(P/P_0)$	−2.61	−2.70	−2.61	−2.58	−2.55	−2.40	−2.46
	Vm (cm^3/g)	13.6	21.8	25.1	23.4	19.9	15.0	16.7
	ω/KT	0	0	0	0	0	0	0
Domain 2	$\ln(P/P_0)$	−5.04	−4.95	−5.01	−4.98	−4.98	−4.89	−4.92
	Vm (cm^3/g)	7.9	19.6	23.8	24.5	24.4	23.1	22.1
	ω/KT	0.5	1.1	1.1	1.2	1.1	1.2	1.4
Domain 3	$\ln(P/P_0)$	−6.93	−6.84	−6.93	−6.93	−7.05	−7.44	−7.29
	Vm (cm^3/g)	8.2	23.9	24.7	22.6	20.1	14.8	14.8
	ω/KT	0	0	0	0	0	−0.2	−0.3
Domain 4	$\ln(P/P_0)$	−9.21	−9.48	−9.84	−9.78	−9.87	−10.77	−10.77
	Vm (cm^3/g)	3.4	9.9	9.7	7.8	7.1	4.3	3.7
	ω/KT	0	0	0	0	0	0	0.2
Domain 5	$\ln(P/P_0)$	−11.91	−12.21	−12.27	−12.24	−12.42	−13.02	−13.14
	Vm (cm^3/g)	1.1	8.1	6.6	6.2	5.3	2.3	2.2
	ω/KT	0	0	0	0	0	0	0

$\ln(P/P_0)$: peak position in logarithm of the relative argon pressure unit; Vm (cm^3/g): monolayer capacity; ω/KT: lateral interaction between two neighboring adsorbed molecules.

from these data. The synthesis temperature affected the size and shape of the nontronite particles (Table 3). The *TSA* decreased from 75 to 125ºC and remained fixed between 125 and 150ºC (Figure 4). The decrease in the *TSA* was not related to the last appearance of the gel when the synthesis temperature was increased. In fact, the last appearance of the gel would be expected to promote an increase in the *TSA*. The observed decrease in the *TSA* was related to an increase in the particle size of the smectites synthesized (Decarreau, 1980; Decarreau and Bonnin, 1986; Decarreau *et al.*, 1987). In contrast, the *ESA* and *BSA* (expressed as % of the *TSA*) exhibited opposite trends (Figure 5): between 75 and 125ºC the *BSA* increased whereas the *ESA* decreased, and the *ESA* and *BSA* did not change between 125 and 150ºC. These trends are related to an increase in the particle length, although the thickness did not change significantly (Figure 1). The mean diameter of the synthetic nontronites increased from 86 to 173 Å between 75 and 125ºC and did not increase between 125 and 150ºC. For all of the synthesis temperatures, the mean thickness of the particles remained nearly constant at 40 Å. The d_{001} value was 10 Å under the argon-adsorption experimental conditions. Under these conditions, the mean number of stacked layers for the synthesized nontronites was four, irrespective of the synthesis temperature.

For the nontronite samples that were synthesized at 75 and 100ºC, the maximum amount of remaining gel was 30% (Decarreau *et al.*, 2008). Although the *TSA* of the gel was low, the *TSA* of the nontronite particles was slightly larger because the *TSA* was measured for the entire sample. The derivative adsorption isotherm of the starting gel was fitted by the DIS method using the five absorption domains similar to those of nontronite, in

Table 3. Basal surface area (*BSA*), edge surface area (*ESA*), total surface area (*TSA*) (m^2/g), thickness (*H*), and particle length (*D*) of synthesized nontronite particles obtained from low-pressure argon adsorption data. Values given in italics are *BSA* and *ESA* expressed as a percentage of *TSA*.

Synthesis temperature (ºC)	Starting gel	75	90	100	110	125	150
BSA		154 *50*	182 *53*	178 *56*	164 *57*	142 *64*	143 *65*
ESA		155 *50*	152 *47*	136 *44*	121 *43*	79 *36*	77 *35*
TSA	127	309	333	313	285	221	220
H		43	37	37	41	47	47
D		86	88	98	110	169	173

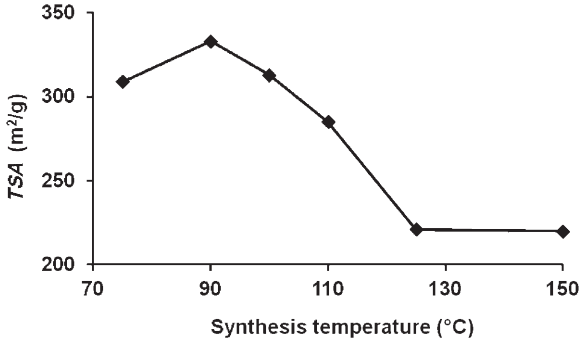

Figure 4. Total surface area (*TSA*) (m^2/g) of nontronite particles (from argon adsorption) *vs.* synthesis temperature.

order to evaluate the gel contribution in argon adsorption on the whole sample (Table 2). The measured *TSA* for each sample was then equal to the sum of the nontronite *TSA* and starting-gel *TSA*. The actual values of the *TSA*, *ESA*, and *BSA* of nontronite could be obtained, using the gel:nontronite weight ratio determined from DTG data and using the data in Table 2, for the five adsorption domains. Using a mixing model, the *TSA* of nontronite would increase but the *ESA*/*BSA* ratio would not change (not shown). This mixing model could not be applied quantitatively because the gel:nontronite weight ratio, as measured by DTG, was not sufficiently precise, and the *TSA* of the remaining untransformed product might have been different from that of the starting gel and might differ from one sample to another.

DISCUSSION

Consistency of data

The XRD data and the argon adsorption data followed the same trend. The parameters measured were in the same range but were not equal (Tables 1, 3; Figure 1).

Both data sets showed an increase in the particle length and CSDS in the (001) plane of nontronite particles synthesized at temperatures from 75 to 125ºC, and these values remained constant for samples prepared at 150ºC. The CSDS that were measured by XRD are slightly greater than the mean particle lengths that were measured by argon adsorption. The XRD data gave the mean length of the crystallographic lattice without any defects (single crystal). The CSDS, in the (001) plane, as measured by XRD, cannot be greater than the particle length of nontronite. The differences between the XRD and argon adsorption data are probably explained by the uncertainties in the measurements.

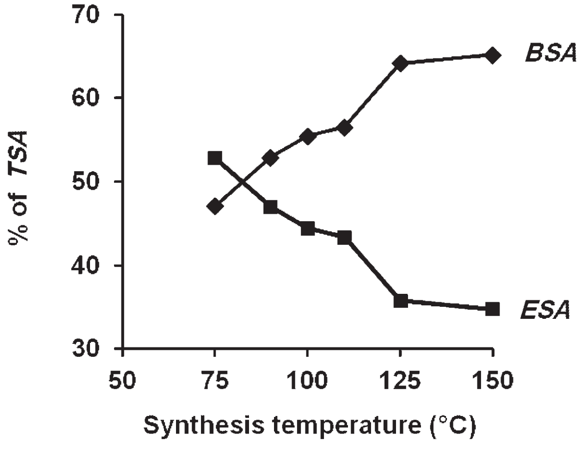

Figure 5. Relative (% of total surface area, *TSA*) ratio of edge surface area (*ESA*) and basal surface area (*BSA*) of nontronite particles (from argon adsorption) *vs.* synthesis temperature.

According to both data sets, the mean number of stacked layers (*N*) in nontronite was four for samples synthesized at temperatures from 75 to 110ºC. For samples prepared at 125 to 150ºC, *N* increased slightly (by <1 layer) according to the argon data and was six according to the powder XRD data. The number of stacked layers, as measured by argon adsorption, was apparently four for all samples. The discrepancy between the XRD and argon adsorption data may be related to inter-particle diffraction (Eberl *et al.*, 1998) for nontronites prepared at higher temperatures. Argon adsorption appears to reflect the actual size and shape of the nontronite particles better than the values obtained from the XRD data.

Crystal growth of smectites

Synthesized nontronite crystal growth. Because nontronite is the only mineral phase that can precipitate under the experimental conditions used (Decarreau *et al.*, 2008; Andrieux and Petit, 2010), the chemical evolution of the system involves only the nucleation and growth of nontronite. The influences of the synthesis duration and temperature on similar nontronite crystallization were studied by Decarreau (1980) and Decarreau *et al.* (1987). The smectite crystal size within the (001) plane was time dependent, and the kinetics of crystal growth followed the Arrhenius equation (Carrado *et al.*, 2006). The mean particle length (*D*), within the (001) plane was:

$$D = \mathrm{A} \cdot \exp\left(-E/\mathrm{R}T\right) \cdot t$$

where *t* is time and *T* is absolute temperature. For the present experiments, time and temperature played analogous roles. Syntheses performed at increased temperatures with a fixed aging time were analogous to syntheses performed at a fixed temperature with increased aging times. In the present work, as the synthesis temperature increased, the number of stacked layers did not increase significantly, although the mean length of the particles doubled. This observation suggests that the crystal growth was dominated by the lateral extension of the synthesized nontronite layers. This lateral extension measured for the synthetic nontronites is a crystal-growth process that differs from those usually described for clay minerals that are more three-dimensional, such as kaolinite, chlorite, and mica. Polygonal and/or broadly circular spiral-growth patterns have often been observed on the growth surfaces of biotite (Amelinks, 1952), phlogopite (Baronnet, 1972), illite (Inoue and Kitagawa, 1994; Kitagawa, 1998), rectorite (Kitagawa, 1997), kaolinite (Sunagawa and Koshino, 1975), and mixed-layer illite-smectite (Kitagawa and Matsuda, 1992). Two-dimensional nucleation was observed on the (001) growth surfaces of sudoite (Jige *et al.*, 2003), which produced an increase in the number of stacked layers. The latter crystal-growth process is less commonly observed because a greater degree of fluid oversaturation is required.

Using the periodic bond chain (PBC) theory of Hartman (1973), a large number of defects in clay minerals was suggested by Meunier (2010) to disrupt the PBCs, thus precluding crystal growth. The PBCs present in this study were those within the (001) plane, *i.e.* the PBCs of [100], [110], and [$\bar{1}$10]. Following Meunier (2010), the PBC theory of Hartman (1973) suggests implicitly a crystal-growth process of clay minerals essentially bi-dimensional within the (001) plane, which was observed for the synthetic nontronites here.

During crystal growth, an increase in the particle size entailed a decrease in the *TSA* per unit mass. For a constant number of stacked layers in the clay particles, the *BSA* per unit mass is constant during crystal growth (*H* = constant in relation 1), and a decrease in the *TSA* is only due to a decrease in the *ESA*. This relation was observed for the synthesized nontronites (Table 3): the *BSA* fluctuated around a mean value of 160 m^2/g, whereas the *ESA* decreased continuously from 115 to 77 m^2/g. The theoretical values of the *TSA* for circular particles, having a constant 40 Å thickness, were calculated as a function of the particle diameter (Figure 6). The measured *TSA* of the synthetic nontronites, obtained by the DIS procedure from the argon adsorption curves, fitted the theoretical curve well (Figure 6).

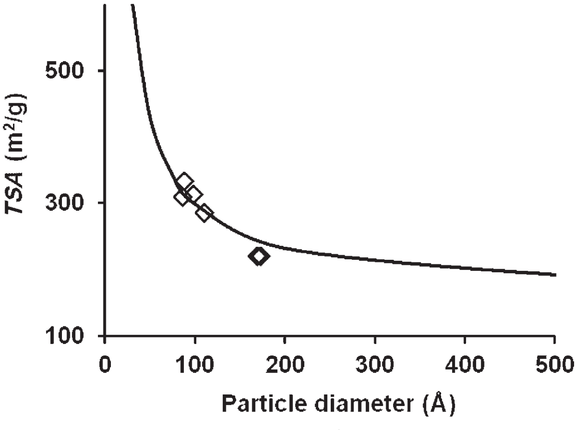

Figure 6. Total surface area (*TSA*) (m^2/g) of nontronite particles *vs.* their mean particle length. Solid line: theoretical *TSA* calculated for circular particles with a constant thickness of 40 Å. Open diamonds: *TSA* values measured from argon adsorption.

The work above demonstrated that the crystal growth of the synthetic nontronites occurred *via* the addition of material ('building blocks') to the edges of particles, mainly. These 'building blocks' were probably less than four layers thick but their structure could not be determined in detail. Consequently, the stacked layers might not have the same planar extension, inducing local strength. This crystal growth may explain the rolled edges of the particles as observed by TEM (Decarreau *et al.*, 2008).

The crystal growth of the nontronites was similar for samples prepared at 125 and 150ºC. Because nontronite becomes unstable and aegirine occurs at higher temperatures (Decarreau *et al.* 2004), long synthesis times (*i.e.* several years, Decarreau *et al.*, 1987) would be required to obtain larger crystals experimentally.

Effect of particle size on OH-stretching vibrations. The ν OH bandwidth in infrared spectra is partially linked to the size of particles due to the "crystallinity" effect (Petit *et al.*, 2004, 2008). A decrease in the ν Fe_2^{3+}-OH band width in IR spectra of synthetic nontronites was noted by Decarreau *et al.* (2008) when the synthesis temperature increased. The plot of the ν Fe_2^{3+}-OH band width *vs.* the mean particle length, obtained from argon adsorption, revealed that the band width reached a plateau at 45 cm^{-1} from a particle length of ~180 Å (Figure 7).

Comparison with other synthetic smectites. The crystal growth of plate-shaped smectite *via* the lateral extension of layers is in agreement with the data from Decarreau (1980) and Decarreau *et al.* (1987). In these previous studies, the CSDS of synthetic Mg-smectite (stevensite) and of various synthetic nontronites were measured. The authors observed a small increase in the number of stacked layers (from two to six) and an increase along the (001) plane with an increase in the synthesis time or temperature.

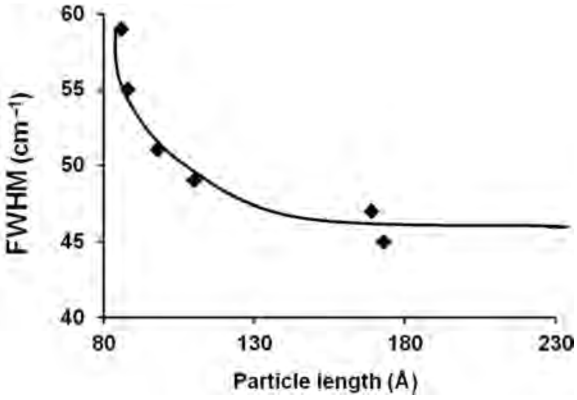

Figure 7. Full width at half maximum (FWHM) of the ν Fe_2^{3+}-OH band observed on the MIR spectra of synthetic nontronites *vs.* the mean length of the particles.

Synthetic saponite (Michot and Villiéras, 2002) and montmorillonite (Le Forestier *et al.*, 2010) were also studied using low-pressure argon adsorption. Syntheses were performed for four weeks at 400ºC at 1 kbar (various charges) for the saponite series and at 350ºC and 1.2 kbar for montmorillonite. The derivative adsorption curves were similar to those of the synthetic nontronite presented here. The saponite particles were 200−600 nm wide (mean of 315 nm) and 17−39 nm thick (mean of 25 nm). These synthetic saponite crystals were ~20 times greater in the lateral dimension and only six times thicker than the largest nontronites synthesized here. The montmorillonite synthesized was 65 nm in-plane and 12 nm thick. Unfortunately, these synthetic saponite samples and montmorillonite were obtained for only one aging time and only one temperature; consequently, the crystal-growth process could not be deduced. Nevertheless, even for synthesis temperatures >300ºC, synthetic smectites contained 12−39 stacked layers which resulted in a thickness much smaller than the plane extension.

Despite the high synthesis temperature, the montmorillonite particles were only three to four times larger than the nontronite particles studied, and had a similar *H*/*D* ratio. For dioctahedral smectites (*e.g.* montmorillonite and nontronite) a moderate increase in synthesis temperature (or time) did not result in a significant increase in the particles size. In contrast, large smectite crystals were synthesized under extreme conditions by Nakasawa *et al.* (1992).

Trioctahedral smectite particles were shown by Decarreau (1980, 1983) and Decarreau *et al.* (1987) to be generally larger than dioctahedral smectite particles in samples prepared under similar synthesis conditions. Accordingly, argon adsorption measurements revealed that saponite particles were significantly larger (ten times) than the montmorillonite particles that were synthesized under similar conditions (Michot and Villiéras, 2002; Le Forestier *et al.*, 2010).

Syntheses performed in the temperature range of weathering or hydrothermal systems indicated that the small size of dioctahedral smectites was constrained by the crystal-growth processes.

Comparison with natural smectites. The particle morphologies of various natural smectites have been studied using low-pressure argon adsorption, including those of MX80 montmorillonite (Tournassat *et al.*, 2003), two montmorillonites and one nontronite (Fe^{3+}-rich beidellite) (Perronnet *et al.*, 2007), and SWy2 montmorillonite samples (Le Forestier *et al.*, 2010). These smectites were derived from bentonites, which resulted from the interaction of volcanic ash falls and ocean water (Moll, 2001; Christidis and Huff, 2009). From the oxygen and hydrogen isotopic data (Arslan *et al.*, 2010 and references therein), bentonites were determined to form at relatively low temperatures (<100ºC). The particles of these natural smectites have a size range similar to those of synthetic dioctahedral smectites, though the MX80 and SWy2 smectites contained additional stacked layers (28 nm and 34 nm thick, respectively) compared to synthetic smectites (11−15 nm thick) according to Perronnet *et al.* (2007).

The data that were obtained for natural bentonites are in agreement with the data from experimental systems (Meunier, 2006), suggesting similar crystal-growth processes.

Clay minerals that form at the Earth's surface and under sub-surface conditions exhibit a small particle size, whereas the associated minerals are generally not as small. The PBC theory (Hartman, 1973) was suggested by Meunier (2006) to be applicable to clay minerals, thus precluding their crystal growth. Implicitly, the crystal growth of clay minerals is essentially two-dimensional (Meunier, 2006) (see above) as demonstrated here both for natural and synthetic smectites.

Smectite crystal-growth mechanisms. As far as the authors are aware, no data on the crystal-growth mechanisms of smectites are available in the literature. The only permanent portion of the smectite structure is the layer because the interlayer can vary in both size and chemistry, depending on the chemistry of the surrounding fluid. Consequently, crystal-growth mechanisms in three dimensions (*e.g.* polygonal and spiral-growth patterns) are unlikely to occur for smectite. The crystal-growth pattern that was determined for synthetic nontronite, *i.e.* the lateral growth of the layer only, probably occurs for synthetic and natural dioctahedral smectites. This conclusion is suggested by the similarity of the morphologies of natural and synthetic dioctahedral smectite. For synthetic nontronite, the number of stacked layers (*i.e.* four) can crystallize during the nucleation stage of crystal growth or slightly afterward; smectites that were synthesized over a few days at 25ºC exhibited a broad 001 XRD reflection due to three or four stacked layers (Decarreau, 1980, 1983; Decarreau and Bonnin, 1986; Decarreau *et al.*, 1987). For natural smectite and smectites that were synthesized at higher temperatures, particles with 10 to 40 stacked layers may represent another crystal-growth process. The AFM images of the MX 80 sample (Tournassat *et al.*, 2003) showed broadly circular "islands" on the (001) surfaces of isolated particles 10−200 nm wide. These islands were one layer thick. This feature was consistent with the close-step pattern of two-dimensional growth, which led to an increase in the number of stacked layers. Such a growth pattern was observed for metamorphic mica (Sunagawa and Koshino, 1975) and hydrothermal sudoite (Jige *et al.*, 2003). However, only two-dimensional crystal-growth processes occur during smectite formation. The remaining questions are as follows: what is the crystal-growth unit (building block) and does this unit include an interlayer cation? For epitaxial growth of trioctahedral clay, nucleation began *via* the formation of a hydroxide sheet on which silica was adsorbed (Manceau *et al.*, 1999; Rainer *et al.*, 2002; Schegel *et al.*, 2001). This model, proposed by Caillère *et al.* (1956, 1957) and often used since, was based on the similarity of structures of trioctahedral Mg, Ni, and Co hydroxides and the analogous octahedral sheet of trioctahedral clay minerals. The process was different for dioctahedral structures (Decarreau, 1983). The building blocks were demonstrated to be [Si tetrahedra-Al (or Fe) octahedra-Si tetrahedra] 'monomers' for TOT dioctahedral clays (Siffert, 1962). These monomers might be the smaller building block for the crystal growth of dioctahedral TOT clays (White and Zelazny, 1988).

ACKNOWLEDGMENTS

The authors thank an anonymous reviewer, Douglas McCarty, and Utpalendu Kuila for their constructive comments that helped to improve the manuscript.

REFERENCES

Amelinckx, S. (1952) La croissance hélicoïdale de cristaux de biotite. *Comptes Rendus de l'Académie des Sciences, Paris*, **234**, 971–973.

Andrieux, P. and Petit, S. (2010) Hydrothermal synthesis of dioctahedral smectites: The Al-Fe chemical series. Part I: Influence of experimental conditions. *Applied Clay Science*, **48**, 5–17.

Arslan, M., Abdioglu, E., and Kadir, S. (2010) Mineralogy, geochemistry and origin of bentonite in upper cretaceous pyroclastic units of the Tirebolu area, Giresun, northeast Turkey. *Clays and Clay Minerals*, **58**, 120–141.

Bauer, A., Lanson, B., Ferrage, E., Emmerick, K., Taubald, H., Schield, D., and Velde, B. (2006) The fate of smectite in KOH solution. *American Mineralogist*, **91**, 1313–1322.

Bardot, F., Villiéras, F., Michot, L.J., François, M., Gérard, G., and Cases, J.M. (1998) High resolution gas adsorption study on illites permuted with various cations: assessment of surface energetic properties. *Journal of Dispersion Science and Technology*, **19**, 739–759.

Baronnet, A. (1972) Growth mechanisms and polytypism in synthetic hydroxyl bearing phlogopite. *American Mineralogist*, **47**, 605–616.

Bickmore, B.R., Bosbach, D., Hochella, M.F., Charlet, L., and Rufe, F. (2001) In situ atomic force microscopy study of hectorite and nontronite dissolution: Implications for phyllosilicates edge surface structures and dissolution mechanisms. *American Mineralogist*, **86**, 411–423.

Brindley, G.W. and Brown, G. editors (1980) *Crystal Structure of Clay Minerals and their X-ray Identification.* Monograph **5**, Mineralogical Society, London.

Caillère, S., Henin, S., and Esquevin, J. (1956) Etude expérimentale du mécanisme de la formation des antigorites nickellifères. *Bulletin de la Société Française de Minéralogie Cristallographie*, **79**, 408–421.

Caillère, S., Henin, S., and Esquevin, J. (1957) Synthèse des minéraux argileux. *Bulletin du Groupe Français des Argiles*, **9**, 67–76.

Carrado, K., Decarreau, A., Petit, S., Bergaya, F., and Lagaly, G. (2006) Synthetic clay minerals and purification of natural clays. Pp. 115–139 in: *Handbook of Clay Science* (F. Bergaya, B.K.G. Theng, and G. Lagaly, editors). Elsevier, Amsterdam.

Christidis, G.E. (2001) Formation and growth of smectites in bentonites: a case study from Kimols Island, Aegean, Greece. *Clays and Clay Minerals*, **49**, 204–215.

Christidis, G.E. and Huff, W.D. (2009) Geological aspects and genesis of bentonites. *Elements*, **5**, 93–98.

Decarreau, A. (1980) Cristallogenèse expérimentale des smectites magnésiennes: hectorites, stévensites. *Bulletin de Minéralogie*, **103**, 579–590.

Decarreau, A. (1983) Etude expérimentale de la cristallogenèse des smectites. Mesure des coefficients de partage smectite trioctaèdrique – solution aqueuse pour les métaux M^{2+} de la première série de transition. *Sciences Géologiques*, Mémoire nº**74**, 185 pp.

Decarreau, A. and Bonnin, D. (1986) Synthesis and crystallogenesis at low temperature of Fe(III)-smectites by evolution of coprecipitated gels: experiments in partially reducing conditions. *Clay Minerals*, **21**, 861–877.

Decarreau, A., Bonnin, D., Badaut-Trauth, D., Couty, R., and Kaiser, P. (1987) Synthesis and crysytallogenesis of ferric smectite by evolution of Si-Fe coprecipitation in oxidizing conditions. *Clay Minerals*, **22**, 207–223.

Decarreau, A., Petit, S., Vieillard, Ph., and Dabert, N. (2004) Hydrothermal synthesis of aegirine at 200ºC. *European Journal of Mineralogy*, **16**, 85–90.

Decarreau, A., Petit, S., Martin, F., Farges, F., Vieillard, Ph., and Joussein, E. (2008) Hydrothermal synthesis, between 75 and 150ºC, of high charge ferric nontronites. *Clays and Clay Minerals*, **56**, 322– 337.

Eberl, D.D., Drits V.A., and Środoń, J. (1998) Deducing growth mechanism for minerals from the shapes of crystal size distributions. *American Journal of Science*, **298**, 499–533.

Güven, N. (1988) Smectites. Pp. 497–559 in: *Hydrous Phyllosilicates (exclusive of Micas)* (S.W. Bailey, editor). Reviews in Mineralogy, **19**, Mineralogical Society of America, Washington DC.

Hartman, P. (1973) Structure and morphology. Pp. 367–402 in: *Crystal Growth: an Introduction* (P. Hartman, editor). North Holland Publications, Amsterdam.

Inoue, A. and Kitagawa, R. (1994) Morphological characteristics of illitic clay minerals from a hydrothermal system. *American Mineralogist*, **79**, 700–711.

Jige, M., Kitagawa, R., Zaykov, V.V. and Sinyakovskaya, I. (2003) Surface microtopography of sudoite. *Clay Minerals* **38**, 375–382.

Kitagawa, R. (1997) Surface microtopography of rectorite (allevardite) from Allevard, France. *Clay Minerals*, **29**, 709–715.

Kitagawa, R. (1998) Surface microtopography of illite crystals from different modes of occurrence. *The Canadian Mineralogist*, **36**, 1559–1567.

Kitagawa, R. and Matsuda, T. (1992) Microtopography of regularly interstratified mica and smectite. *Clays and Clay Minerals*, **40**, 114–121.

Kloprogge, J.T., Komarneni, S., and Amonette, J.E. (1999) Synthesis of smectite clay minerals: a critical review. *Clays and Clay Minerals*, **47**, 529–554.

Kuwahara, Y. (2006) In-situ AFM study of smectite dissolution under alkaline conditions at room temperature. *American Mineralogist*, **91**, 1142–1149.

Le Forestier, L., Muller, F., Villiéras, F., and Pelletier, M. (2010) Textural and hydration properties of a synthetic montmorillonite compared with a natural Na-exchanged clay analogue. *Applied Clay Sciences*, **48**, 18–25.

Manceau, A., Schlegel, M.L., Nagy, K.L., and Charlet, L. (1999) Evidence of the formation of trioctahedral clay upon sorption of Co^{2+} on quartz. *Journal of Colloid and Interface Science*, **220**, 181–197.

Meunier, A. (2006) Why are clay minerals small? *Clay*

Minerals, **41**, 551–556.

Meunier, A. (2010) Formation mechanisms of mixed-layer clay minerals. Pp. 53–71 in: *Interstratified Clay Minerals: Origin, Characterization and Geochemical Significance* (S. Fiore, J. Cuadros, and J. Huertas, editors). AIPEA Educational series, Nº**1**.

Michot, L.J. and Villiéras, F. (2002) Assessment of surface energetic heterogeneity of synthetic Na-saponite. The role of layer charge. *Clay Minerals*, **37**, 39–57.

Michot, L.J. and Villiéras, F. (2006) Surface and porosity. Pp. 965–978 in: *Handbook of Clay Science* (F. Bergaya, B.K.G. Theng, and G. Lagaly, Editors). Elsevier, Amsterdam.

Michot, L.J., François, M., and Cases, J.M. (1990) Surface heterogeneity studied by a quasi-equilibrium adsorption procedure. *Langmuir*, **6**, 637–643.

Moll Jr., W.F. (2001) Baseline studies of The Clay Minerals Society Source Clays: geological origins. *Clays and Clay Minerals*, **49**, 374–380.

Moore, D.M. and Reynolds, R.C. (1989) *X-ray Diffraction and the Identification and Analysis of Clay Minerals*. Oxford University Press, New York.

Nakasawa, H., Yamada, H., and Fujita, T. (1992) Crystal synthesis of smectite applying very high pressure and temperature. *Applied Clay Science*, **6**, 395–401.

Peronnet, M., Villiéras, F., Jullien, M., Razafitianamaharavo, A., Raynal, J., and Bonnin D. (2007) Towards a link between the energetic heterogeneities of the edge faces of smectites and their stability in the context of metallic corrosion. *Geochimica et Cosmochimica Acta*, **71**, 1463–1479.

Petit, S., Martin, F., Wiewióra, A., De Perseval, P., and Decarreau, A. (2004) Crystal-chemistry of talc: A near infrared (NIR) spectroscopy study. *American Mineralogist*, **89**, 319–326.

Petit, S., Righi, D., and Decarreau, A. (2008) Transformation of synthetic Zn-stevensite to Zn-talc induced by the Hoffmann-Klemen effect. *Clays and Clay Minerals*, **56**, 645–654.

Rainer, D., Scheidegger, A.M., Manceau, A., Schlegel, M., Baeyens, B., Bradbury, M.H., and Morales, M. (2002) Neoformation of Ni phyllosilicates upon Ni uptake on montmorillonite: a kinetic study by powder and polarized extended X-ray absorption fine structure spectroscopy. *Geochimica et Cosmochimica Acta*, **66**, 2335–2347.

Rudzinski, W., Charmas, R., Piasecki, W., Prélot, B., Thomas, F., Villiéras, F., and Cases, J.M. (1999) Calorimetric effects of simple ion adsorption at silica/ electrolyte interface: A quantitative analysis of surface energetic heterogeneity. *Langmuir*, **15**, 5977–5983.

Sayed Hassan, M., Villiéras, F., Razafitianamaharavo, A., and Michot, L.J. (2005) Geometrical and energetic heterogeneity of kaolinites. The role of exchangeable cations on argon adsorption energy distribution. *Langmuir*, **21**, 12283–12289.

Sayed Hassan, M., Villiéras, F., Gaboriaud, F., and Razafitianamaharavo, A. (2006) AFM and low-pressure argon adsorption analysis of geometrical properties of phyllosilicates. *Journal of Colloid and Interface Science*, **296**, 614–623.

Schlegel, M.L., Manceau, A., Charlet, L., Chateigner, D., and Hazeman, J.L. (2001) Sorption of metal ions on clay minerals. Nucleation and epitaxial growth of Zn phyllosilicate on the edges of hectorite. *Geochimica et Cosmochimica Acta*, **65**, 4155–4170.

Siffert, B. (1962) Quelques réactions de la silice en solution: la fomation des argiles. *Mémoires Service Carte Géologique Alsace Lorraine*, **253**, 142–144.

Środoń, J., Eberl, D.D., and Drits, V.A. (2000) Evolution of fundamental-particle size during illitization of smectite and implications for reaction mechanism. *Clays and Clay Minerals*, **48**, 446– 458.

Sunagawa, I. and Koshino, Y. (1975) Growth spirals on kaolin group minerals. *American Mineralogist*, **60**, 407–412.

Tournassat, C., Neaman, A., Villiéras, F., Bosbach, D., and Charlet, L. (2003) Nano morphology of montmorillonites particles: estimation of the clay edge sorption site density by low-pressure gas adsorption and AFM observations. *American Mineralogist*, **88**, 1989–1995.

Villiéras, F., Cases, J.M., François, M., Michot, L.J., and Thomas, F. (1992) Texture and surface energetic heterogeneity of solids from modeling of low pressure gas adsorption isotherms. *Langmuir*, **8**, 1789–1795.

Villiéras, F., Michot, L.J., Bardot, F., Cases, J.M., François, M., and Rudzinsky, W. (1997a) An improved derivative isotherm summation method to study surface heterogeneity of clay minerals. *Langmuir*, **13**, 1104–1117.

Villiéras, F., Michot, L.J., Cases, J.M., Berend, I., Bardot, F., François, M., Gérard, G., and Yvon, J. (1997b) Static and dynamic studies of the energetic surface heterogeneity of clay minerals. Pp. 573–623 in: *Equilibria and Dynamics of Gas Adsorption on Heterogeneous Solid Surfaces* (W. Rudzinski, W.A. Steele, and G. Zgrablich, editors). Studies in Surface Science and Catalysis, **104**, Elsevier Science Publishers B.V., Amsterdam.

Villiéras, F., Leboda, R., Charmas, B., Bardot, F., Gérard, G., and Rudzinski, W. (1998) High resolution Ar and N_2 assessment of carbosils surface heterogeneity. *Carbon*, **36**, 1501–1510.

Villiéras, F., Michot, L.J., Bardot, F., Chamerois, M., Eypert-Blaison, C., Gérard, G. and Cases, J.M. (2002) Surface heterogeneity of minerals. *Comptes Rendus Geoscience*, **334**, 597–609.

White, G.N. and Zelazny, L.W. (1988) Analysis and implications of the edge structure of dioctahedral phyllosilicates. *Clays and Clay Minerals*, **36**, 141–146.

Zhang, D., Zhou, C., Lin, C., Tong, D., and Yu, W. (2010) Synthesis of clay minerals. *Applied Clay Science*, **50**, 1–11.

(*Received 23 August 2013; revised 30 April 2014; Ms. 702; AE: H. Dong*)

Clays and Clay Minerals, Vol. 62, No. 2, 112–125, 2014.

THE TIMING OF DIAGENESIS AND THERMAL MATURATION OF THE CRETACEOUS MARIAS RIVER SHALE, DISTURBED BELT, MONTANA

Stephen G. Osborn[1,2], Louise Totten Duffield[3,5], W. Crawford Elliott[2,*], J. M. Wampler[2,4], R. Douglas Elmore[5], and Michael H. Engel[5]

[1] Department of Geological Sciences, California State Polytechnic University, Pomona, CA 91768, USA
[2] Department of Geosciences, Georgia State University, Atlanta, GA 30302-4105, USA
[3] Anadarko Petroleum Corporation, 1201 Lake Robbins Drive, The Woodlands, TX 77380, USA
[4] School of Earth and Atmospheric Sciences, Georgia Institute of Technology, Atlanta, GA 30332-0340, USA
[5] ConocoPhillips School of Geology and Geophysics, University of Oklahoma, Norman, OK 73019, USA

Abstract—The hypothesis that chemical remanent magnetization (CRM) in argillaceous rocks may be due to release of Fe during smectite illitization has been tested by study of spatial and temporal relationships of CRM acquisition, smectite illitization, and organic-matter maturation to deformation in the Montana Disturbed Belt. New K-Ar ages and stacking order and percentages of illite layers in illite-smectite (I-S) are consistent with conclusions from previous studies that smectite illitization of bentonites in Subbelts I and II of the Disturbed Belt was produced by thrust-sheet burial resulting from the Laramide Orogeny. Internally concordant, early Paleogene, K-Ar age values (55−57 Ma) were obtained from clay sub-fractions of thick bentonites which were significantly different in terms of their ages (*i.e.* Jurassic Ellis Formation and late Cretaceous Marias River Shale), further supporting a model of smectite illitization as a result of the Laramide Orogeny. Internally concordant K-Ar ages were found also for clay sub-fractions from a thick bentonite at Pishkun Canal (54 Ma) and from an undeformed bentonite near Vaughn on the Sweetgrass Arch (48 Ma). In Subbelts I and II, a greater degree of smectite illitization corresponds to increased thermal maturation, increased natural remanent magnetization intensity, and increased deformation (dip of beds). A dissolution−precipitation model over a short duration is proposed for the formation of illite layers in Subbelts I and II. A characteristic remanent magnetization was developed before or just after folding began in the early Paleogene. More smectite-rich I-S, low thermal maturity, and the absence of a CRM were noted in one outcrop of an undeformed rock on the Sweetgrass Arch. Strontium isotope data allow for the possibility that internal or externally derived fluids may have influenced illitization, but the K-Ar age values suggest that illitization was probably in response to conductive heating after the overthrusting had occurred. The differences in K-Ar dates among the bentonites studied herein may be due to differences in the timing of peak temperature related to differences in distance below the overthrust slab, in rates of burial and exhumation, and in initial temperature.

Key Words—Illite, K-Ar, Montana Disturbed Belt, Remagnetization, Thermal Maturity.

INTRODUCTION

A number of methods provide useful information about the thermal maturity of petroleum source rocks in sedimentary basins. These methods include the study of (1) diagenetic inorganic minerals (clays, oxides, carbonates), (2) organic geochemical parameters (vitrinite reflectance, time-temperature index, biomarkers), (3) the timing of diagenetic mineral transformations (from isotopic dating and remanent magnetization), (4) the geochemistry of basin brines, and (5) constructed burial curves and numerical models simulating burial temperatures. Knowledge of the timing of thermal maturation relative to that of the formation of suitable traps for crude oil and natural gas is critical for successful hydrocarbon exploration (Pevear, 1999).

The degree of illitization of smectite, indicated by the type of stacking order and the percentage of illite layers in diagenetic mixed-layered illite-smectite (I-S), is well known as a gauge of thermal maturity in basins where conversion of smectite to illite (smectite illitization) was caused by burial, and the timing of the illitization can be determined by K-Ar dating (Hoffman *et al*., 1976; Hower *et al*., 1976; Hoffman and Hower, 1979; Elliott *et al*., 1991; Pollastro, 1994; Pevear, 1999; Clauer and Lerman, 2012; Stroker *et al*., 2013, Środoń *et al*., 2013). Smectite illitization also occurs in accretionary wedges, near igneous intrusions (by contact metamorphism or hydrothermal activity), and in other settings where the transformation is prompted by increases in temperature and potassium concentration (Aronson and Lee, 1986; Nadeau and Reynolds, 1981; Schoonmaker *et al*., 1986; Elliott and Matisoff, 1996; Bauluz *et al*., 2002; Kim and Peacor, 2002; Clauer, 2006; Derkowski *et al*., 2013). Externally derived fluids can cause diagenetic changes, particularly in mountain belts (Garven and Freeze, 1984; Oliver, 1986; Osborn *et al*., 2012). These external fluids

---

* E-mail address of corresponding author:
wcelliott@gsu.edu
DOI: 10.1346/CCMN.2014.0620204

influence clay diagenesis in foreland basins adjacent to tectonic highlands (Morton, 1985; Elliott and Aronson, 1987; Elliott and Aronson, 1993; Ziegler and Longstaffe, 2000; Elliott and Haynes, 2002; Środoń *et al.*, 2009). The conversion of smectite to illite proceeds either by solid-state transformation or dissolution-precipitation reactions; the latter mechanism prevails in fluid-dominated systems (Altaner and Ylagan, 1997).

The conversion of smectite to illite can release iron, which in turn precipitates as authigenic magnetite (Katz *et al.*, 2000). Such authigenic magnetite can hold a measureable chemical remanent magnetization (CRM), the timing of which is relatable to the apparent polar wandering curve (Katz *et al.*, 2000; Gill *et al.*, 2002; Woods *et al.*, 2002; Tohver *et al.*, 2008; Elmore *et al.*, 2012). Thus, a CRM can provide another basis for establishing the timing of diagenetic processes in argillaceous rocks, in particular where the timing of potassic diagenesis is difficult to determine in the clay fraction due to the presence of detrital I-S or detrital illite (Elliott *et al.*, 2006a; Tohver *et al.*, 2008; Zwing *et al.*, 2009).

The Disturbed Belt in northwestern Montana is a good place to investigate the controls on clay diagenesis. The eastern and central parts of the Disturbed Belt consist of generally NW−SE trending folded and thrust-faulted Paleozoic and Mesozoic rocks. The last episode of disturbance was the late Cretaceous through early Paleogene Laramide Orogeny, which deformed Devonian−Cretaceous rocks (Mudge, 1982). To the east, the Disturbed Belt is bounded by gently folded Mesozoic rocks on the Sweetgrass Arch. Diagenesis in the Cretaceous rocks can be fit into a well known context of burial and thermal history. Clay-mineral thermometry was well established in an earlier study of the Disturbed Belt (Hoffman and Hower, 1979). Preliminary studies suggested that CRM in the Disturbed Belt Cretaceous rocks could be related to illitization, although other remagnetization mechanisms are possible (Gill *et al.*, 2002; Elliott *et al.*, 2006b).

I-S from Cretaceous shales and bentonites in the Disturbed Belt was studied by Hoffman and Hower (1979) and Hoffman *et al.* (1976) who found that ordered I-S with a high percentage of illite layers (>60% in most cases) was the most common clay mineral. Diagenetic illite formed in response to heating due to thrust sheet burial, according to Hoffman *et al.* (1976), and those authors used K-Ar ages of I-S to suggest that the thrusting had ended in the Paleocene. In almost undeformed stratigraphically equivalent units on the Sweetgrass Arch to the east, the clay fractions are dominated by randomly interstratified I-S with a high proportion of smectite layers (>70% in most cases), which indicates maximum burial temperatures of ~50ºC (Hoffman *et al.*, 1976; Hoffman and Hower, 1979). The smectite-to-illite transformation in a 2.5 m-thick bentonite in the Sun River Canyon was studied by Altaner *et al.* (1984) who found that the percentage of illite layers and K-Ar ages of I-S decreased together from the edge (54 Ma) to the center (50 Ma) of this bentonite. These data were used to derive a model for diffusive transport of potassium and the formation of illite in thick bentonites (Altaner, 1989). The clay fractions of many samples collected from a ~2 m-thick bentonite from the Sun River Canyon (near Pishkun Canal) contained both R1 I-S and R0 I-S (McCarty *et al.*, 2009). (The R descriptor is the Reichweite notation to denote the type of stacking order in I-S and other mixed-layered clay minerals; Jagodzinski, 1949; Moore and Reynolds, 1997). The center of this thick bentonite contained more R0 I-S and less R1 I-S than did the edges, but the percentage of illite layers in each of these kinds of I-S was the same throughout the bentonite. The I-S in this thick potassium bentonite was formed by simultaneous nucleation and growth according to Eberl *et al.* (2011). The diffraction patterns showing separate R1 I-S and R0 I-S (McCarty *et al.*, 2009) can be explained as interparticle diffraction. The illite clay mineralogy of this thick potassium bentonite consists of continuous distributions of illite and smectite crystals (Eberl *et al.*, 2011).

A temporal relationship between clay diagenesis and remagnetization was sought by Gill *et al.* (2002) who compared results from several different Mesozoic units in the Disturbed Belt with results from equivalent smectite-rich strata on the adjacent Sweetgrass Arch. The Disturbed Belt rocks contain a pre-folding or early syn-folding, reversed, Paleogene magnetization that is interpreted to be a CRM residing in magnetite and perhaps pyrrhotite. The rocks on the Sweetgrass Arch have weak magnetization and do not contain the CRM (Gill *et al.*, 2002). A presence-absence test and the timing of acquisition of the CRM suggested that magnetite authigenesis could have been causally related to the conversion of smectite to illite. Support for such a relation was added by Elliott *et al.* (2006b) by finding that the timing of CRM acquisition in limestone concretions of the Cretaceous Marias River Shale is consistent with K-Ar ages of diagenetic illite from a thick (30 cm) bentonite near concretion beds. A late Jurassic to early Paleogene CRM that resides in magnetite in the Mississippian Madison Group carbonates of the Disturbed Belt was found by O'Brien *et al.* (2007). The CRM is pre-tilting in the thrust sheets and one anticline with a fault-bend geometry but syn-tilting in two fault-propagation folds. Petrographic and geochemical studies indicated that this CRM is related to evolved fluids that carried radiogenic Sr or to hydrocarbons (O'Brien *et al.*, 2007).

Building on these past efforts, the present study was intended to test further the hypothesis that CRM acquisition in the Disturbed Belt was caused by smectite illitization, by more detailed investigation than before of how CRM acquisition, illitization, and organic maturation were spatially and temporally related to deformation in the Disturbed Belt. The Upper Cretaceous (Cenomanian to mid-Santonian), marine Marias River Shale, which overlies unconformably the lower Cretaceous Blackleaf Formation and consists predominantly of dark gray shale that is up to ~400 m thick. A few samples from the Blackleaf Formation and the Jurassic Ellis Formation were also investigated. Thus, some new K-Ar age values from bentonites (Jurassic Ellis Formation at Swift Dam, Cretaceous Marias River Shale at Badger Creek) and new paleomagnetic data from limestone concretions in the Marias River Shale (at Badger Creek) are presented and integrated with K-Ar and paleomagnetic data from Pishkun Canal (Elliott *et al*., 2006b) to further elucidate the remagnetization mechanism(s). These data are integrated with biomarker, geochemical, and clay mineralogical data to test the hypothesis regarding the origin of CRM in relation to smectite illization. These data further address the causes and timing of diagenesis and thermal maturation of Mesozoic rocks in the Disturbed Belt.

MATERIALS AND METHODS

Samples were collected from Subbelts I and II of the Disturbed Belt in Montana, which consists of Mesozoic strata that were deformed during the Laramide Orogeny (Mudge, 1982). Most samples were collected from the calcareous Cone Member of the Marias River Shale, which contains dark gray shale, limestone concretions, thin beds of limestone, and bentonites (Cobban *et al*., 1959). The Cone Member was probably a hydrocarbon source rock in the Disturbed Belt and is a known reservoir rock for crude oil and natural gas in the Sweetgrass Arch (Clayton *et al*., 1982). Samples were also collected from horizontal beds of the Vaughn Member of the Blackleaf Formation shale at the Sweetgrass Arch (Vaughn, Montana), and from a nearly overturned section of the Jurassic Ellis Formation at Swift Dam (Figure 1).

Concretions, bentonites, and carbonaceous shales were sampled at two outcrops (Badger Creek and Pishkun Canal) of the Marias River Shale and at one outcrop of the Blackleaf Formation at Vaughn (Figure 1). Results of studies of some of the collected samples, specifically K-Ar and clay mineral data from the Pishkun Canal bentonites and paleomagnetic data from one Pishkun Canal site and two Badger Creek sites, were published in a short, conference-related report (Elliott *et al*., 2006b). Limestone concretions are aligned with the direction of bedding and are from a few centimeters to ~30 cm in diameter. The bedding of the shale dips 75ºE at Pishkun Canal and from 20ºSW to 30ºSW at Badger Creek. Thick (>5 cm) bentonites were collected at both Badger Creek and Pishkun Canal. Thin

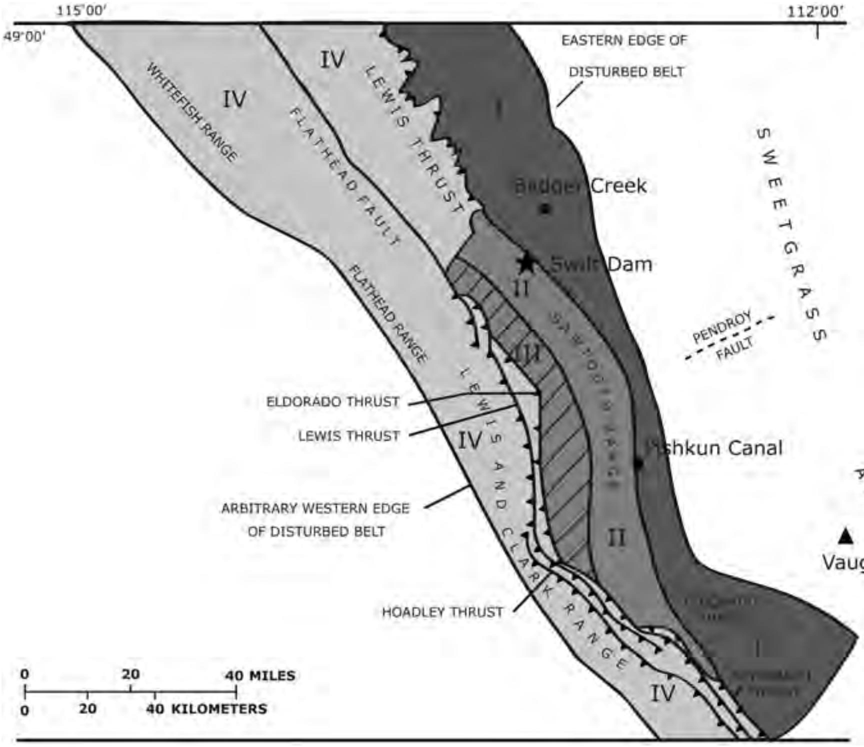

Figure 1. Map of the study area in Montana and sampling locations: Badger Creek (square), Swift Dam (star), Pishkun Canal (circle), and Vaughn (triangle). Areas I–IV refer to subbelts of the Disturbed Belt (modified from Mudge, 1982).

bentonites (1–2 cm) were also collected at Badger Creek. A thick bentonite from the Ellis Formation was sampled at Swift Dam. Locations (latitude, longitude) for the Badger Creek, Pishkun Canal, and Swift Dam outcrops were given by Osborn (2006).

Portions (~25 g) of the collected bentonite samples were treated, using the methods of Jackson (1979), to remove carbonate cements, bulk organic matter, and Fe oxide cements. The treated portions were separated into sand, silt, and clay fractions by timed settling. The clay fractions were separated into sub-micrometer size fractions by centrifugation. The mineralogy of the clay fractions, the percentage of illite layers in I-S, and the stacking order of I-S were determined by X-ray diffractometry (XRD) of oriented clay following methods of Hower (1981) and Moore and Reynolds (1997). The K-Ar age values of clay fractions and clay sub-fractions were determined by procedures detailed by Osborn (2006). The LP-6 Bio interlaboratory standard was analyzed for potassium and radiogenic argon five times (Table 1). These results agree with accepted values (Odin *et al*., 1982).

Cores (2.5 cm diameter) were drilled from the limestone concretions and oriented with an inclinometer and a Brunton Compass. The cores were cut into standard specimens (2.2 cm long). Natural remanent magnetization (NRM) was measured with a 2G Enterprises cryogenic magnetometer with DC squids at the Paleomagnetic Laboratory of The University of Oklahoma. Most samples were processed through 19 steps of thermal demagnetization by heating in an SC Thermal Demagnetizer for 1 h. Selected samples were treated by alternating field demagnetization to 120 mT before undergoing thermal demagnetization. The demagnetization data were displayed on orthogonal projections (Zijderveld, 1967) and the components of the magnetization were determined by principal component analysis (Kirschvink, 1980) with mean angular deviations of 10º or less. The intensity of characteristic remanent magnetization (ChRM) for each specimen was calculated and mean site intensities were determined. Mean directions were calculated with Fisher (1953) statistics. Isothermal remanent magnetization (IRM) acquisition and thermal decay measurements were also performed to identify the magnetic minerals (Lowrie, 1990). A tilt test was performed on the results from Badger Creek and Pishkun Canal. The ChRM directions from beds tilted by different amounts are compared after incremental rotations that produce the same degree of relative ‘untilting’ of each bed. The incremental rotations range from zero for *in situ* bed orientation to 100% for the original horizontal bed orientation. If the best grouping of ChRM directions is for zero rotation, then the magnetization is considered post-tilting. If the best grouping is after rotation to the horizontal, the magnetization is considered pre-tilting. Otherwise the magnetization is considered syn-tilting.

Hand samples of carbonaceous shales were collected for organic geochemical analyses. Weathered surfaces were removed with a Dremel drill, and each sample was broken into smaller pieces, which were then ground to fine powder with a mortar and pestle. Organic matter was extracted from the powders in a Soxhlet apparatus with a mixture of dichloromethane and methanol. Most of the solvent was removed by evaporation under a stream of N_2 gas and hexane was added to each extract. The solutions then sat overnight at room temperature so the asphaltene fractions would precipitate. After removal of the asphaltene fractions by centrifugation, the remaining hexane-soluble components were separated into their respective saturated, aromatic, and heteroatomic compound (those containing N, S, or O) fractions by column chromatography. Details of the method were reported by Totten (2005). The procedure of West *et al*. (1990) was used to isolate the branched and cyclic alkanes from a portion of each saturated fraction. The methods reported by Totten (2005) were used to analyze the saturated fractions by gas chromatography and their sub-fractions of branched and cyclic alkanes by gas chromatography-mass spectrometry. The terpanes used to calculate thermal maturity ratios (Ts/Tm; Seifert and Moldowan, 1986) were as follows: 18α-30-norneohopane (C29Ts); 17α-30-norneohopane (C29Tm); 18α,21β-22,29,30-trisnorhopane (C27Ts); and 17α,21β-22,29,30-trisnorhopane (C27Tm). $T_{\max}$ values determined from Rock-Eval pyrolysis were used to calculate vitrinite reflectance values for the samples (Totten, 2005).

Strontium isotope analysis was done at the University of Texas-Austin according to the methods described by Gao *et al*. (1992). After fractionation corrections to $^{86}Sr/^{88}Sr = 0.1194$, the $^{87}Sr/^{86}Sr$ ratios were normalized relative to a mean observed value of 0.71014 for the ratio in SRM 987 (National Institute of Standards and Technology).

RESULTS

Clay mineralogy and K-Ar dating of I-S

The clay mineralogy and the K-Ar age values of the clay sub-fractions from seven samples, and of the clay fraction of four of those samples, were determined (Table 1). At Badger Creek, several bentonites of variable thickness were sampled. Samples BC-03, BC-05, and BC-06 are from thin (1–2 cm) bentonites. BC-01 is from a thick (>5 cm) bentonite. The rectorite-like ordering (R1) was found in I-S from both Pishkun Canal and Badger Creek (BC-01 and BC-06), as indicated by a superlattice peak at 26–28 Å in diffraction patterns of air-dried clay. On glycol saturation of the clay, this peak shifted to 29–30 Å. The percentage of illite layers in I-S is between 60 and 70% in the thick bentonite BC-01 and also in a thin bentonite (BC-06). Greater percentages of illite layers in I-S (>90%) and higher ordering (R3) were found in other

Table 1. Bentonite clay mineralogy and K-Ar data.

Location, Sample	Clay mineralogy	K (% by mass)	^{40}Ar* (%)	^{40}Ar* (pmol g^{-1})	K-Ar age (Ma)
Badger Creek					
BC-01 (<0.25 µm)	I-S (60−70% I), kt	3.68±0.04	87	367±6	56.6±1.0
BC-01 (0.25−1.0 µm)	I-S (60−70% I), kt	3.71±0.04	89	375±4	57.4±0.9
BC-01 (0.25−1.0 µm)a		3.82±0.04	89	378±4	56.2±0.8
BC-01 (1−2 µm)	I-S (60−70% I), kt	3.75±0.04	88	368±4	55.8±0.8
BC-01 (1−2 µm)a		3.64±0.04	88	365±4	56.9±0.9
BC-03 (<0.25µm)	I-S (>90% I), kt	3.01±0.05	78	658±8	121.9±2.3
BC-03 (<0.25 µm)a		2.97±0.06	74	662±8	124.1±2.9
BC-03 (0.25−1.0 µm)	I-S (>90% I), kt	3.09±0.03	94	1008±11	178.9±2.6
BC-03 (0.25−1.0 µm)a		3.08±0.03	95	1004±11	179.1±2.6
BC-03 (1−2 µm)	I-S (>90% I), kt	2.47±0.03	95	1046±12	228.6±3.9
BC-03 (1−2 µm)a		2.42±0.02	95	1042±12	232.5±3.3
BC-03 (< 2 µm)	I-S (>90% I), kt	3.18±0.07	89	851±12	148.2±3.7
BC-05 (<0.25 µm	I-S (>90% I), kt	3.78±0.04	94	883±10	129.8±1.9
BC-05 (0.25−1.0 µm)	I-S (>90% I), kt	3.24±0.03	95	1193±14	200.9±2.9
BC-05 (1−2 µm)	I-S (>90% I), kt	3.34±0.03	95	1107±13	181.9±2.6
BC-06 (<0.25 µm)	I-S (70−80% I), kt	3.34 ±0.03	85	354±4	60.2±0.9
BC-06 (0.25−1.0 µm)	I-S (70−80% I), kt	3.09 ±0.03	87	340±5	62.3±1.1
BC-06 (1.0−2.0 µm)	I-S (60−70% I), kt	2.80 ±0.03	89	343±5	69.3±1.2
Pishkun Canal					
SR-04 (<0.25 µm)	I-S (70−80% I)	4.14±0.08	81	389±5	53.3±0.8
SR-04 (0.25−1.0 µm)	I-S (70−80% I), kt	4.15±0.08	92	390±4	53.3±1.1
SR-04 (1.0−2.0 µm)	I-S (70−80% I), kt	4.14±0.07	88	395±5	54.1±1.1
SR-04 (<2 µm)	I-S (70−80% I), kt	3.98±0.11	84	363±5	51.9±1.6
Swift Dam					
SD-03 (<0.25 µm)	I-S (70−80% I), kt	4.47±0.05	88	436±5	55.3±0.8
SD-03 (0.25−1.0 µm)	I-S (80−90% I), kt	3.65±0.04	88	362±6	56.2±1.0
SD-03 (1.0−2.0 µm)	I-S (80−90% I), kt	3.37±0.03	86	330±4	55.7±0.8
Vaughn					
VQ (<0.25 µm)	I-S (20−30% I)	0.89±0.02	60	79±1	50.6±1.2
VQ (0.25−1.0 µm)	I-S (20−30% I), kt	0.95±0.01	66	86±1	51.7±0.8
VQ (1.0−2.0 µm)	I-S (20−30% I), kt	1.04±0.01	65	95±1	51.8±0.9
VQ (<2 µm)	I-S (10−20% I), kt	1.18±0.02	54	100 ±2	48.3±1.2
LP6 (Biotite interlaboratory standard)					
		8.12±0.12	96	1943±30	132.9±2.7
		8.34±0.08	97	1935±22	129.1±1.9
		8.25±0.08	97	1921±22	129.4±1.9
		8.37±0.09	97	1918±22	127.5±1.9
		8.23±0.08	97	1943±22	131.2±1.9
Accepted (Odin *et al.*, 1982)		8.33±0.03		1930	127.7±1.4

Notes: An ‘a’ after the size fraction denotes duplicate K-Ar determination.
Kaolinite is abbreviated to kt. ^{40}Ar* stands for radiogenic Ar. The error values are twice the estimated standard deviation (2σ) owing to random error. Pishkun Canal data from Elliott *et al.* (2006b).

thin bentonites (BC-03 and BC-05). Representative diffraction patterns of the glycol-solvated <0.25 µm clay fractions from thick bentonites (BC-01, Pishkun Canal, and Swift Dam) and from a thin bentonite at Vaughn are shown in Figure 2.

K-Ar age values were concordant at ~56−57 Ma for the clay sub-fractions of the thick bentonite (BC-01) but not for those of the thin bentonites at Badger Creek. The criterion for concordance used herein is that age values differ by no more than the sum of their error values (the 2σ error estimates). If the age values of the three sub-fractions are weighted equally, then the mean age value for BC-01 I-S is 56.6 Ma and the sample standard deviation is 0.23 Ma. The mean age value with 2σ

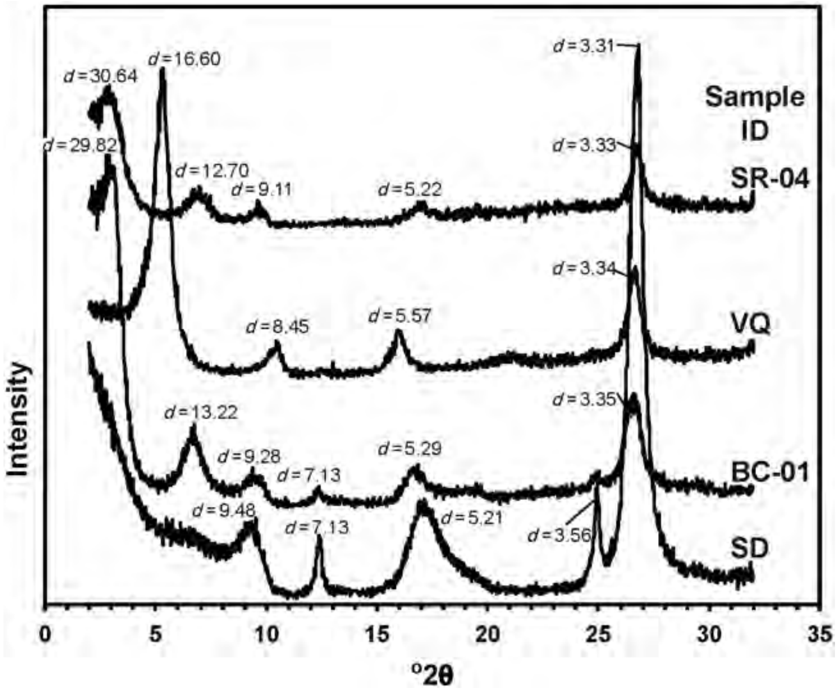

Figure 2. XRD patterns of the <0.25 μm fractions, glycol-solvated, of bentonites collected at Badger Creek (BC-01), Pishkun Canal (SR), Swift Dam (SD), and Vaughn (VQ). The *d* values are given in angstroms.

uncertainty is then 56.6 ± 0.5 Ma. For the BC-06 bentonite, the age values ranged from 60 to 69 Ma, but those of the two finer sub-fractions were concordant at 60−61 Ma.

Concordant K-Ar age values with a mean of 53.6 ± 0.9 Ma were determined for the clay sub-fractions of the bentonite from Pishkun Canal. This bentonite has more illite layers in I-S (70−80%) than the thick bentonite at Badger Creek (BC-01). I-S from the thick bentonite at Swift Dam has R3 stacking order and, in the two coarser clay sub-fractions, greater percentages of illite layers (>80%) than the Pishkun Canal bentonite. The K-Ar age values of clay sub-fractions of the Swift Dam bentonite were concordant with a mean of 55.7 ± 0.9 Ma. The percentage of illite layers in I-S from the bentonite sample collected near Vaughn is ~20% and the K-Ar ages of the clay sub-fractions were concordant with a mean of 51.4 ± 1.3 Ma.

Organic geochemical indicators of thermal maturity

The $T_{\max}$ values in the shale samples ranged from 431ºC to 457ºC (Table 2). The values were lower for shale from Badger Creek (431ºC and 433ºC) and Vaughn (437−439ºC) than for shale from Pishkun Canal (440−453ºC) and from the Ellis Formation at Swift Dam (445ºC and 452ºC). Values for vitrinite reflectance (R_o) calculated from the $T_{\max}$ values range from 0.6 at Badger Creek to near 1.0 at Pishkun Canal and Swift Dam (Table 2). The values for Vaughn were uncertain because of uncertainties in measuring the S2 peaks (Totten, 2005). The Badger Creek R_o values signify source rocks immature with respect to oil generation. The higher R_o values at Swift Dam and at Pishkun Canal signify thermal maturity within the oil-generating zone.

The ratios of selected biomarkers (C27 Ts/Tm, C29 Ts/Tm) were small for samples from Badger Creek and Vaughn. These ratios were much greater for samples from Swift Dam and Pishkun Canal (Figure 3, Table 2). These biomarker data are consistent with the $T_{\max}$ values observed for the shale samples at these localities.

Sr isotope ratios

The $^{87}Sr/^{86}Sr$ ratio observed for the concretion at Vaughn (0.7073) coincides with a coeval seawater value (0.7073−0.7074; McArthur *et al.*, 2001; Mearon *et al.*, 2003). The concretions at Badger Creek (0.7077) and Pishkin Canal (0.7081) had elevated values, greater than the coeval seawater value between 0.7073 and 0.7074.

Paleomagnetism

The measured NRM intensity in limestone concretions from the Marias River Shale ranged from 0.025 mA/m (Badger Creek) to 0.142 mA/m (Pishkun Canal). The magnetic intensities measured at Pishkun Canal were variable (0.074, 0.091, and 0.142 mA/m). The magnetic intensity found in a concretion from the Ellis Group at Swift Dam was 0.088 mA/m, and that found in two concretions from the Blackleaf Formation at Vaughan was 1.01 mA/m.

The demagnetization results revealed two components of the NRM, a viscous remanent magnetism (VRM) and a ChRM. At low temperatures (<~200ºC),

Table 2. Biomarker, T_{max}, and NRM intensity data.

Location/ Sample	Ts/Tm C27	Ts/Tm C 29	CR	T_{max} (ºC)	R_o	NRM (mA/m)
Badger Creek Concretion						0.025
04BC2	0.28	0.29	1.04	431	0.60	
04BC3	0.35	0.28	0.80	433	0.63	
Pishkun Canal Concretions						0.074, 0.091, 0.142
D11	4.45	1.18	0.27	450*	0.94*	
D10	4.21	1.26	0.30	453	0.99	
04 SR 6	5.78	1.44	0.25	452*	0.98*	
04 SR 5	7.11	1.75	0.25	440	0.76	
Swift Dam Concretion						0.088
04 SD 10	9.13	1.59	0.17	445*	0.85*	
04 SD 9A	5.44	0.76	0.14	452	0.98	
04 SD 9B	4.74	0.81	0.17	457*	1.07*	
Vaughn Concretions						0.101
04 VQ	0.27	0.26	0.96	439*	0.74*	
04 VQ 2	0.32	0.32	1.00	437*	0.71*	

Notes: CR = ratio of C29/C27. NRM = natural remanent magnetism. *The T_{max} and R_o derived from T_{max} should be viewed as estimated or approximate values based on S2 peak measurements (Totten, 2005; M. Engel, pers. comm.).

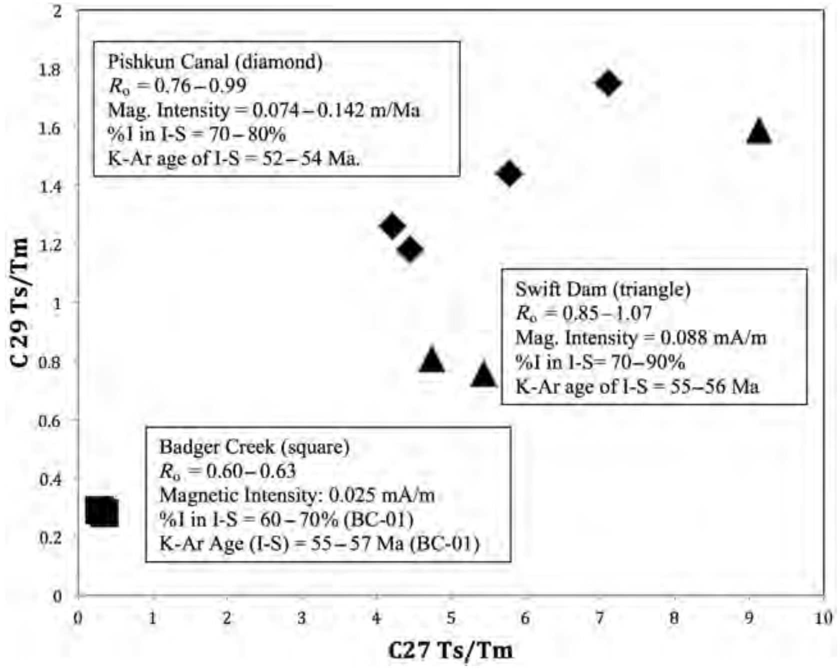

Figure 3. Plot of selected biomarker ratios (C27 Ts/Tm, C29 Ts/Tm) from Badger Creek (squares), Pishkun Canal (diamonds), and Swift Dam (triangles) from Totten (2005). NRM intensity, R_o, derived from T_{max} data, percentage of illite layers in I-S from thick bentonites, and range of concordant K-Ar age values are noted for each site.

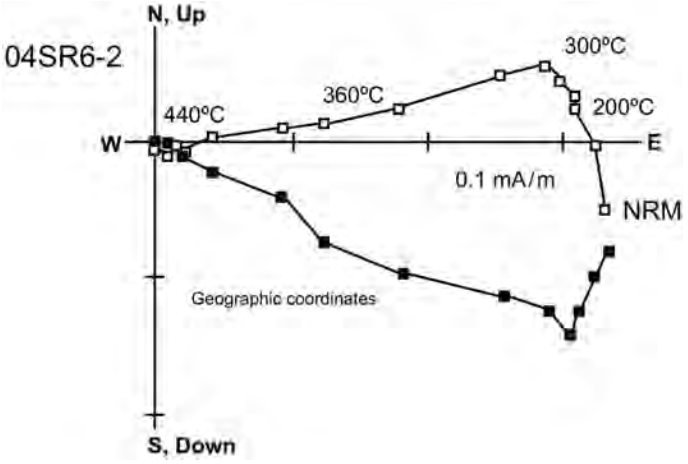

Figure 4. Representative Zijderveld diagram showing removal by thermal demagnetization of a modern VRM below 200ºC and of the ChRM between 200 and 440ºC. Open symbols: vertical component; closed symbols: horizontal component.

a northward and steeply downward component, interpreted to be a modern VRM, was removed from all concretion specimens. The ChRM from three Badger Creek limestone concretions and three Pishkun Canal limestone concretions, was removed between 200ºC and 440ºC (Figure 4). In geographic coordinates, the ChRM at the Pishkun Canal had east-southeasterly declinations and shallow inclinations whereas at Badger Creek the ChRM had southwesterly declinations and steeply upward inclinations (Figure 5; Table 3). The ChRMs were also removed by alternating field demagnetization from the Badger Creek and Pishkun canal specimens, which suggests the magnetization resided in a low-coercivity mineral such as magnetite or pyrrhotite. Most specimens from the concretions on the Sweetgrass Arch did not display stable decay. A few contained the modern VRM but did not display linear decay at unblocking temperatures above 250ºC.

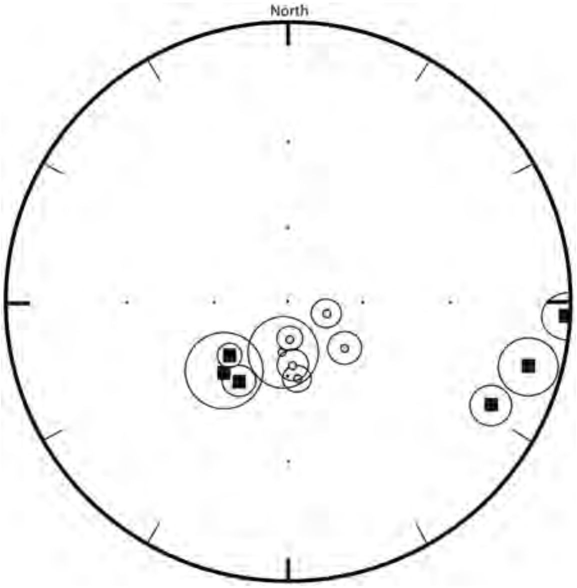

Figure 5. Equal area plot showing site mean directions with α95 circles in geographic (squares) and 100% tilt-corrected (small circles) coordinates. The best grouping is in tilt-corrected coordinates, which indicates magnetization before significant tilting occurred.

Assuming the ChRMs at Badger Creek and Pishkun Canal were contemporaneous, the mean site directions were used for a regional tilt test. Two results from two concretion sites at Pishkun Canal reported by Gill *et al.* (2002) were used in the tilt test. The site mean directions grouped best after correction for the tilt of the beds (100% untilting, declination = 160.2º, inclination = −69.1º, *k* [precision parameter] = 38.1, α95 [cone of 95% confidence] = 11.0º, *n* = 6; Figure 5). The Enkin (2003) tilt test indicates that the best grouping occurs at untilting of 114 ± 25%. The 95% confidence interval overlaps the 100% tilt correction and the ChRM could be interpreted as a pre-tilting magnetization. The 95% confidence interval is large, however, and the ChRM could also have been early syn-tilting.

The pole position for the 100% tilt-corrected direction is 185ºE, 77ºN (dp/dm [semi axes of 95% oval of confidence] = 15.9º/18.7º). This pole plots near the Paleogene part of the apparent polar wander path (Torsvik *et al.*, 2012). The directions for the ChRM were all reversed, which suggests that the ChRM is secondary, because the Marias River Shale was deposited during the Cretaceous Normal Polarity Superchron.

Magnetic intensity rose rapidly during IRM-acquisition studies of samples from Pishkun Canal (Gill *et al.*, 2002) and from Badger Creek (this study). Saturation was reached by 200−300 mT, suggesting that a low-coercivity phase dominates the magnetization. Thermal decay measurements of a triaxial IRM showed complete removal by 580ºC, indicating the presence of magnetite (Lowrie, 1990). A decrease in intensity of the low- and intermediate-coercivity components in the 300−320ºC

Table 3. Site mean paleomagnetic data for carbonate concretions.

Locality	Site #	N/No	– *In situ* – Dec (º)	Inc (º)	*k*	α95(º)	Tilt-corrected Dec (º)	Inc (º)
Badger Creek	04BC2**	4/4	222.8	−52.7	44.6	13.9	186.4	−69.3
Badger Creek	04BC3**	8/9	212.1	−51.3	87.1	6.0	176.3	−63.9
Badger Creek	05BC4	9/9	227.4	−58.4	110.4	4.9	178.7	−74.9
Pishkun Canal	04SR6**	8/8	117.4	−11.7	131	4.9	173.4	−58.8
Pishkun Canal	D10*	6/7	105.4	6.7	100.1	6.7	129.1	−60.7
Pishkun Canal	D11*	9/9	92.9	0.4	108.8	5.0	108.7	−73.3

Notes: N/N_o – Number of specimens with direction *vs.* number of specimens demagnetized;
In situ – Geographic coordinate direction; Tilted – Stratigraphic coordinates; Dec – Declination;
Inc – Inclination; *k* – Precision parameter; α95 – Cone of 95% confidence.
* denotes data from Gill *et al.* (2002); ** denotes data published by Elliott *et al.* (2006b).

range also suggests the presence of pyrrhotite. These results suggest the ChRM in Disturbed Belt concretions found by stepwise demagnetization resides predominantly in magnetite. In contrast, the IRM-acquisition measurements of concretions from Vaughn showed an increase in intensity by 200 mT followed by a more gradual increase. These data suggest the presence of both lower- and higher-coercivity phases. Thermal-decay measurements showed removal of the low- and intermediate-coercivity curves by 580ºC. The high-coercivity curve was removed by 650–680ºC suggesting the presence of hematite.

INTERPRETATION AND DISCUSSION

Indicators of thermal maturity

The new clay-mineralogical results presented here are consistent with earlier work by Hoffman and Hower (1979) in that the I-S in bentonite samples from the Montana Disturbed Belt was ordered and illite-rich, while that in rocks on the Sweetgrass Arch I-S was randomly stacked and smectite-rich. The stacking order and percentage of illite layers in I-S suggest burial temperatures in the range 100–200ºC (Hoffman and Hower, 1979) for the Cretaceous rocks at Pishkun Canal and Badger Creek and for the Jurassic Ellis Formation from the same zone of the Disturbed Belt. Thus, the clay mineralogy indicates that these rocks were within the oil-generation window (Pevear, 1999). The new results are consistent with the previous interpretation that diagenetic illite formed in response to increased temperature due to thrust-sheet burial (Hoffman *et al.*, 1976). The data from the present study indicate that the degree of smectite illitization in bentonite presently exposed in Subbelts I and II is variable. At the Badger Creek sampling site, farther north than the other Disturbed Belt sites and farther from the mountain front where the rocks were more intensely deformed, the percentage of illite layers found in I-S was 60–70%, less than at the other sites. The randomly ordered, smectite-rich I-S in bentonite from Vaughn denotes a much less thermally mature rock on the Sweetgrass Arch.

In addition to the evidence for clay diagenesis, the present study provides information from other indicators of thermal maturity. The Rock-Eval and biomarker results, including the calculated R_o values, indicate low thermal maturity of shale at the Badger Creek site and moderate thermal maturity at the two other Disturbed Belt sites. A difference of ~10% illite layers in I-S of bentonite coincides with a significant difference in thermal maturity of shale indicated by the Rock-Eval and biomarker data. The thermal maturity of Marias River Shale indicated by ratios of terpane compounds (Ts/Tm; Figure 3) is correlated with both percentage of illite layers in I-S and calculated vitrinite reflectance. In summary, a variety of indications of more active diagenesis correspond to increasing proximity to the mountain front and, thus, to increasing intensity of deformation in the Disturbed Belt.

K-Ar age values

The K-Ar age values for I-S from the thicker bentonites were <60 Ma and concordant across each set of clay sub-fractions. The larger and more variable age values for the clay sub-fractions of BC-06, from a thin Badger Creek bentonite, were probably due to small amounts of detrital illite – more in the coarse fraction than in finer ones – from shale originally entrained in the bentonite or included during collection of the bentonite. The predominance of detrital illite was indicated by much greater age values for BC-03 and BC-05 and also by >90% illite in the I-S.

The high degree of concordance of age values across the range of clay-particle size for each of the four thicker bentonites has several important implications. First, the concordance rules out a significant contribution of radiogenic argon by volcanogenic feldspar or mica (as well as by detrital minerals, already effectively ruled out by the thickness of the bentonite), because such minerals should be much older than the diagenetic I-S and relatively most abundant in the coarsest clay fraction. Second, the concordance rules out significant loss of radiogenic argon by thermal diffusion (proposed as significant under certain conditions by Clauer and Lerman, 2012), because such loss should have affected the finest I-S more than the coarser fractions. Third, the concordance indicates that the illite layers in I-S within each of the thicker illite-rich bentonites grew within a short time period, because thicker fundamental particles of illite are expected to be significantly younger than the thinnest ones if illitization occurred over an extended time period (Środoń *et al.*, 2002). This inference does not apply to the poorly illitized bentonite from near Vaughn, because its illite fundamental particles, few in number relative to a larger number of smectite fundamental particles, should all be thin. This hypothesis can be tested through measuring particle-size distributions of the illitic clay fractions (Eberl *et al.*, 2011). Fourth, the concordance permits the time of illite formation within each sample to be better defined than it could be from a single K-Ar age determination, because concordant age values may be averaged with confidence to provide a mean age having less uncertainty than a single age value.

The age values of I-S from the thicker (>5 cm) bentonites (means of the concordant values from different clay sub-fractions) in the Disturbed Belt decrease southward, from 56.6 ± 0.5 Ma at Badger Creek, to 55.7 ± 0.9 Ma at Swift Dam, and to 53.6 ± 0.9 Ma at Pishkun Canal. The concordant age values for SR-04 at Pishkun Canal agree well with K-Ar age values of ~53−54 Ma reported by Altaner *et al.* (1984) for <1 μm size fractions of three samples of a 2.5 m thick bentonite in the Marias River Shale in the Sun River Canyon nearby. K-Ar data for clay fractions of two other bentonite samples from the Marias River Shale in the Sun River Canyon were also published by Hoffman *et al.* (1976); K-Ar age values for those two samples calculated from their radiogenic Ar and K_2O contents (with no adjustment for labile K) with the decay constants and isotopic abundances in current use (Steiger and Jäger, 1977) would be 51.4 Ma and 52.1 Ma (J.L. Aronson, pers. comm.). Thus, substantial evidence exists in support of illitization of smectite early in the Eocene Epoch in bentonites now exposed in the Sun River Valley. This illitization was notably later than the cessation of thrusting in the Disturbed Belt at ~59 Ma as inferred by Sears (2001). The data from the present study show a north-to-south progression of the effects of this thrusting. In particular, the similarity of K-Ar values of I-S from Jurassic and Cretaceous rocks supports a thrust-burial model for illitization.

The Pishkun Canal site is closer to the front ranges than the Badger Creek site. The rocks at Pishkun Canal are more strongly deformed. These rocks might have experienced deeper burial for a longer period of time as a result of thrust loading. Such prolonged thrust loading could have produced the younger illite at Pishkun Canal. If this interpretation is correct, then the timing of I-S formation may be explained by a dissolution-precipitation model (Altaner and Ylagan, 1997) in which radiogenic argon was released from older diagenetic illite as new and younger diagenetic illite was formed.

An alternative explanation of the younger illite at Piskun Canal might be found by seeking a mechanism for brief but later heating at Pishkun Canal than at Badger Creek and Swift Dam. The temporal temperature increase in footwall rock of major overthrusts in the Disturbed Belt was modeled by Hoffman and Hower (1979) who inferred that rocks within 200−300 m of a thick (6 or 7 km) overthrust sheet would have reached 'metamorphic temperatures' (>100ºC) soon (<1 m.y.) after the sheet was emplaced, owing to heat conduction downward. Those authors also inferred that under a thin overthrust sheet (~4 km), ~10 m.y. might be required for temperature to reach 100ºC, not from heat conducted downward but in response to restoration of a normal geothermal gradient in the rocks that had been buried by thrusting. From the then-available knowledge of thrust-sheet thicknesses, Hoffman and Hower (1979) inferred that rocks now exposed in the Sun River Canyon would have experienced the slower heating.

With respect to the differences in K-Ar age values, the thermal model of Hoffman and Hower (1979) offers an explanation − a slower heating in response to overthrusting − for the younger illite at Pishkun Canal than at Badger Creek and Swift Dam. That explanation, however, cannot account for the greater thermal maturity of the rocks at Pishkun Canal than at Badger Creek, evident from several indicators of thermal maturity applied in the present study. Furthermore, because Hoffman and Hower (1979) did not consider how denudation would have affected burial depth after emplacement of the thrust sheets, their model of slow heating of rock under thinner thrust sheets cannot account for the brief illitization implied by concordance of age values across the clay sub-fractions.

A detailed picture of the emplacement of a very thick thrust slab in the Montana Disturbed Belt during the Laramide Orogeny, including a description of the effects of the emplacement on the overridden footwall rocks was presented by Sears (2001). This picture included modeling of burial history in response to both the overthrusting and the subsequent rapid denudation (Sears, 2001, Figure 4). For rocks along the present-day mountain front, the model suggests rapid burial over 10−15 m.y. followed by somewhat more rapid exhumation over ~10 m.y. The model also implies that the maximum depth of thrust-slab burial (Sears, 2001, Figure 2), and consequently the rates of burial and subsequent exhumation, decreased rapidly toward the northeastern edge of the Disturbed Belt. The model of Sears (2001) provides a possible explanation for the strong but brief heating needed to account for a high degree of illitization in a short time period at Pishkun Canal and Swift Dam. For rock that had been more than ~⅓ km below the overriding slab, conductive heating after thrust-slab burial would have been due primarily to heat coming from hotter rock below, and the maximum temperature would have been reached substantially after deepest burial had occurred. That maximum temperature, the time elapsed before it was reached, and its effective duration would have depended on the initial temperature of the buried rock, on the maximum depth, and on the rates of burial and exhumation. Before deformation began, the Jurassic rock in the sedimentary column should have been warmer than the overlying Cretaceous rock; the difference in initial temperature perhaps accounts for the earlier illitization in the Jurassic bentonite at Swift Dam than in the Cretaceous rock to the south. The Sears (2001) model also suggests that the presently exposed rocks that are farther from the mountain front (Badger Creek) should have been closer to the overthrust slab, where they might have been heated promptly and briefly by heat moving downward from the thrust slab, but not as strongly over time as the then more deeply buried rocks now near the mountain front. If this idea is correct, then the K-Ar data indicate that thrust slab emplacement over what is now the Badger Creek area occurred at ~57 Ma. Such timing is not inconsistent with the inference of Sears (2001) that thrusting ended at ~59 Ma, because there could have been some systematic error in the K-Ar age values.

Fluids, either internal or externally derived, might also have influenced the timing and degree of illitization. Sears (2001) noted evidence that no metamorphic fluids were released from the overthrust slab, but he also described evidence for release of hot fluids from the more deeply buried footwall rocks and noted some likely effects of such fluids on rocks farther to the east. Insofar as release of fluids from deeply buried footwall rocks would have been driven by the immediate effect of increased pressure, rather than by the delayed effect of increased temperature, the effects of such fluids should have been manifest during the orogeny rather than after it ended. Such fluids moving eastward could have warmed sedimentary rocks above their initial temperature, however, thus influencing indirectly the timing of later illitization as well as causing geochemical changes in the rock. The results of the present study indicate that at least the concretions were altered by fluids with elevated ^{87}Sr/^{86}Sr ratios. This could mean that externally derived fluids altered the rocks. The dissolution of K-feldspar in shale by internal fluids generated by smectite illitization might also account for the elevated ^{87}Sr/^{86}Sr ratios.

In summary, concordant age values across clay subfractions of Disturbed Belt bentonites indicate that brief illitization occurred at about the time when thrusting ceased toward the north (Badger Creek and Swift Dam) and a few million years later toward the south (Sun River area). Post-thrusting heating of the overridden sedimentary rock owing to conductive heating could account for both the degree and timing of illitization, but this idea must remain hypothetical until much more relevant information is obtained. At this time, an effect of moving orogenic fluids on illitization of the bentonites remains a possibility.

Paleomagnetism

The burial temperatures in the Cretaceous rocks in the Disturbed Belt ranged from 100 to 200ºC according to estimates by Hoffman and Hower (1979). The calculated R_o values range from 0.60−0.63 at Badger Creek to 0.76−0.99 at Pishkun Canal. The maximum burial temperature was probably near 100ºC at Badger Creek but may have approached 200ºC at Pishkun Canal. If the maximum temperature was near 200ºC, the maximum unblocking temperature (440ºC) would have been too high for the ChRM to be a thermoviscous remanent magnetization (TVRM) caused by burial heating according to the time-temperature relationships of Pullaiah *et al.* (1975). The 200ºC estimate and the maximum unblocking temperatures, however, are consistent with a TVRM that resides partially in multidomain magnetite, based on other studies (*e.g.* Middleton and Schmidt, 1982; Kent, 1985). A maximum burial temperature of 100ºC, however, is probably too low for the ChRM to be thermoviscous in origin. Because the ChRM is present at Badger Creek, where burial temperatures were lower (maximum ~100ºC), the ChRM is interpreted as a CRM.

The presence of the CRM in the Disturbed Belt and its absence to the east suggests a genetic relation between the CRM and deformation of the Cretaceous rocks. The age based on pole position is not constrained well enough to make a precise comparison with the K-Ar illite ages. An early syn-tilting or pre-tilting CRM is not consistent with a connection between thrust loading and illitization, particularly considering the interpretation above that illitization at the Pishkun Canal site occurred several million years after cessation of thrusting. A pre-tilting CRM is problematic for a connection between thrust loading and the CRM. Pre-deformational burial depths for the Cretaceous rocks (<1 km) were too small to have caused illitization (*e.g.* Katz *et al.*, 2000) or maturation of organic matter (*e.g.* Banerjee *et al.*, 1997; Blumstein *et al.*, 2004) by burial alone. Several models for the origin of the CRM may be considered, including the migration of externally derived orogenic fluids (Oliver, 1992; Sears, 2001). One scenario is that the alteration could have been triggered by fluids that migrated in front of or were triggered to migrate by the deformation front to the west (*e.g.* Enkin *et al.*, 2000; O'Brien *et al.*, 2007). This scenario would be consistent with pre-tilting or syn-tilting CRM. The Sr isotope results, however, do not provide convincing evidence for alteration by external fluids because dissolution of K-feldspar in shale by internal fluids from smectite illitization could have generated the elevated $^{87}Sr/^{86}Sr$ ratios. The origin of the CRM in the concretions is unresolved, although it does provide evidence for a diagenetic event that caused acquisition of the CRM and precipitation of authigenic magnetite prior to or during early deformation.

The CRM reported in this study is similar to magnetizations from Paleozoic rocks in the southern Canadian Cordillera reported by Enkin *et al*. (2000) who noted a pre-folding Cretaceous CRM in magnetite, which was older in the west and younger in the east. Those authors proposed that the CRM was caused by alteration associated with a diagenetic front that moved eastward ahead of the deformation. They also reported the presence of a younger syn-tilting to post-tilting thermoviscous remagnetization in magnetite. A pre-tilting to early syn-tilting Early Cretaceous CRM in magnetite within folded Mississippian carbonate rocks in the southern Canadian Cordillera was reported by Zechmeister *et al*. (2102). Geochemical data and a vein-contact test suggested that the CRM was associated with fluids that migrated in front of the deformation front. They also reported an intermediate-temperature late syn-tilting to post-tilting CRM residing in pyrrhotite, which they attributed to thermal sulfate reduction.

SUMMARY

The clay mineralogy and the organic geochemistry data together provided a consistent view of the extent of thermal maturation as seen from the study of samples from three localities (Pishkun Canal, Badger Creek, and the Sweetgrass Arch). The concordant K-Ar data from the thick bentonites indicated that illite grew in a short time, perhaps *via* a dissolution-precipitation process. The K-Ar ages suggested some necessary revision of earlier ideas of how thrust burial prompted the formation of diagenetic illite in these bentonites. The thicknesses of bentonites were important for measuring concordant ages among these sub-fractions. The clay-mineral data (stacking order and percentage of illite layers) together with organic geochemistry data were consistent with the apparent extent of burial and deformation caused by thrust-sheet burial. The Sr geochemical data suggested that internal or externally derived fluids might have influenced illitization. Large percentages of illite layers were found with evolved organic matter, as indicated by calculated vitrinite reflectance values derived from $T_{\max}$ data and biomarker ratios, at Pishkun Canal (overturned beds). Smaller percentages of illite in I-S and less evolved organic matter were seen in moderately deformed strata at Badger Creek.

Although a broad genetic relationship is present among a CRM, thermal maturation, formation of diagenetic illite, and deformation in this study area, the K-Ar results of the present study did not support the hypothesis that acquisition of the CRM was caused by illitization. The paleomagnetic data provided evidence for a diagenetic event of unspecified origin prior to illitization that caused acquisition of a CRM residing in magnetite.

ACKNOWLEDGMENTS

This study comprised the Masters degree theses of Louise Totten at the University of Oklahoma and of Stephen G. Osborn at Georgia State University. The US Department of Energy Basic Energy Sciences provided funding for this study. The authors thank Venessa O'Brien and Shannon Dulin for help with sampling, John Zumberge and Kendra Imbus (GeoMark Research, Inc.) for their assistance with the biomarker data, and Dougal McCarty and an anonymous reviewer for their constructive comments.

REFERENCES

Altaner, S.P. (1989) Calculation of K diffusional rates in bentonite beds. *Geochimica et Cosmochimica Acta*, **53**, 923–931.

Altaner, S.P. and Ylagan, R.F. (1997) Comparison of structural models of mixed-layer illite/smectite and reaction mechanisms of smectite illitization. *Clays and Clay Minerals*, **45**, 517–533.

Altaner, S.P., Hower, J., Whitney, G., and Aronson, J.L. (1984) Model for K-bentonite formation: Evidence from zoned K-bentonites from the disturbed belt, Montana. *Geology*, **12**, 412–415.

Aronson, J.L. and Lee, M. (1986) K/Ar systematics of bentonite and shale in a contact metamorphic zone, Cerrillos, New Mexico. *Clays and Clay Minerals*, **34**, 483–487.

Banerjee, S., Elmore, R.D., and Engel, M.H. (1997) Chemical remagnetization and burial diagenesis; testing the hypothesis in the Pennsylvanian Belden Formation, Colorado. *Journal of Geophysical Research*, **102**, 24825–24842.

Bauluz, B., Peacor, D.R., and Ylagan, R.F. (2002) Transmission electron microscopy study of smectite illitization during hydrothermal alteration of a rhyolitic hyaloclastite from Ponza, Italy. *Clays and Clay Minerals*, **50**, 157–173.

Blumstein, A.M., Elmore, R.D., Engel, M.H., Elliot[*sic*], C., and Basu, A. (2004) Paleomagnetic dating of burial diagenesis in Mississippian carbonates, Utah. *Journal of Geophysical Research*, **109**, B04101. doi: 10.1029/2003JB002698.

Clauer, N. (2006) Towards an isotopic modeling of the illitization process based on data of illite-type fundamental particles from mixed-layer illite-smectite. *Clays and Clay Minerals*, **54**, 116–127.

Clauer, N. and Lerman, A. (2012) Thermal history analysis of sedimentary basins: An isotopic approach to illitization. Pp. 125–146 in: *Analyzing the Thermal History of Sedimentary Basins*: *Methods and Case Studies* (N.B. Harris and K.E. Peters, editors). SEPM Special Publication No. **103**, Society for Sedimentary Geology, Tulsa, Oklahoma, USA.

Clayton, J., Mudge, M.R., Sr., Lubeck, C., and Daws, T.A. (1982) Hydrocarbon source rock evaluation of the Disturbed Belt, northwestern Montana. Pp. 773–793 in: *Geologic Studies of the Cordilleran Thrust Belt, Volume II* (R.B. Powers, editor). Rocky Mountain Association of Geologists, Denver, Colorado, USA, **2**, p. 773–793.

Cobban, W.A., Erdmann, C.E., Lemke, R.W., and Manghen, E.K. (1959) Revision of Colorado group on Sweetgrass arch, Montana. *AAPG Bulletin*, **43**, 2786–2796.

Derkowski, A., Bristow, T.F., Wampler, J.M., Środoń, J., Marynowski, L., Elliott, W.C., and Chamberlin, C.P. (2013) Hydrothermal alteration of the Ediacaran Doushantuo Formation in the Yangtze Gorges area (South China). *Geochimica et Cosmochimica Acta*, **107**, 279–298.

Eberl, D.D., Blum A.E., and Serravezza, M. (2011) Anatomy of a metabentonite: Nucleation and growth of illite crystals and their coalescence into mixed-layer illite/smectite. *American Mineralogist*, **96**, 586–593.

Elliott, W.C. and Aronson, J.L. (1987) Alleghanian episode of K–bentonite illitization in the southern Appalachian Basin. *Geology*, **15**, 735–739.

Elliott, W.C. and Aronson, J.L. (1993) The timing and extent of illite formation in Ordovician K-bentonites at the Cincinnati Arch, the Nashville Dome and north-eastern Illinois Basin. *Basin Research*, **5**, 125–135.

Elliott, W.C. and Haynes, J.T. (2002) The chemical character of fluids forming diagenetic illite in the Southern Appalachian Basin. *American Mineralogist*, **87**, 1519–1527.

Elliott, W.C. and Matisoff, G. (1996) Evaluation of kinetic models for the smectite to illite transformation. *Clays and Clay Minerals*, **44**, 77–87.

Elliott, W.C., Aronson, J.L., Matisoff, G., and Gautier, D.L. (1991) Kinetics of the smectite to illite transformation in the Denver Basin: clay mineral, K-Ar data, and mathematical model results. *The American Association of Petroleum Geologists Bulletin*, **75**, 436–462.

Elliott, W.C., Basu, A., Wampler, J.M., Elmore, R.D., and Grathoff, G.H. (2006a) Comparison of K-Ar ages of diagenetic illite-smectite to the age of a chemical remanent magnetization (CRM): An example from the Isle of Skye, Scotland. *Clays and Clay Minerals*, **54**, 314–323.

Elliott, W.C., Osborn, S.G., O'Brien, V.J., Elmore, R.D., Engel, M.H., and Wampler, J.M. (2006b) On the timing and causes of illite formation and remagnetization in the Cretaceous Marias River Shale, Disturbed Belt, Montana. *Journal of Geochemical Exploration*, **89**, 92–95.

Elmore, R.D., Muxworthy, A.R., and Aldana, M. (2012) Remagnetization and chemical alteration of sedimentary rocks. Pp. 1–21 in: *Remagnetization and Chemical Alteration of Sedimentary Rocks* (R.D. Elmore, A.R. Muxworthy, M.M. Aldana, and M. Mena, editors). Special Publications, **371**. Geological Society, London, doi:10.1144/SP371.15

Enkin, R.J. (2003) The direction-correction tilt test; an all-purpose tilt/fold test for paleomagnetic studies. *Earth and Planetary Science Letters*, **212**, 151–166.

Enkin, R.J., Osadetz, K.G., Baker, J., and Kisilevsky. D. (2000) Orogenic remagnetizations in the Front Ranges and Inner Foothills of the southern Canadian Cordillera: Chemical harbinger and thermal handmaiden of Cordilleran deformation. *Geological Society of America Bulletin*, **112**, 929–942.

Fisher, R. (1953) Dispersion on a sphere. *Proceedings of the Royal Society of London*, *Series A*, *Mathematical and Physical Sciences*, **217**, 295–305.

Gao, G., Elmore, R.D., and Land, L.S. (1992) Geochemical constraints on the origin of calcite veins and associated limestone alteration, Ordovician Viola Group, Arbuckle Mountains, Oklahoma, U.S.A. *Chemical Geology*, **98**, 257–269.

Garven, G. and Freeze, R.A. (1984) Theoretical analysis of the role of groundwater flow in the genesis of stratabound ore deposits. 1. Mathematical and numerical model. *American Journal of Science*, **284**, 1085–1124.

Gill, J.D., Elmore, R.D., and Engel, M.H. (2002) Chemical remagnetization and clay diagenesis: testing the hypothesis in the Cretaceous sedimentary rocks of northwestern Montana. *Physics and Chemistry of the Earth*, **27**, 1131–1139.

Hoffman, J. and Hower, J. (1979) Clay mineral assemblages as low grade metamorphic geothermometers: application to the thrust faulted disturbed belt of Montana, U.S.A. Pp. 55–79 in: *Aspects of Diagenesis* (P.A. Scholle and P.R. Schluger, editors). Society of Economic Paleontologists and Mineralogists, Special Publication **26**.

Hoffman, J., Hower, J., and Aronson, J.L. (1976) Radiometric dating of time of thrusting in the disturbed belt of Montana. *Geology*, **4**, 16–20.

Hower, J.F. (1981) X-ray diffraction of mixed layered clay minerals. Pp. 39–59 in: *Clays and the Resource Geologist* (F.J. Longstaffe, editor). Short Course **7**, Mineralogical Society of Canada.

Hower, J., Eslinger, E.V., Hower, M.E., and Perry, E.A. (1976) Mechanism of burial metamorphism of argillaceous sediment: 1. Mineralogical and chemical evidence. *Geological Society of America Bulletin*, **87**, 725–737.

Jackson, M.L. (1979) *Soil Chemical Analyses – Advanced Course*, second edition. Published by the author, Madison, Wisconsin, USA, 895 pp.

Jagodzinski, H. (1949) Eindimensionale Fehlordnung in Kristallen und ihr Einfluss auf die Röntgeninterferenzen. I. Berechnung des Fehlordnungsgrades aus den Röntgenintensitäten. *Acta Crystallographica*, **2**, 201–207.

Katz, B., Elmore, R.D., Cogoini, M., Engel, M.H., and Ferry, S. (2000) Associations between burial diagenesis of smectite, chemical remagnetization, and magnetite authigenesis in the Vocontian trough, SE France. *Journal of Geophysical Research*, **105(B1)**, 851–868.

Kent, D.V. (1985) Thermoviscous remagnetization in some Appalachian limestones. *Geophysical Research Letters*, **12**, 805–808.

Kim, J.-W. and Peacor, D.R. (2002) Crystal-size distributions of clays during episodic diagenesis: the Salton Sea Geothermal System. *Clays and Clay Minerals*, **50**, 371–380.

Kirschvink, J.L. (1980) The least-squares line and plane and the analysis of palaeomagnetic data. *Geophysical Journal of the Royal Astronomical Society*, **62**, 699–718.

Lowrie, W. (1990), Identification of ferromagnetic minerals in a rock by coercivity and unblocking temperature properties. *Geophysical Research Letters*, **17**, 159–162.

McArthur, J.M., Howarth, R.J., and Bailey, T.R. (2001) Strontium isotope stratigraphy: LOWESS version 3: Best fit to the marine Sr-isotope curve for 0–509 Ma and accompanying look-up table for deriving numerical age. *The Journal of Geology*, **109**, 155–170.

McCarty, D.K., Sakharov, B.A., and Drits, V.A. (2009) New insights into smectite illitization: A zoned K-bentonite revisited. *American Mineralogist*, **94**, 1653–1671.

Mearon, S., Paytan, A., and Bralower, T.J. (2003) Cretaceous strontium isotope stratigraphy using marine barite. *Geology*, **31**, 15–18.

Middleton, M.F. and Schmidt, P.W. (1982) Paleothermometry of the Sydney Basin. *Journal of Geophysical Research*, **87**, 5351–5359.

Moore, D.M. and Reynolds, R.C., Jr. (1997) *X-ray Diffraction and the Identification and Analysis of Clay Minerals*, second edition. Oxford University Press, New York, 378 pp.

Morton, J.P. (1985) Rb-Sr dating of diagenesis and source age of clays in Upper Devonian black shales of Texas. *Geological Society of America Bulletin*, **96**, 1043–1049.

Mudge, M.R. (1982) A resume of the structural geology of the Northern Disturbed Belt, northwestern Montana. Pp. 91–122 in: *Geologic Studies of the Cordilleran Thrust Belt, Volume I* (R.B. Powers, editor), Rocky Mountain Association of Geologists, Denver, Colorado, USA.

Nadeau, P.H. and Reynolds, R.C., Jr. (1981) Burial and contact metamorphism in the Mancos Shale: *Clays and Clay Minerals*, **29**, 249−259.

O'Brien, V.J., Moreland, K.M., Elmore, R.D., Engel, M.H., and Evans, M.A. (2007), Origin of orogenic remagnetizations in Mississippian carbonates, Sawtooth Range, Montana. *Journal of Geophysical Research*, **112**, B06103, doi:10.1029/2006JB004699.

Odin, G. and 35 collaborators (1982) Interlaboratory standards for dating purposes. Pp. 123−149 in: *Numerical Dating in Stratigraphy* (G.S. Odin, editor). John Wiley and Sons, New York.

Oliver, J. (1986) Fluids expelled tectonically from orogenic belts: Their role in hydrocarbon migration and other geologic phenomena. *Geology*, **14**, 99−102.

Oliver, J. (1992) The spots and stains of plate tectonics. *Earth-Science Reviews*, **32**, 77−106.

Osborn, S.G. (2006) The timing and causes of illite formation in the Cretaceous Marias River Shale, Disturbed Belt, Montana. M.S. Thesis, Georgia State University, Atlanta, Georgia, USA, 117 pp.

Osborn, S.G., McIntosh, J.C., Hanor, J.S., and Biddulph, D. (2012) Iodine-129, ^{87}Sr/^{86}Sr, and trace elemental geochemistry of northern Appalachian Basin brines: Evidence for basinal-scale fluid migration and clay mineral diagenesis. *American Journal of Science*, **312**, 263−287, doi: 10.2475/03.2012.01

Pevear, D.R. (1999) Illite and hydrocarbon exploration. *Proceedings of the National Academy of Sciences*, **96**, 3440−3446.

Pollastro, R.M., (1994) Considerations and applications of the illite/smectite geothermometer in hydrocarbon-bearing rocks of Miocene to Mississippian age: *Clays and Clay Minerals*, **41**, 119− 133.

Pullaiah, G., Irving, E., Buchan, K.L., and Dunlop, D.J. (1975) Magnetization changes caused by burial and uplift. *Earth and Planetary Science Letters*, **28**, 133−143.

Schoonmaker, J., Mackenzie, F.T., and Speed, R.C. (1986) Tectonic implications of illite/smectite diagenesis, Barbados accretionary prism. *Clays and Clay Minerals*. **34**, 465−472.

Sears, J.W. (2001) Emplacement and denudation history of the Lewis-Eldorado-Hoadley thrust slab in the northern Montana Cordillera, USA: Implications for steady-state orogenic processes. *American Journal of Science*, **301**, 359−373.

Seifert, W.K. and Moldowan, J.M. (1986) Use of biological markers in petroleum exploration. Pp. 261−290 in: *Biological Markers in the Sedimentary Record* (R.B. Johns, editor). Methods in Geochemistry and Geophysics, **24**, Elsevier, Amsterdam.

Środoń, J., Clauer, N., and Eberl, D.D. (2002) Interpretation of K-Ar dates of illitic clays from sedimentary rocks aided by modeling. *American Mineralogist*, **87**, 1528−1535.

Środoń, J., Clauer, N., Huff, W., Dudek, T., and Banaś, M. (2009) K-Ar dating of the Lower Palaeozoic K-bentonites from the Baltic Basin and the Baltic Shield: implications for the role of temperature and time in the illitization of smectite. *Clay Minerals*, **44**, 361−387.

Środoń, J., Paszkowski, M., Drygant, D., Anczkiewicz, A., and Bana M. (2013) Thermal history of Lower Paleozoic rocks on the Peri-Tornquist margin of the East European Craton (Podolia, Ukraine) inferred from combined XRD, K-Ar, and AFT data. *Clays and Clay Minerals*, **61**, 107−132.

Steiger, R.H. and Jäger, E. (1977) Subcommission on Geochronology: Convention on the use of decay constants in geo- and cosmochronology. *Earth and Planetary Science Letters*, **36**, 359−362.

Stroker, T.M., Harris, N.B., Elliott, W.C., and Wampler, J.M. (2013) Diagenesis of a tight gas sand reservoir: Upper Cretaceous Mesaverde Group, Piceance Basin, Colorado. *Marine and Petroleum Geology*, **40**, 48−68.

Torsvik, T.H., Van der Voo, R., Preeden, U., Mac Niocaill, C., Steinberger, B., Doubrovine, P.V., van Hinsbergen, D.J.J., Domeier, M., Gaina, C., Tohver, E., Meert, J.G., McCausland, P.J.A., and Cocks, L.R.M. (2012) Phanerozoic polar wander, palaeogeography and dynamics. *Earth-Science Reviews*, **114**, 325−368.

Totten, L.A. (2005) Geochemical and paleomagnetic assessments of organic-rich lithologies in the disturbed belt, Montana. M.S. thesis, Oklahoma University, Norman, Oklahoma, USA, 79 pp.

Tohver, E., Weil, A.B., Solum, J.G., and Hall, C.M. (2008) Direct dating of carbonate remagnetization by ^{40}Ar/^{39}Ar analysis of the smectite−illite transformation. *Earth and Planetary Science Letters*, **274**, 524−530.

West, N., Alexander, R., and Kagi, R.I. (1990) The use of silicalite for rapid isolation of branched and cyclic alkane fractions of petroleum. *Organic Geochemistry*, **15**, 499−501.

Woods, S., Elmore, R.D., and Engel, M. (2002) Paleomagnetic dating of the smectite-to-illite conversion: testing the hypothesis in Jurassic sedimentary rocks, Skye, Scotland. *Journal of Geophysical Research*, **107**, 10.1029/2000JB000053, EPM 2-1-2-12.

Zechmeister, M.S., Pannalal, S., and Elmore, R.D. (2012) A multidisciplinary investigation of multiple remagnetizations within the Southern Canadian Cordillera, SW Alberta and SE British Columbia. Pp. 123−144 in: *Remagnetization and Chemical Alteration of Sedimentary Rocks* (R.D. Elmore, A.R. Muxworthy, M.M. Aldana, and M. Mena, editors). Special Publications, **371**. Geological Society, London, doi:10.1144/SP371.11.

Ziegler, K. and Longstaffe, F.J. (2000) Multiple episodes of clay alteration at the Precambrian/Paleozoic unconformity, Applachian Basin: Isotopic evidence for long-distance and local fluid migrations. *Clays and Clay Minerals*, **48**, 474−493.

Zijderveld, J.D.A. (1967) A.C. demagnetization of rocks − analysis of results. Pp. 254−286 in: *Methods in Paleomagnetism* (D.W. Collinson, K.M. Creer, and S.K. Runcorn, editors). *Developments in Solid Earth Geophysics*, **3**. Elsevier, Amsterdam.

Zwing, A., Clauer, N., Liewig, N., and Bachtadse, V. (2009) Identification of remagnetization processes in Paleozoic sedimentary rocks of the northeast Rhenish Massif in Germany by K-Ar dating and REE tracing of authigenic illite and Fe oxides. *Journal of Geophysical Research*, **114**, B06104 http://dx.doi.org/10.1029/2008JB006137

(*Received 16 January 2014; revised 26 May 2014; Ms. 836; AE: R.J. Pruett*)

Clays and Clay Minerals, Vol. 62, No. 2, 126–136, 2014.

STOICHIOMETRIC REACTIONS DESCRIBING SERPENTINIZATION OF ANHYDROUS PRIMARY SILICATES: A CRITICAL APPRAISAL, WITH APPLICATION TO AQUEOUS ALTERATION OF CHONDRULE SILICATES IN CM CARBONACEOUS CHONDRITES

Michael A. Velbel*

Department of Geological Sciences, 206 Natural Science Building, Michigan State University, East Lansing,
Michigan 48824-1115, USA

Abstract—A number of chemical reactions (mass-action expressions) have been proposed to describe serpentinization of olivine in terrestrial serpentinites. Some have been applied to interpreting the formation of serpentine-group minerals in CM carbonaceous chondrites. The widely used olivine + pyroxene → serpentine (ol + px → srp) reaction is quantitatively inconsistent with observed ratios of olivine to pyroxene and olivine to serpentine in CM carbonaceous chondrites. The reaction of 5ol → 2srp is most consistent with constraints from textural observations at the scale of individual partial and complete pseudomorphs of serpentine after coarse olivine in CM chondrites, observed co-variations in modal abundances of reactant and product minerals in CM chondrites, and experimental geochemical kinetics. Furthermore, the 5ol → 2srp reaction provides insight into the mobility of solute species in the aqueous alteration environment of CM carbonaceous chondrites.

Key Words—CM Chondrite, Meteorite, Olivine, Serpentine.

INTRODUCTION

Carbonaceous chondrites are meteorites with primitive chemical compositions that are understood to come from undifferentiated asteroids (*e.g.* Dodd, 1981; Hutchison, 2004). Carbonaceous chondrites of the compositionally primitive (solar composition) and rare CI (Ivuna-like) group, the CR (Renazzo-like) group, and the much more abundant (Grady, 2000) CM (Mighei-like) group (Dodd, 1981; Hutchison, 2004) all contain appreciable modal abundances of phyllosilicates; several other varieties of carbonaceous chondrites contain little or no phyllosilicate material. Because they are much more abundant and exhibit variations in phyllosilicate abundance and composition, this paper emphasizes CM2 carbonaceous chondrites (where the number refers to the petrologic type). Current thinking is that petrologic type 3 was the ‘starting material’ and that petrologic types 2 and 1 may be products of increasing degrees of hydrous alteration of type 3 starting material (McSween, 1979a; Buseck and Hua, 1993). The CM chondrites are mostly petrologic type 2 (CM2; Hutchison, 2004), and a variety of subdivisions have been proposed to distinguish different degrees of aqueous alteration within CMs of petrologic type 2 (Zolensky *et al.*, 1993, 1997; Browning *et al.*, 1996; Rubin *et al.*, 2007; Chizmadia and Brearley, 2008; Howard *et al.*, 2009), and from petrologic type 2 to type 1 in CM chondrites (Zolensky *et al.*, 1997).

Serpentine-group phyllosilicates dominate the CM chondrites, constituting 67–88 vol.% of the CM chondrites examined to date (Howard *et al.*, 2009, 2011). Textural constituents of CM carbonaceous chondrites can be classified as coarse constituents and fine material. Coarse constituents (the “larger components” of Zolensky and McSween, 1988) include chondrules (the defining textural constituent of chondrites; generally spherical mm to sub-mm-sized silicate-dominated solids that are solidified droplets formed by flash heating and rapid cooling of precursor solids in the early solar nebula; Lofgren, 1989, 1996; Lofgren and Russell, 1986; Lofgren and Lanier, 1990; Hutchison, 2004), large mineral fragments, and refractory-element-rich calcium aluminum inclusions, CAIs (Hutchison, 2004). Fine materials in CM chondrites include matrix (fine-grained) and fine-grained rims on coarse constituents (see review by Velbel and Palmer, 2011, and references therein). Serpentine occurs in fine matrix and rims, and in coarse constituents as partial or complete pseudomorphs after (1) anhydrous phenocryst minerals in chondrules (Figure 1), and (2) isolated coarse anhydrous minerals. Matrix consisting predominantly of serpentine constitutes 57–85% of CM chondrites (McSween, 1979b). Because of their abundance and fine particle size, matrix and rim materials are particularly sensitive indicators of various alteration processes (*e.g.* Brearley, 2003, 2006).

Matrix in CM chondrites is compositionally heterogeneous at the scale of defocused-beam electron microprobe analyses, suggesting mechanical mixing of serpentines with diverse compositions, but mean and modal serpentine compositions vary systematically with

---

* E-mail address of corresponding author:
velbel@msu.edu
DOI: 10.1346/CCMN.2014.0620205

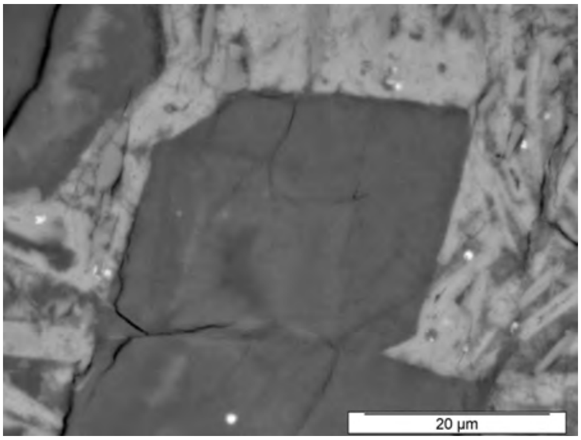

Figure 1. Pseudomorph of serpentine after altered chondrule-hosted olivine in the CM2 chondrite Nogoya. The euhedral outline of the precursor olivine is perfectly preserved. Mesostasis (intercrystalline chondrule glass) surrounding olivine crystals is altered before olivine in other CM2 chondrites. The absence of radial or concentric fractures in the altered mesostasis indicates that there was no volume change during the olivine−serpentine reaction. [This image is a close-up of the same region imaged by Velbel *et al.* (2012, figure 4a); see that paper for further discussion of this texture and phase assemblage.]

independent measures of aqueous alteration (McSween *et al.*, 1979b, 1987; Zolensky *et al.*, 1993; Browning *et al.*, 1996). Observations by transmission electron microscopy (TEM) show that ferroan serpentine-group minerals occur as solid solutions containing appreciable components of ferroan endmembers (*e.g.* cronstedtite, greenalite; Lauretta *et al.*, 2000; Zega and Buseck, 2003; Zega *et al.*, 2004, 2006; Chizmadia and Brearley, 2008) rather than as discrete endmember ferroan phyllosilicates. CM chondrite matrix, more Fe-rich than the chondrules in less-altered CM chondrites, becomes progressively enriched in more Mg-rich serpentine (more chrysotile endmember) with increase in various other measures of aqueous alteration in more altered CM chondrites (McSween and Richardson, 1977; McSween, 1979b, 1987; Zolensky *et al.*, 1993; Browning *et al.*, 1996; Howard *et al.*, 2009, 2011).

Zolensky *et al.* (1993, figure 4) illustrated that specimen-average Fe/(Fe+Mg) (wt.%) values vary from 0.4 to 0.9 in a suite of nine CM chondrites. Increasing Mg/Fe (decreasing Fe/(Fe+Mg) (wt.%) (Zolensky *et al.*, 1993) and corresponding increasing Mg/(Fe+Mg) (wt.%)) in matrix phyllosilicates with increasing CM chondrite alteration is generally (*e.g.* Zolensky *et al.*, 1993) attributed to differences in dissolution rates of olivines of the different compositions that co-exist in CM chondrites (*e.g.* Hanowski and Brearley, 2001; Velbel *et al.*, 2012). The formation of serpentine in matrix is generally advanced even in CM chondrites in which anhydrous coarse primary-mineral constituents (*e.g.* olivine and pyroxene phenocrysts in chondrules; isolated olivine and pyroxene fragments hosted in matrix) are unaltered. However, the increased Mg/(Fe+Mg) of matrix and rim serpentines in more altered CM chondrites suggests a shift from addition of Fe to matrix by alteration of fast-reacting minerals (especially ferroan olivine) in less-altered CM chondrites (forming Fe-rich serpentines), to increased contributions of Mg from the destruction of slower-altering forsteritic olivine at advanced-intermediate stages of aqueous alteration resulting in the formation of Mg-rich serpentines.

Matrix already exists and consists of serpentine even in CM chondrites in which the coarse chondrule olivine is unaltered, but becomes more magnesian in CM chondrites containing more altered coarse olivine. Hanowski and Brearley (2001) developed a four-stage model for the successive alteration of progressively more forsteritic olivine after the onset of the alteration of coarse olivine in chondrules. Observations from an even more altered CM chondrite were used by Velbel *et al.* (2012) to extend the Hanowski and Brearley (2001) model to Stage 5. Key attributes of the extended model are summarized in Table 1, along with related measures of aqueous alteration from the same CM chondrites on which the extended model is based, and the resulting relative abundances of mobile Fe and Mg in the solutions to which the olivine alteration would be contributing solutes at the various alteration stages. The observations and the inferences from them are all consistent with the long-expected relationship between increasingly magnesian serpentines observed in the matrices of more-altered CM chondrite and progressively more extensive alteration of the proposed Mg-source mineral, olivine (McSween and Richardson, 1977; McSween, 1979b, 1987; Zolensky *et al.*, 1993; Browning *et al.*, 1996; Howard *et al.*, 2009, 2011). The reader is directed to Velbel and Palmer (2011) and Velbel *et al.* (2012), for more detailed summaries of the recent state of knowledge of serpentine formation and compositional variation in fine-grained (matrix and rim) serpentine, and in serpentine formed by pseudomorphous replacement of coarse olivine (in chondrules and isolated fragments), respectively.

Primary anhydrous silicate minerals (*e.g.* pyroxene, olivine) in three groups of carbonaceous chondrites (CI, CR, and CM) were subjected to aqueous alteration (Brearley, 2003, 2006). Numerous workers (*e.g.* Bunch and Chang, 1980; Barber, 1985; Browning *et al.*, 2000; Hanowski and Brearley, 2001; Velbel *et al.*, 2012) have noted that replacement textures of primary coarse-grained olivines and pyroxenes in the abundant and well studied CM chondrites resemble terrestrial aqueous-alteration textures of ferromagnesian silicate minerals in terrestrial mafic/ultramafic rocks. Such textures include partial and complete pseudomorphic and alteromorphic replacement (after euhedral and anhedral primary minerals, respectively; Delvigne, 1998), meshwork serpentinization textures (Wicks and Whittaker, 1977), and "centripetal replacement" in which entire grains or fracture-bounded remnants are replaced from the margin inward (*e.g.* Delvigne, 1998; Boudier *et al.*, 2010). Hanowski and Brearley (2001) and Velbel *et al.* (2012) both reported textural observations from which they inferred that pseudomorphous replacement of coarse olivine by serpentine in chondrules and isolated coarse olivine grains is isovolumetric. Such textures and compositional observations constrain elemental redistribution from primary anhydrous silicates (*e.g.* olivine) to serpentine and to surrounding phases during serpentinization (*e.g.* Velbel *et al.*, 2012).

Given the apparently important role of alteration of coarse olivine in providing the Mg required to make matrices in more-altered CM chondrites more magnesian, the present study examines a number of different chemical reactions that have been proposed to describe terrestrial serpentinization, and assesses their suitability for the interpretation of serpentine pseudomorphs after coarse olivine in light of textural and modal-abundance data from CM2 carbonaceous chondrites. Note that matrix already consists predominantly of serpentine even before Stage 1 alteration (in the Hanowski and Brearley, 2001, model) of coarse constituents in chondrules begins. Furthermore, this paper distinguishes between (early) formation of matrix and the 'cronstedtite' that dominates it, and (late) alteration of coarse-grained/coarsely crystalline olivine. Discrete endmember cronstedtite (*sensu stricto*) does not occur in CM2 chondrites; cronstedtite occurs as one endmember in a solid-solution series. There are two solid-solution trends in the serpentine-group minerals of CM2 chondrites; one between chrysotile and greenalite endmembers, the other between chrysotile and cronstedtite. Discrete masses of serpentine-structured material with abundant ferric and tetrahedral iron (cronstedtite *sensu lato*) occur in the fine-grained constituents (matrix and rims) of many CM2 chondrites (Müller *et al.*, 1979; Lauretta *et al.*, 2000; Zega and Buseck, 2003; Zega *et al.*, 2004, 2006; Chizmadia and Brearley, 2008), but not among the serpentine pseudomorphic after coarse anhydrous primary silicates that are the target of this study. The matter of whether cronstedtite in rim and matrix might also be produced by isovolumetric reactions remains to be resolved by future work, but Müller *et al.* (1979) argued explicitly against this possibility. In summary, much of the formation of Fe-rich serpentine-group minerals in CM2 rim and matrix (*e.g.* abundant cronstedtite component in the serpentine solid-solution) has occurred before the phenomenon being investigated in the present study has begun. After exploring the usefulness of different serpentinization reactions, this paper also briefly explores some implications of the choice of reaction for interpretation of elemental mobility in the aqueous solutions that drove serpentinization on the CM2 chondrite parent-body/ies.

MASS-ACTION EXPRESSIONS AND ASSOCIATED ELEMENTAL MASS-TRANSFER DURING AQUEOUS ALTERATION OF OLIVINE TO SERPENTINE

Olivine-serpentinization reactions

At the scale of meteorite-specimen bulk chemistry, aqueous alteration of carbonaceous chondrites is isochemical (DuFresne and Anders, 1962; Clayton and Mayeda, 1999; Young *et al.*, 2003; Brearley, 2003, 2006; Rubin *et al.*, 2007; Bland *et al.*, 2009). However, every individual reaction between anhydrous primary minerals and hydrous alteration products requires and/or evolves some elements or chemical species (at minimum, water) other than those hosted entirely within the reactant and/or product minerals. The elemental mobility required by a variety of olivine-alteration and olivine-serpentinization reactions that have been proposed for terrestrial serpentinization and similar reactions in extraterrestrial materials are explored here.

A number of stoichiometric mass-action expressions for the serpentinization of olivine have been proposed. For the purposes of illustration, Mg endmembers are used here to introduce different variants of serpentinization reactions. As already noted above, much of the formation of ferroan serpentine-group minerals in matrix (*e.g.* abundant cronstedtite component in the serpentine solid-solution) has occurred before pseudomorphous replacement of olivine by Mg-rich serpentine discussed herein has begun (before Stage 1 of Table 1). After the onset of Stage 1 olivine alteration (Hanowski and Brearley, 2001), either cronstedtite-rich serpentines reacted with Mg to form more magnesian serpentine (*e.g.* Zega *et al.*, 2006), or newly formed Mg-rich serpentine diluted the previously formed matrix; in either case, CM2 matrices are more Mg-rich with more advanced progress through Stages 1 through 5 of Table 1. Thus, formation of cronstedtite-rich matrix serpentines falls outside the scope of this work, which emphasizes pseudomorphism of coarse olivine after most of the ferroan matrix material has already formed. Also, because much terrestrial serpentinization of olivine involves highly forsteritic olivine ($Fo_{\sim 85-95}$), Mg endmembers are used in most of the literature from which the reactions are cited.

The most common (*e.g.* Martin and Fyfe, 1970; Coleman, 1971; Hemley *et al.*, 1977; Wegner and Ernst, 1983; O'Hanley, 1996; Viti and Mellini, 1998; Schulte *et al.*, 2006; Evans, 2008, reaction 1) is one in which both Mg and Si are retained in mineral products at some spatial scale, so that two formula units of olivine are destroyed by reaction with water, forming one formula unit each of serpentine and brucite (reaction 1).

$$2Mg_2SiO_4 + 3H_2O \rightarrow Mg_3Si_2O_5(OH)_4 + Mg(OH)_2 \qquad (1)$$

A reaction of the same form that conserves both Mg and Si with the same proportions of phases (2ol → srp + brc;

Table 1. Textural criteria, ratios of hydrous/anhydrous-silicate modal abundances, and examples of meteorites showing different extents of aqueous alteration in CM2 chondrules (adapted from Hanowski and Brearley, 2001).

Stage (Hanowski and Brearley, 2001)		1	2	3	4	5*
Matrix silicates entirely of serpentine and mesostasis completely altered; alteration of:	Fa in Type IIA chondrules	Unaltered	Incipient	Advanced	Nearly complete	Nearly complete
	Fo in chondrules	Unaltered	Unaltered	Incipient	Moderate	Advanced
	Metal/sulfide grains in chondrules	Small grains, completely	Larger grains, completely	Larger grains completely	All grains, completely	All grains, completely
Inferred Fe and Mg content in fluid		Very high Fe	High Fe	High Mg	Very high Mg	Even higher Mg
Phyllosilicate/anhydrous modal abundance ratio (Howard *et al.*, 2011)		Murchison (3.10) Murray (3.24)	3.74		3.94	4.09
Meteorite(s) (and Rubin *et al.*, 2007 petrologic sub-type)		Murchison (CM2.5) Murray (CM2.4/5)	Mighei (CM2.3)	LEW 90500	ALH 81002	Nogoya (CM2.2)

Qualitative criteria for stages 1−4 adapted from Hanowski and Brearley (2001).
* Extended to stage 5 by Velbel *et al.* (2012). Additional data from Rubin *et al.* (2007) and Howard *et al.* (2011).

abbreviations from Kretz, 1983) but real rather than endmember mineral compositions were used by Bach *et al.* (2006). The volumetric relationships among the reactants and products for reaction 1 were illustrated by O'Hanley (1996) as follows.

$$88\ \text{cm}^3 \rightarrow 111\ \text{cm}^3 + 25\ \text{cm}^3 = 137\ \text{cm}^3 \qquad (1a)$$

The 53% volume increase (equation 1a) illustrates the "Volume Problem" of serpentinization (see reviews by Coleman, 1971, and O'Hanley, 1996), in which solid volume must have increased as a consequence of serpentinization, but for which field evidence consistent with demonstrable structural volume increase was long lacking (O'Hanley, 1992). Using molar volumes (Table 2) for minerals from Smyth and Bish (1988), the solid volume relationships before and after reaction can be expressed as follows.

$$87.2\ \text{cm}^3 \rightarrow 107.3\ \text{cm}^3 + 24.5\ \text{cm}^3 = 131.8\ \text{cm}^3 \qquad (1b)$$

This corresponds to a 51% volume increase (Table 3).

Several other stoichiometric reactions have been used in support of chemical and/or isotopic modeling of aqueous alteration in carbonaceous chondrites. In one (originally written for terrestrial serpentinization by Graham, 1917; Hostetler *et al.*, 1966; Martin and Fyfe, 1970; Viti and Mellini, 1998; applied to aqueous alteration of carbonaceous chondrites by Clayton and Mayeda, 1999; Cohen and Coker, 2000; Guo and Eiler, 2007), one formula unit of olivine and one formula unit of pyroxene react with water to form one formula unit of

Table 2. Molar volumes of minerals relevant to serpentinization and/or CM chondrites.

Mineral group	Mg endmember Name	 Symbol	 Molar volume (cm^3/mol)	Fe endmember Name	 Symbol	 Molar volume (cm^3/mol)
Olivine	Forsterite	Fo	43.6	Fayalite	Fa	46.3
Pyroxene	Enstatite (ortho)	En	62.7	Ferrosilite (ortho)	Fs	65.9
Serpentine	Lizardite	Lz	107.3			
	Talc	Tlc	136.6			
	Brucite	Brc	24.5			
	Magnesite	Mgs	28.0			

Mineral symbols from Kretz (1983).
Molar volumes from Smyth and Bish (1988).
The actual formula for the Mg-rich lizardite for which Smyth and Bish (1988) determined the molar volume is $(Mg_{2.79}Fe^{2+}_{0.04}Fe^{3+}_{0.10}Al_{0.07})(Si_{1.83}Al_{0.17})O_5(OH)_4$.

Table 3. Stoichiometric coefficients of minerals and chemical species in chondrite-relevant Mg-endmember olivine alteration reactions.

Reaction	Ol	Px	Srp	Tlc	Water	CO_2	H^+	H_4SiO_4	Mg^{2+}	Brc	Mgs	ΔV(%)	Source
1	−2	0	1	0	−3	0	0	0	0	1	0	+51	O'Hanley (1996)
2	−1	−1	1	0	−2	0	0	0	0	0	0	+0.65	Graham (1917) Clayton and Mayeda (1999) Cohen and Coker (2000) (nearly isovolumetric)
3	−4	0	0	1	−1	−5	0	0	0	0	5	+59	Young *et al.* (1999)
4	−3	0	2	0	−2	0	0	−1	0	0	0	+64	Graham (1917) O'Hanley (1996)
5	−2	0	1	0	−1	0	−2	0	1	0	0	+23	This study
6	−5	0	2	0	−2	0	−8	1	4	0	0	−1.6	This study (nearly isovolumetric)

Mineral symbols from Kretz (1983).
Stoichiometric coefficients are negative for minerals consumed during forward reactions, positive for minerals produced.
Volumetric changes based on molar volumes from Smyth and Bish (1988) (see Table 2 and text).

serpentine (ol + en → srp; abbreviations from Kretz, 1983) (reaction 2).

$$Mg_2SiO_4 + MgSiO_3 + 2H_2O \rightarrow Mg_3Si_2O_5(OH)_4 \qquad (2)$$

Using molar volumes (Table 2) for forsterite, enstatite, and serpentine from Smyth and Bish (1988), solid volumes before and after reaction can be determined (2a).

$$43.6\ cm^3 + 63\ cm^3 = 106.6\ cm^3 \rightarrow 107.3\ cm^3 \qquad (2a)$$

Like the classic serpentinization reaction 1, all Mg and Si released by destruction of primary anhydrous silicates is retained in solid products. Unlike the classic reaction 1, solid volume is within 1% of isovolumetric for this reaction (Table 3).

In another olivine alteration reaction applied to modeling of aqueous alteration in carbonaceous chondrite parent bodies (Young *et al.*, 1999), four formula units of olivine react with water and carbon dioxide to form one formula unit of talc and five formula units of magnesite (4ol → tlc + 5mgs; abbreviations from Kretz, 1983) (reaction 3):

$$4Mg_2SiO_4 + H_2O + 5CO_2 \rightarrow Mg_3Si_4O_{10}(OH)_2 + 5MgCO_3 \qquad (3)$$

Using molar volumes (Table 2) for minerals from Smyth and Bish (1988), solid volumes before and after reaction can be calculated (3a).

$$\underset{(4 \times 43.6\ cm^3/mol)}{174.4\ cm^3\ \text{olivine}} \rightarrow 136.6\ cm^3\ \text{talc} + \underset{(5 \times 28.0\ cm^3/mol)}{140\ cm^3\ \text{magnesite}} \qquad (3a)$$

In this reaction, the product mineral assemblage invokes talc as a simplified proxy for smectite-group phyllosilicate (which occurs in the more rare petrologic type CI1 carbonaceous chondrites; Dodd, 1981; Hutchison, 2004), and magnesite for the carbonate minerals of carbonaceous chondrites (Young *et al.*, 1999). The 59% volume increase consequent upon this reaction is similar to that of the classic olivine to serpentine plus brucite reaction 1 (Table 3).

All the aforementioned previously used reactions assume reaction with water (plus or minus carbon dioxide), and invoke the assumption that all Mg and Si released during alteration of primary anhydrous silicate minerals is retained in their alteration products (Table 3). Less restrictive reactions involving water can be written, *e.g.* if all Mg released during destruction of olivine is retained in serpentine but Si is not similarly restricted, reaction 4 can be written.

$$3Mg_2SiO_4 + H_4SiO_{4(aq)} + 2H_2O \rightarrow 2Mg_3Si_2O_5(OH)_4 \qquad (4)$$

(3ol → 2srp; modified from Graham, 1917; Hostetler *et al.*, 1966; Coleman, 1971; O'Hanley, 1996; Viti and Mellini, 1998; see also Frost and Beard, 2007; applied to CM chondrites by Howard *et al.*, 2009). Using molar volumes (Table 2) for minerals from Smyth and Bish

(1988), solid volumes before and after reaction can be shown (4a).

$$130.8\ \text{cm}^3\ \text{olivine} \rightarrow 214.6\ \text{cm}^3\ \text{serpentine} \quad (3 \times 43.6\ \text{cm}^3/\text{mol}) \quad (2 \times 107.3\ \text{cm}^3/\text{mol}) \tag{4a}$$

The 64% volume increase consequent upon this reaction is similar to that of the classic olivine to serpentine plus brucite reaction 1 (Table 3).

Alternatively, if all Si released during destruction of olivine is retained in serpentine but Mg is not similarly restricted, reaction 5 results.

$$2Mg_2SiO_4 + 2H^+ + H_2O \rightarrow Mg_3Si_2O_5(OH)_4 + Mg^{2+} \tag{5}$$

A similar 2ol → srp reaction with different descriptions of the mobile solute species was used by Coleman (1971). Using molar volumes (Table 2) for minerals from Smyth and Bish (1988), solid volumes before and after reaction can be calculated (5a).

$$87.2\ \text{cm}^3\ \text{olivine} \rightarrow 107.3\ \text{cm}^3\ \text{serpentine} \quad (2 \times 43.6\ \text{cm3/mol}) \tag{5a}$$

The 23% volume increase consequent upon this reaction (2ol → srp) is smaller than that of the classic olivine to serpentine plus brucite reaction 1 (Table 3). Condie and Madison (1969) invoked both importation of Si (as in reaction 4, but unlike reaction 5) and export of Mg (not a phenomenon of reaction 4, but common in many other reactions including reaction 5) to explain observed whole-rock bulk-compositional relationships of serpentinized dunite, and also inferred volume expansion; these relationships are consistent with both reactions (4) and (5) for whole-rock-scale serpentinization.

An isovolumetric reaction for the hydration of forsterite to serpentine + brucite was written by O'Hanley (1996, p. 15) who noted that mobile products included excess Mg and Si. The reaction was dismissed by O'Hanley (1996) on the grounds that Mg and Si metasomatism is not observed in the rocks surrounding terrestrially serpentinized rock bodies. Other isovolumetric reactions (*e.g.* reactions not producing brucite) have not yet been considered for application to carbonaceous chondrites. Velbel and Barker (2008) and Velbel *et al.* (2009) observed replacement textures consistent with isovolumetric replacement by several different phyllosilicates after several different primary minerals (chain-silicates) during terrestrial weathering. They also reported that unexpected elemental mobility is required during early weathering for phyllosilicates of the observed compositions to isovolumetrically replace primary minerals of known composition. According to Velbel and Barker (2008), Fe had to be imported into the pseudomorphic-replacement microenvironment in order to produce nontronitic smectite of the observed composition from the weathering of pyroxenes of the observed composition in the naturally weathered terrestrial pyroxenite they studied. Similarly, Al had to be imported into the partially pseudomorphic (Velbel *et al.*, 2009) (septoalteromorphic, in the terminology of Delvigne, 1998) microenvironment to produce kaolin-group minerals from hornblende, and Price *et al.* (2013) identified the external source mineral of the required Al.

Following the approach of Velbel and Barker (2008) and Velbel *et al.* (2009), a reaction describing isovolumetric replacement of olivine by serpentine can be written (reaction 6):

$$5Mg_2SiO_4 + 8H^+ + 2H_2O \rightarrow 2Mg_3Si_2O_5(OH)_4 + 4Mg^{2+} + H_4SiO_{4(aq)} \tag{6}$$

A similar 5ol → 2srp isovolumetric reaction with different descriptions of the mobile solute species was used by Hostetler *et al.* (1966) and Thayer (1966). Using molar volumes (Table 2) for minerals from Smyth and Bish (1988), solid volumes before and after reaction are expressed as follows (6a):

$$218.0\ \text{cm}^3\ \text{Forsterite} \rightarrow 214.6\ \text{cm}^3\ \text{Serpentine} \quad (5 \times 43.6\ \text{cm}^3/\text{mol}) \quad (2 \times 107.3\ \text{cm}^3/\text{mol}) \tag{6a}$$

This reaction (5ol → 2srp) is nearly isovolumetric, with a decrease in volume of <2% (Table 3). This reaction explicitly embodies the hydrolysis and hydration aspects of serpentinization reactions discussed by Evans (2008).

The discussion of Plümper *et al.* (2012) on isovolumetric replacement of olivine by serpentine during terrestrial serpentinization is for the most part superb. However, their reaction 8 is based on oversimplifications (by rounding) of the molar volumes of olivine and serpentine. The molar volume of forsterite was overestimated by Plümper *et al.* (2012) (they used 50 cm^3/mol instead of the actual value of 43.6 cm^3/mol) and underestimated the molar volume of serpentines (they used 100 cm^3/mol instead of the actual value of 107.3 cm^3/mol). This results in some misleading consequences for the resulting mass-action expression, specifically the ratios of olivine to serpentine formula units and the stoichiometric coefficients of the mobile solutes. Using oversimplified molar volumes resulted in a 2:1 olivine:serpentine ratio instead of the correct value of 5:2 (reaction 6 in the present study). The 2:1 ol:srp reaction of Plümper *et al.* (2012) does not produce mobile Si as isovolumetric serpentinization of olivine by serpentine should when written in the volumetrically correct form of Hostetler *et al.* (1966), Thayer (1966), and reaction 6 above. As Plümper *et al.* (2012) were not concerned with and, therefore, did not discuss Si mobility, their sound qualitative conclusions about Mg mobility are not affected by this approximation, but this is an example of how seemingly inconsequential simplifications useful in one context can have negative consequences in other contexts.

The six reactions examined above are not an exhaustive survey of all possibilities (for some other reactions, see also Hostetler *et al.*, 1966; Schulte *et al.*, 2006; and Frost and Beard, 2007). They do, however, include several that have been applied previously to carbonaceous chondrites, and they illustrate several important aspects of choosing appropriate reactions for interpreting the geochemical/cosmochemical conditions under which aqueous alteration occurred:

(1) All describe aqueous alteration of olivine, but to different phyllosilicate products; most reactions apply to production of serpentine, but reaction 3 invokes talc as a proxy for smectite-group minerals known from a small number of chondrites.

(2) Some reactions produce ancillary non-phyllosilicate products (brucite, magnesite) and may not be appropriate to situations lacking the required abundances of such products within pseudomorphs/alteromorphs after olivine. For example, note that direct application of reaction 1 would be appropriate for systems in which serpentine and brucite were formed in equimolar abundances. Brucite is documented from Nogoya (Bunch and Chang, 1980), and the brucite-like hydroxide layer in discrete tochilinite and interstratified tochilinite-serpentine common in CM chondrites (Mackinnon and Zolensky, 1984; Tomeoka *et al.*, 1989; Buseck and Hua, 1993) also occurs in Nogoya (Zolensky *et al.*, 1993) and may serve as a brucite-like sink for Mg not taken up in other alteration products. Recent whole-sample quantitative X-ray diffraction analyses detected but could not quantify abundances of tochilinite or tochilinite-serpentine intergrowths (Howard *et al.*, 2009, 2011). Furthermore, all previously documented occurrences of tochilinite or interstratified serpentine-tochilinite have been in matrix and rims; the fact that these brucite-like layers occur 'outside' the pseudomorphs/alteromorphs after olivine means that brucite-like layers are not among the products the volume of which must be considered 'within' the pseudomorphs/alteromorphs described by the proposed reactions.

(3) The ratio of olivine destroyed to serpentine formed varies among serpentine-forming reactions, from 1.5 (reaction 4) to 2.5 (reaction 6), even if no other reactants (*e.g.* pyroxene; reaction 2) are involved (Table 3). Consequently, the mere coexistence of olivine and serpentine (or olivine and serpentine and brucite, or olivine and serpentine and interstratified tochilinite-serpentine) in a phase assemblage is not sufficient to identify the reaction responsible. Instead, quantitative modal analysis (*e.g.* Howard *et al.*, 2009, 2011) is required, and must be of sufficient sensitivity to discriminate among the different co-variations of olivine and serpentine expected from the different reactions.

Assessing the suitability of different serpentinization reactions for application to CM chondrites

Generally, the material immediately surrounding pseudomorphs/alteromorphs after individual coarse olivine crystals/grains in carbonaceous chondrites contains no systematic evidence (*e.g.* demonstrably pre-terrestrial, indigenous radial or concentric fractures) of volume change (Hanowski and Brearley, 2001; Velbel *et al.*, 2012). Within porphyritic olivine chondrules, mesostasis is usually the first chondrule silicate phase to alter to phyllosilicates (Fuchs *et al.*, 1973) while ferroan olivine is still unaltered (Hanowski and Brearley, 2001, their Stage 1). The commonly observed perfect pseudomorphism of serpentine after olivine (*e.g.* figure 4b of Velbel *et al.*, 2012) combined with the absence of radial or concentric fractures within the pseudomorphs, between them and their surroundings, and in the surrounding previously altered mesostasis (Figure 1), all suggest negligible volume change during serpentinization of single olivine crystals. Therefore, at the scale of the individual coarse primary olivine grains and their alteration products in CM chondrites, partial and complete replacement of olivine by serpentine in CM2 chondrites was isovolumetric (*e.g.* Hanowski and Brearley, 2001). On this basis, reactions 1, 3, 4, and 5 can be dismissed; they are not accurate descriptions of 'mineral-scale' alteration in CM2 chondrites (although they may still be applicable to 'larger-than-grain-scale' alteration such as that reported by Lee *et al.* (2012), which is beyond the scope of this paper).

Reactions 2 and 6 are both isovolumetric within a few volume percent. However, they are not equally consistent with the ensemble of available observations. Olivine alteration in CM chondrites can and must proceed with mass-action expressions other than reaction 2 (ol + px → srp). The mole-for-mole stoichiometric coupling of olivine and pyroxene destruction required by reaction 2 is inconsistent with a number of observations. These include: (1) The generally unequal abundances of olivines and pyroxenes in CM chondrites (*e.g.* Rosenberg *et al.*, 2001; Bland *et al.* 2004; Howard *et al.*, 2009, 2011); (2) the observed depletion ratios of CM olivine and pyroxene during aqueous alteration (data from Howard *et al.*, 2011); (3) the observed ratios of CM olivine decrease to CM serpentine increase during aqueous alteration (data from Howard *et al.*, 2011); (4) the known unequal mineral-solution reaction rates of these minerals over the temperature range of interest (*e.g.* Goldich, 1938; Velbel, 1993; Brantley, 2005, 2008).

The next several paragraphs elaborate on several of these points.

Some CM and CM-like primitive chondrites (Murchison, Cold Bokkeveld, Nawapali, Cochabamba, Acfer 094, El-Quss Abu Said) contain abundant fine-grained pyroxene along with olivine in their matrices (Barber, 1981; Greshake, 1997; Nakamura *et al.*, 2008), which may have reacted simultaneously with matrix olivine consistent with reaction 2, but this is only relevant to the alteration of coarse-grained olivine if coarse or matrix pyroxene were available in abundances sufficient for reaction 2 (ol + px → srp) to both proceed in matrix olivine and continue in coarse olivine (as observed by Hanowski and Brearley, 2001, and Velbel *et* *al.*, 2012) before the matrix pyroxene was exhausted. The paucity of primitive (petrologic type 3) CM chondrites presently limits the ability to quantitatively test such modal-abundance relationships. However, some CM chondrites reach high levels of olivine depletion even after pyroxene has been completely depleted (Howard *et al.*, 2011). This could be taken to mean that the pyroxene was depleted in a coupled ol + px → srp reaction, that olivine occurred in excess of pyroxene, that olivine reacted more slowly, and, therefore, that the olivine was not completely altered. Alternatively, this could indicate that olivine alteration can continue even in the absence of simultaneous pyroxene alteration. In the absence of better quantitative evidence for high pre-alteration pyroxene abundances in what are now petrologic type 2 CM chondrites, the case for applying reaction 2 to pseudomorphic replacement of coarse olivine is weak.

From the least altered to the most altered CM2 chondrites examined by quantitative X-ray diffraction (XRD), the modal volume percentage sum of anhydrous silicates (olivine and pyroxene) decreases by almost exactly same amount as the modal volume percentages of serpentine-group phyllosilicates increase (Howard *et al.*, 2011: table 1, figure 5). Within uncertainties (~20% relative), these measurements appear consistent with replacement reaction 2 in which the volume of serpentine produced equals the volume of olivine and pyroxene destroyed. More detailed examination of the 'molar' ratios associated with the aforementioned modal proportions reveals the failure of reaction 2 to conform to observations, however. From the least altered to the most altered CM2 chondrites examined by quantitative XRD, modal volume percentages of olivine decrease from 23.1% to 4.0% (a difference of 19.1% modal) while pyroxene decreases from 9.8% to 0% (a difference of 9.8% modal) (Figure 2, data from Howard *et al.*, 2011). In other words, Δol(modal) ≈ 2 × Δpx(modal); ~2 modal % olivine is consumed by the actual alteration reaction for every 1 modal % pyroxene consumed. Because the molar volumes of olivine and pyroxene differ substantially (reaction 2a), the 'molar' proportion of olivine/pyroxene consumed is substantially different (7).

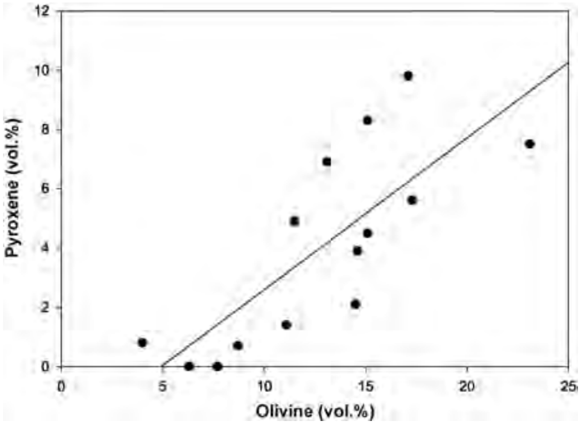

Figure 2. Modal percentages of olivine and pyroxene in CM chondrite falls and finds QUE 97990, Y 791198, Murchison, Murray, Mighei, ALHA81002, Nogoya, Essebi, Cold Bokkeveld, QUE 93005, ALH 83100, MET 01070, MET 01070 (2), and SCO 06043, (from highest to lowest modal olivine abundance) with linear regression. (Data from Howard *et al.*, 2011, table 1.)

$$(19.1\ \mathrm{cm^3_{ol}}/9.8\ \mathrm{cm^3_{px}}) \times (63\ \mathrm{cm^3_{px}\ mol^{-1}_{px}}/43.6\ \mathrm{cm^3_{ol}\ mol^{-1}_{ol}}) = 2.82\ \mathrm{mol_{ol}/mol_{px}} \quad (7)$$

Observed modal-abundance depletions of olivine and pyroxene (Figure 2; Howard *et al.*, 2011) thus show that Δol(molar) ≈ 3 × Δpx(molar); nearly three moles of olivine are depleted by aqueous alteration reactions for each mole of pyroxene depleted. These 'observed' proportions (Δol(molar) ≠ Δpx(molar) by nearly a factor of three) are incompatible with the equimolar consumption of olivine and pyroxene (Δol(molar) = Δpx(molar)) as required by widely used reaction 2.

Finally, the observed value of the ratio of molar olivine depleted to molar serpentine produced in CM2 chondrites (determined from the ranges of modal depletion of olivine and modal increase of serpentine as measured by Howard *et al.*, 2011, as shown in equation 8) is 2.9.

$$(19.1\ \mathrm{cm^3_{ol}}/16.2\ \mathrm{cm^3_{srp}}) \times (107.3\ \mathrm{cm^3_{srp}\ mol^{-1}_{srp}}/43.6\ \mathrm{cm^3_{ol}\ mol^{-1}_{ol}}) = 2.90\ \mathrm{mol_{ol}/mol_{srp}} \quad (8)$$

This demonstrates that reaction 6 (5ol → 2srp), which yields the highest ol:srp ratio (2.5) of any reaction considered here (Table 3), conforms most closely to the observed co-variations between olivine depletion and serpentine enrichment in altered CM carbonaceous chondrites.

The several lines of reasoning summarized in the previous paragraphs demonstrate that reaction 2 (ol + px → srp) is not a satisfactory description of serpentinization phenomena in CM chondrites. In contrast, the isovolumetric 5ol → 2srp reaction 6 as written is appropriate for replacement of anhydrous silicates 'at the grain scale', as water in the products was not initially present within the volume of the anhydrous reactant-mineral grain that was replaced, and was instead added to the volume within which replacement of the initially parent-mineral occurred. Volumes computed for all the reactions summarized above are for silicate and hydroxide (and in one case, carbonate) mineral phases only. If the water involved in the reactions was initially present as ice, initial (reactant) solid volumes would have to include the volume of reactant ice. This can be an important concern at the whole-rock scale (*e.g.* Clayton and Mayeda, 1999; Cohen and Coker, 2000; Bland *et al.*, 2009; Lee *et al.*, 2012). The reactions written above apply without such modification, however, in the case of 'grain-scale' replacement (isovolumetric or otherwise) of initially anhydrous silicates (*e.g.* olivine). Any water incorporated into a pseudomorph or alteromorph after an anhydrous reactant silicate (and that may or may not result in product volume being different from reactant volume) originated from outside the anhydrous reactant mineral, would not be part of the pre-alteration volume of the reactant mineral grain, and would have been added to the pseudomorph or alteromorph from outside its initial volume.

There exists a hierarchy of spatial scales in rocks subjected to aqueous alteration, including individual pseudomorphs (each of which must generally be a small open geochemical alteration microsystem, *sensu* Nahon, 1991 and Delvigne, 1998) and the whole rock. At the bulk-sample scale, hydration of CM2 chondrites appears isochemical (except for the O and H of water), with little evidence for metasomatic element mobility beyond the whole-rock scale (DuFresne and Anders, 1962; Clayton and Mayeda, 1999; Young *et al.*, 2003; Brearley, 2003, 2006; Rubin *et al.*, 2007; Bland *et al.*, 2009). On the basis of the preceding examination of reactions 1–6, however, isovolumetric replacement of coarse olivine by serpentine as described by reaction 6 (5ol → 2srp) satisfies presently understood textural, modal-abundance, and kinetic constraints for replacement of olivine by serpentine at the scale of an individual pseudomorph. At the scale of an individual pseudomorph, reaction 6 requires open-system behavior – several mobile species must be added to (H^+, H_2O) or removed from (Mg^{2+}, $H_4SiO_{4(aq)}$, and in real, non-endmember solid solutions, Fe) the pseudomorphic/alteromorphic replacement volume, by elemental mass transfer between the pseudomorphed volume and its surroundings. Each such individual volume described by reaction 6 (or a similar reaction for other primary-secondary mineral pairs) is only a small fraction of the whole rock.

Alteration may be isochemical at the whole-rock scale if smaller contained 'importing' and 'exporting' volumes experienced compensating mass transfers resulting in whole-rock scale mass balance (i.o.w., the large closed system consists of small local open systems). The import-export (open system) behavior of the volumes that are pseudomorphic after olivine as described by reaction 6 can be used to gain additional insight about elemental mass transfer among different volumes within an altered CM2 chondrite from compositional data on olivines and the serpentines that replace them (*e.g.* Hanowski and Brearley, 2001; Velbel *et al.*, 2012), as will be demonstrated for H^+, H_2O, Mg^{2+}, $H_4SiO_{4(aq)}$, and Fe in the next contribution in this series.

CONCLUSIONS

A number of chemical reactions (mass-action expressions) have been proposed to describe serpentinization of olivine in terrestrial serpentinites. Among those serpentinization reactions that have been proposed to explain replacement of olivine by serpentine in CM2 carbonaceous chondrites, the isovolumetric 5ol → 2srp reaction best satisfies presently understood textural, modal-abundance, and kinetic constraints. This isovolumetric replacement of olivine by serpentine requires that several solute and/or solvent chemical species be added to or removed from the pseudomorphic/alteromorphic replacement volume. Isochemical whole-rock-scale aqueous alteration of CM2 chondrites may be a consequence of element exchange between smaller (*e.g.* individual-pseudomorph-scale) volumes with 'importing' and 'exporting' (open system) behavior for different elements, that sum over all microsystem volumes to whole-rock-scale mass balance and bulk-sample isochemical alteration because of compensating mass transfers among the smaller-scale internal alteration microsystems.

ACKNOWLEDGMENTS

The author thanks his colleagues Mike Zolensky, Eric Tonui, Ian Mackinnon, Oliver Plümper, Joe Nuth, Hap McSween, Adrian Brearley, Alexander Krot, Maggie McAdam, Jessica M. Sunshine, Kieran T. Howard, Tim McCoy, Bob Clayton, Alan Rubin, Ed Young, Eric Palmer, Frans Rietmeijer, Jeff Grossman, and Anton Kearsley, for helpful discussions and correspondence; Craig Schwandt, Loan Le, Jason Price, Cari Corrigan, Amy McAdam, Angela Donatelle, Dan Snyder, Anna Losiak, Kathleen Jeffery, Gabrielle Tepp, Laurel Eibach, and Mike Wright for assistance in the laboratory and stimulating discussions; the Meteorite Working Group and the staff of the Astromaterials Acquisition and Curation Office at NASA-JSC for samples; Ewa Danielewicz and Abigail Tirrell (Michigan State University Center for Advanced Microscopy) for assistance with the scanning electron microscopy; and Brother Guy Consolmagno, S.J., for helpful and encouraging perspectives on long-term scholarly enterprises. This research was supported by two Michigan Space Grant Consortium Research Seed Grants, a Michigan State University Honors College Honors Research Seminar, and NASA Grant NAG 9-1211. Thoughtful, thorough reviews by Kieren Howard and an anonymous reviewer are greatly appreciated. This paper was written during the first author's tenure as a Smithsonian Senior Fellow at the Division of Meteorites, Department of Mineral Sciences, National Museum of Natural History, Smithsonian Institution. He is most grateful to Cari Corrigan and Ed Vicenzi for hosting the visit, and to his co-hosts, and Glenn MacPherson, Tim McCoy, and Linda Welzenbach, for stimulating conversations.

REFERENCES

Bach, W., Paulick, H., Garrido, C.J., Ildefonse, B., Meurer, W.P., and Humphris, S.E. (2006) Unraveling the sequence of serpentinization reactions: petrography, mineral chemistry, and petrophysics of serpentinites from MAR 15ºN (ODP Leg 209, Site 1274). *Geophysical Research Letters*, **33**, L13306, doi:10.1029/2006GL025681

Barber, D.J. (1981) Matrix phyllosilicates and associated minerals in C2M carbonaceous chondrites. *Geochimica et Cosmochimica Acta*, **45**, 945–970.

Barber, D.J. (1985) Phyllosilicates and other layer-structured materials in stony meteorites. *Clay Minerals* **20**, 415–454.

Bland, P.A., Cressey, G., and Menzies, O.N. (2004) Modal mineralogy of carbonaceous chondrites by X-ray diffraction and Mössbauer spectroscopy. *Meteoritics and Planetary Science*, **39**, 3–16.

Bland, P.A., Jackson, M.D., Coker, R.F., Cohen, B.A., Webber, J.B.W., Lee, M.R., Duffy, C.M., Chater, R.J., Ardakani, M.G., McPhail, D.S., McComb, D.W., and Benedix, G.K. (2009) Why aqueous alteration in asteroids was isochemical: High porosity $\neq$ high permeability. *Earth and Planetary Science Letters*, **287**, 559–568.

Boudier, F., Barronet, A., and Mainprice, D. (2010) Serpentine mineral replacements of natural olivine and their seismic implications: Oceanic lizardite versus subduction-related antigorite. *Journal of Petrology*, **51**, 495–512.

Brantley, S.L. (2005) Reaction kinetics of primary rock-forming minerals under ambient conditions. Pp. 73–117 in: *Surface and Ground Water, Weathering, and Soils* (J.I. Drever, editor). Treatise on Geochemistry Vol. **5** (H.D. Holland and K.K. Turekian, series editors). Elsevier-Pergamon, Oxford, UK.

Brantley, S.L. (2008) Kinetics of mineral dissolution. Pp. 151–210 in: *Kinetics of Water–Rock Interaction* (S.L. Brantley, J.D. Kubicki, and A.F. White, editors). Springer, Berlin.

Brearley, A.J. (2003) Nebular versus parent-body processing. Pp. 247–268 in: *Meteorites, Comets, and Planets* (A.M. Davis, editor). Treatise in Geochemistry Vol. **1** (H.D. Holland and K.K. Turekian, series editors). Elsevier-Pergamon, Oxford, UK.

Brearley, A.J. (2006) The action of water. Pp. 587–624 in: *Meteorites and the Early Solar System II* (D.S. Lauretta and H.Y. McSween, Jr., editors). University of Arizona Press, Arizona, USA.

Browning, L.B., McSween, H.Y., Jr., and Zolensky, M.E. (1996) Correlated alteration effects in CM carbonaceous chondrites. *Geochimica et Cosmochimica Acta*, **60**, 2621–2633.

Browning, L.B., McSween, H.Y., Jr., and Zolensky, M.E. (2000) On the origin of rim textures surrounding anhydrous silicate grains in CM carbonaceous chondrites. *Meteoritics and Planetary Science*, **35**, 1015–1023.

Bunch, T.E. and Chang, S. (1980) Carbonaceous chondrites – II. Carbonaceous chondrite phyllosilicates and light element geochemistry as indicators of parent body processes and surface conditions. *Geochimica et Cosmochimica Acta*, **44**, 1543–1577.

Buseck, P.R. and Hua, X. (1993) Matrices of carbonaceous chondrite meteorites. *Annual Reviews of Earth and Planetary Science*, **21**, 255–305.

Chizmadia, L.J. and Brearley, A.J. (2008) Mineralogy, aqueous alteration, and primitive textural characteristics of fine-grained rims in the Y-791198 CM2 carbonaceous chondrite: TEM observations and comparison to ALHA81002. *Geochimica et Cosmochimica Acta*, **72**, 602–625.

Clayton, R.N. and Mayeda, T.K. (1999) Oxygen isotope studies of carbonaceous chondrites. *Geochimica et Cosmochimica Acta*, **63**, 2089–2104.

Cohen, B.A. and Coker, R.A. (2000) Modeling liquid water on CM meteorite parent bodies and implications for amino acid racemizations. *Icarus*, **145**, 369–381.

Coleman, R.G. (1971) Petrologic and geophysical nature of serpentinites. *Geological Society of America Bulletin*, **82**, 897–918.

Condie, K.C. and Madison, J.A. (1969) Compositional and volume changes accompanying progressive serpentinization of dunites from the Webster-Addie ultramafic body, North Carolina. *American Mineralogist*, **54**, 1173–1179.

Delvigne, J. (1998) *Atlas of Micromorphology of Mineral Alteration and Weathering*. The Canadian Mineralogist, Special Publication **3**, Mineralogical Association of Canada, Ottawa, Ontario, Canada, 495 pp.

Dodd, R.T. (1981) *Meteorites: A Petrologic-Chemical Synthesis*. Cambridge University Press, Cambridge, UK, 368 pp.

DuFresne, E.R. and Anders, E. (1962) On the chemical evolution of the carbonaceous chondrites. *Geochimica et Cosmochimica Acta*, **26**, 1085–1114.

Evans, B.W. (2008) Control of the products of serpentinization by the $Fe^{2+}Mg_{-1}$ exchange potential of olivine and orthopyroxene. *Journal of Petrology*, **49**, 1873–1887. doi:10.1093/petrology/egn050

Frost, B.R. and Beard, J.S. (2007) On silica activity and serpentinization. *Journal of Petrology*, **48**, 1351–1368.

Fuchs, L.H., Olsen, E. and Jensen, K.J. (1973) *Mineralogy, Mineral-Chemistry, and Composition of the Murchison (C2) Meteorite.* Smithsonian Contributions to Earth Science **10**, 39 pp.

Goldich, S.S. (1938) A study in rock weathering. *Journal of Geology*, **46**, 17–58.

Grady, M.M. (2000) *Catalog of Meteorites* (fifth edition). Cambridge University Press, Cambridge, UK, 689 pp.

Graham, R.P.D. (1917) Origin of massive serpentine and chrysotile-asbestos, Black Lake-Thetford area, Quebec. *Economic Geology*, **12**, 154–202.

Greshake, A. (1997) The primitive matrix components of the unique carbonaceous chondrites Acfer 094: A TEM study. *Geochimica et Cosmochimica Acta*, **61**, 437–452

Guo, W. and Eiler, J.M. (2007) Temperatures of aqueous alteration and evidence for methane generation on the parent bodies of CM chondrites. *Geochimica et Cosmochimica Acta*, **71**, 5565–5575.

Hanowski, N.P. and Brearley, A.J. (2001) Aqueous alteration of chondrules in the CM carbonaceous chondrite, Allan Hills 81002: Implications for parent body alteration. *Geochimica et Cosmochimica Acta*, **65**, 495–518.

Hemley, J.J., Montoya, J.W., Christ, C.L., and Hostetler, P.B. (1977) Mineral equilibria in the $MgO-SiO_2-H_2O$ system: I Talc-chrysotile-forsterite-brucite stability relations. *American Journal of Science*, **277**, 322–351.

Hostetler, P.B., Coleman, R.G., and Mumpton F.A. (1966) Brucite in alpine serpentinites. *American Mineralogist*, **51**, 75–98.

Howard, K.T., Benedix, G.K., Bland, P.A., and Cressey, G. (2009) Modal mineralogy of CM2 chondrites by X-ray diffraction (PSD-XRD). Part 1: Total phyllosilicate abundance and the degree of aqueous alteration. *Geochimica et Cosmochimica Acta*, **73**, 4576–4589.

Howard, K.T., Benedix, G.K., Bland, P.A., and Cressey, G. (2011) Modal mineralogy of CM2 chondrites by X-ray diffraction (PSD-XRD). Part 2: Degree, nature and settings of aqueous alteration. *Geochimica et Cosmochimica Acta*, **75**, 2735–2751.

Hutchison, R. (2004) *Meteorites: A Petrologic, Chemical and Isotopic Synthesis*. Cambridge University Press, Cambridge, UK, 506 pp.

Kretz, R. (1983) Symbols for rock-forming minerals. *American Mineralogist*, **68**, 277–279.

Lauretta, D.S., Hua, X., and Buseck, P.R. (2000) Mineralogy of fine-grained rims in the ALH 81002 CM chondrite. *Geochimica et Cosmochimica Acta*, **64**, 3263–3273.

Lee, M.R., Lindgren, P., Sofe, M.R., Alexander, C.M.O'D., and Wang, J. (2012) Extended chronologies of aqueous alteration in the CM2 carbonaceous chondrites: Evidence from carbonates in Queen Alexandra Range 93005. *Geochimica et Cosmochimica Acta*, **92**, 148–169.

Lofgren, G.E. (1989) Dynamic crystallization of chondrule melts of porphyritic olivine composition: Textures: Experimental and natural. *Geochimica et Cosmochimica Acta*, **53**, 461–470.

Lofgren, G.E. (1996) A dynamic crystallization model for chondrule melts. Pp. 187–196 in: *Chondrules and the Protoplanetary Disk* (R.H. Hewins, R.H. Jones, and E.R.D. Scott, editors). Cambridge University Press, Cambridge, UK.

Lofgren, G.E. and Lanier, A.B. (1990) Dynamic crystallization study of barred olivine chondrules. *Geochimica et Cosmochimica Acta*, **54**, 3537–3551.

Lofgren, G.E. and Russell, W.J. (1986) Dynamic crystallization of chondrule melts of porphyritic and radial pyroxene composition. *Geochimica et Cosmochimica Acta*, **50**, 1715–1726.

Mackinnon, I.D.R. and Zolensky, M.E. (1984) Proposed structures for poorly characterized phases in C2M carbonaceous chondrite meteorites. *Nature*, **309**, 240–242.

Martin, B. and Fyfe. W.S. (1970) Some experimental and theoretical observations on the kinetics of hydration reactions with particular reference to serpentinization. *Chemical Geology*, **6**, 185–202.

McSween, H.Y., Jr. (1979a) Are carbonaceous chondrites primitive or processed? A review. *Reviews of Geophysics and Space Physics*, **17**, 1059–1078.

McSween, H.Y., Jr. (1979b) Alteration in CM carbonaceous chondrites inferred from modal and chemical variations in matrix. *Geochimica et Cosmochimica Acta*, **43**, 1761–1770.

McSween, H.Y., Jr. (1987) Aqueous alteration in carbonaceous chondrites: Mass balance constraints on matrix mineralogy. *Geochimica et Cosmochimica Acta*, **51**, 2469–2477.

McSween, H.Y., Jr. and Richardson, S.M. (1977) The composition of carbonaceous chondrite matrix. *Geochimica et Cosmochimica Acta*, **41**, 1145–1161.

Müller, W.F., Kurat, G., and Kracher, A. (1979) Chemical and crystallographic study of cronstedtite in the matrix of the Cochabamba (CM2) carbonaceous chondrite. *Tschermaks Mineralogische und Petrographische Mitteilungen*, **26**, 293–304.

Nahon, D.B. (1991) *Introduction to the Petrology of Soils and Chemical Weathering*. John Wiley and Sons, Inc., New York, 313 pp.

Nakamura, T., Noguchi, T., Okazaki, R., Jogo, K., and Ohtsuka, K. (2008) Mineralogical and stable isotope signatures of El-Quss Abu Said CM2 carbonaceous chondrite: Pristine material from the outer asteroid belt. Abstract, 71st Annual Meteoritical Society Meeting, #5124.

O'Hanley, D.S. (1992) Solution to the volume problem in serpentinization. *Geology*, **20**, 705–708.

O'Hanley, D.S. (1996) *Serpentinites: Records of Tectonic and Petrological History*. Oxford University Press, New York, 277 pp.

Plümper, O., King, H.E., Vollmer, C., Ramasse, Q., Jung, H., and Austrheim, H. (2012) The legacy of crystal-plastic deformation in olivine: High-diffusivity pathways during serpentinization. *Contributions to Mineralogy and Petrology*, **163**, p. 701–724.

Price, J.R., Bryan-Ricketts, D.S., Anderson, D., and Velbel, M.A. (2013) Weathering of almandine garnet: Influence of secondary minerals on the rate-determining step, and implications for regolith-scale Al mobilization. *Clays and Clay Minerals*, **61**, 34–56.

Rosenberg, N.D., Browning, L. and Bourcier, W.L. (2001) Modeling aqueous alteration of CM carbonaceous chondrites. *Meteoritics and Planetary Science*, **36**, 239–244.

Rubin, A.E., Trigo-Rodríguez, J.M., Huber, H., and Wasson, J.T. (2007) Progressive alteration of CM carbonaceous chondrites. *Geochimica et Cosmochimica Acta*, **71**, 2361–2382.

Schulte, M., Blake, D., Hoehler, T., and McCollom, T. (2006) Serpentinization and its implications for life on early Earth and Mars. *Astrobiology*, **6**, 364–376.

Smyth, J.R. and Bish, D.L. (1988) *Crystal Structures and Cation Sites of the Rock-Forming Minerals*. Allen & Unwin, Boston, USA, 332 pp.

Thayer, T.P. (1966) Serpentinization considered as a constant-volume metasomatic process. *American Mineralogist*, **51**, 685–710.

Tomeoka, K., McSween, H.Y., Jr., and Buseck, P.R. (1989) Mineralogical alteration of CM carbonaceous chondrites: A review. *Proceedings of the National Institute of Polar Research Symposium on Antarctic Meteorites* **2**, 221–234.

Velbel, M.A. (1993) Constancy of silicate-mineral weathering-rate ratios between natural and experimental weathering: Implications for hydrologic control of differences in absolute rates. *Chemical Geology*, **105**, 89–99.

Velbel, M.A. and Barker, W.W. (2008) Pyroxene weathering to smectite: Conventional and low-voltage cryo-field emission scanning electron microscopy, Koua Bocca ultramafic complex, Ivory Coast. *Clays and Clay Minerals*, **56**, 111–126.

Velbel, M.A. and Palmer, E.E. (2011) Fine-grained serpentine in CM2 carbonaceous chondrites and its implications for the extent of aqueous alteration on the parent body: A review. *Clays and Clay Minerals*, **59**, 416–432.

Velbel, M.A., Donatelle, A.R., and Formolo, M.J. (2009) Reactant-product textures, volume relations, and implications for major-element mobility during natural weathering of hornblende, Tallulah Falls Formation, Georgia Blue Ridge, U.S.A. *American Journal of Science*, **309**, 661–688.

Velbel, M.A., Tonui, E.K. and Zolensky, M.E. (2012) Replacement of olivine by serpentine in the carbonaceous chondrite Nogoya (CM2). *Geochimica et Cosmochimica Acta*, **87**, 117–135.

Viti, C. and Mellini, M. (1998) Mesh textures and bastites in the Elba retrograde serpentinites. *European Journal of Mineralogy*, **10**, 1341–1359.

Wegner, W.W. and Ernst, W.G. (1983) Experimentally determined hydration and dehydration reaction rates in the system MgO-SiO_2-H_2O. *American Journal of Science*, **283-A**, 151–180.

Wicks, F.J. and Whittaker, E.J.W. (1977) Serpentine textures and serpentinization. *The Canadian Mineralogist*, **15**, 459–488.

Young, E.D., Ash, R.D., England, P., and Rumble, D., III (1999) Fluid flow in chondritic parent bodies: Deciphering the compositions of planetesimals. *Science*, **286**, 1331–1335.

Young, E.D., Zhang, K.K., and Schubert, G. (2003) Conditions for pore water convection within carbonaceous chondrite parent bodies – implications for planetesimal size and heat production. *Earth and Planetary Science Letters*, **213**, 249–259.

Zega, T.J. and Buseck, P.R. (2003) Fine-grained-rim mineralogy of the Cold Bokkeveld CM chondrite. *Geochimica et Cosmochimica Acta*, **67**, 1711–1721.

Zega, T.J., Garvie, L.A.J., Dodony, I., and Buseck, P.R. (2004) Serpentine nanotubes in the Mighei CM chondrite. *Earth and Planetary Science Letters*, **223**, 141–146.

Zega, T.J., Garvie, L.A.J., Dódony, I., Friedrich, H., Stroud, R.M., and Buseck, P.R. (2006) Polyhedral serpentine grains in CM chondrites. *Meteoritics and Planetary Science*, **41**, 681–688.

Zolensky, M. and McSween, H.Y., Jr. (1988) Aqueous alteration. Pp. 114–143 in: *Meteorites and the Early Solar System* (J.F. Kerridge and M. Shapley Matthews, editors). The University of Arizona Press, Arizona, USA.

Zolensky, M.E., Barrett, R., and Browning, L. (1993) Mineralogy and composition of matrix and chondrule rims in carbonaceous chondrites. *Geochimica et Cosmochimica Acta*, **57**, 3123–3148.

Zolensky, M.E., Mittlefehldt, D.W., Lipschutz, M.E., Wang, M.-S., Clayton, R.N., Mayeda, T.K., Grady, M.M., Pillinger, C., and Barber, D. (1997) CM chondrites exhibit the complete petrologic range from type 2 to 1. *Geochimica et Cosmochimica Acta*, **61**, 5099–5115.

(*Received 21 January 2014; revised 20 June 2014; Ms. 845; AE: W. Huff*)

Clays and Clay Minerals, Vol. 62, No. 2, 137–144, 2014.

INVESTIGATION OF THE THERMAL DECOMPOSITION OF TALC

XIAOWEN LIU*, XIAOXU LIU, AND YUEHUA HU
School of Minerals Processing and Bioengineering, Central South University, Changsha 410083, China

Abstract—Different changes in the structural and thermal properties of various types of talc have been reported in the literature which have made comparison of analytical results difficult. The objective of the present study was to obtain some fundamental insights into the effects of the thermal behavior of talc and to carry out kinetic analyses of the decomposition of talc under high temperature. X-ray diffraction (XRD), Fourier-transform infrared spectroscopy (FTIR), and thermogravimetry-differential scanning calorimetry (TG-DSC) were used to study the thermal decomposition mechanism. The Coats-Redfern decomposition model was used to determine the decomposition mechanism of talc samples. The results showed that the decomposition of talc commenced at ~800ºC, peaking at ~895ºC, with the formation of enstatite and amorphous silica. An isothermal treatment at 1000ºC caused the complete dehydroxylation of talc. The XRD and FTIR results indicated that the enstatite and amorphous silica phases were transformed into clinoenstatite and paracrystalline opal phases, respectively, after the decomposition stage at 1200ºC. Good linearity in the Coats-Redfern model was observed from room temperature to 1300ºC and the activation energy was calculated to be 69 kcal/mol.

Key Words—Activation Energy, Coats-Redfern, Thermal Decomposition, Talc.

INTRODUCTION

Talc, $Mg_3Si_4O_{10}(OH)_2$, is used widely in the form of a fine powder in several industrial applications such as ceramics (Ptáček *et al.*, 2014), pharmaceutical (Lee *et al.*, 2010; Akhtar *et al.*, 2012), cosmetics (Agarwal *et al.*, 2011), and papermaking (Yu *et al.*, 2013), and as a filler in talc-polymer composites to enhance nucleation and improve the mechanical properties (Dellisanti *et al.*, 2011). It is the 2:1 trioctahedral ene-member phyllosilicate (Drits *et al.*, 2012; Schumann *et al.*, 2013). Recently, possible changes in the properties of talc during high-temperature calcination have received a great deal of attention because the changes in the physico-chemical, structural, and thermal properties of talc can be exploited in new industrial applications, such as foamed glass (Okada *et al.*, 2009), oil lubricants (Prasad *et al.*, 2010), and electronic substrates for integrated circuits (Gökçe *et al.*, 2011). The influence of mechanical grinding (Christidis *et al.*, 2004; Terada and Yonemochi, 2004; Dellisanti *et al.*, 2009, 2011; Zulumyan *et al.*, 2012) and sonication treatments (Jamil and Palaniandy, 2010; Şener and Özyılmaz, 2010; Jamil and Palaniandy, 2011) on the talc structure have been analyzed extensively. The main effects described in those studies are the progressive structural disorder and subsequent amorphization of the material leading to changes in its physical and thermal properties (Palaniandy and Azizli, 2009; Mahadi and Palaniandy, 2010), and only demonstrate the deformation of talc under relatively low-temperature conditions.

Previous studies have described the decomposition of talc under thermal treatment. The formation of beta magnesium metasilicate was reported at ~600ºC by Avgustinik and Vigdergauz (1948) who also suggested that at 1200ºC silica was dissolved and recrystallized as enstatite. The dehydroxylation temperature was reported by Kedesdy (1943) to be 800ºC, however, with the formation of enstatite only, and protoenstatite formed at 1400ºC. The formation of enstatite, amorphous silica, and water vapor when talc was decomposed at 800−840ºC was noted by Ewell *et al.* (1935). The enstatite changed gradually to protoenstatite at ~1200ºC, and the amorphous silica was converted to cristobalite at ~1300ºC. The dehydroxylation of talc was reported by Ptáček *et al.* (2014) to occur at ~905ºC; enstatite, amorphous silica, and water were formed during this process and cristobalite in particular was stated to originate from the silica phase at 1150ºC. Talc was reported (Dellisanti and Valdrè, 2010) to dehydroxylate in a single step to form $MgSiO_3$ and cristobalite from 1473 to 1600ºC. Comparison of results, however, is difficult because of the various types of dehydroxylation reaction proposed in all these reports.

The objectives of the present study were to obtain insights into the effects of the thermal behavior of talc, to carry out kinetic analysis of its decomposition at high temperatures, and to test the applicability of the Coats-Redfern decomposition model to talc.

EXPERIMENTAL

Materials and methods

Talc was obtained from Guangxi Longguang Talc Development Co. Ltd., China, with chemical compositions listed in Table 1. The talc content was >98 wt.%.

---

* E-mail address of corresponding author:
onlylonely101@126.com
DOI: 10.1346/CCMN.2014.0620206

Table 1. Chemical compositions (mass %) of different samples by XRF.

Samples	SiO_2	MgO	Al_2O_3	Fe_2O_3	CaO
‘Original’ talc	67.68	31.04	0.77	0.50	0.01
200ºC	65.20	33.33	0.47	0.50	0.02
700ºC	65.64	33.36	0.49	0.50	0.02
800ºC	65.66	33.33	0.48	0.52	0.02
900ºC	65.73	33.25	0.50	0.50	0.02
1000ºC	65.70	33.34	0.44	0.50	0.02

After drying at 60ºC, talc was ground into a powder *via* a planetary ball mill to pass through a 0.074 mm sieve and this was labeled as the ‘original’ talc sample. Analysis of the talc sample by scanning electron microscopy (SEM) (Figure 1) revealed the morphology and size of the aggregated particles to be within the 5−30 μm range.

4-g samples of ‘original’ talc were heated in a programmed temperature-controlled muffle furnace at scheduled temperatures (200−1300ºC) for 2.5 h. The heating rate, β, was 10ºC/min. The products were ground into powders using an agate mortar and were given names denoted by the heating temperature (ºC).

Phosphoric-acid digestion was applied to the 1200ºC sample. Orthophosphoric acid (H_3PO_4, 85% mass content; density of 1.71 g cm^{-3}) was supplied by JT Baker Chemical Company (Phillipsburg, New Jersey, USA) − 2 g of the 1200ºC sample was mixed with 100 mL of H_3PO_4 and the mixture heated rapidly to 240ºC and maintained at that temperature for 12 min. After the viscous solution was cooled to 60ºC, it was then diluted with distilled water to 800 mL and filtered. The residue was washed with distilled water to remove the excess PO_4^{3-} ions and dried at room temperature. This phosphoric-acid digestion sample was labeled ‘K0’.

Characterization techniques

X-ray diffraction patterns were obtained using a DX-2700 instrument (Dandong Haoyuan Instrument Co. Ltd., China) with an acceleration voltage of 40 kV and an emission current of 40 mA at a scanning rate of 9º/min from 3 to 80º2θ. Fourier-transform infrared (FTIR) spectra were recorded using a Nicolet 5700 spectrophotometer (Thermo Nicolet, USA). The specimens used for FTIR measurement were prepared by mixing 0.9 mg of sample powder with 80 mg of KBr and pressing the mixture into a pellet. The morphology of the samples was examined by SEM (Sirion 200, FEI, USA). Thermogravimetry-differential scanning calorimetry (TG-DSC) was performed at heating rates, β, of 12ºC/min under N_2 atmosphere (20 cm^3/min) with masses of 10 mg using a Netzch STA449C thermal analyzer (Netzsch, Germany). α-Al_2O_3 was used as an inert material. The chemical compositions of the talc were measured by X-ray fluorescence (XRF, Axios max, PANalytical, Netherlands).

RESULTS AND DISCUSSION

The XRD pattern of the ‘original’ talc sample (Figure 2a) showed that all of the diffraction peaks observed were indexed to the characteristics of talc (JCPDS 19-0770). Over the range 200−700ºC, the locations of most talc peaks changed little. Calcination produced a decrease in the intensity and led to broadening of the diffraction lines; changes in the (001) planes at 9.3º in particular were attributed to a decrease in crystallinity (Yang *et al.*, 2006). The change in crystallinity was used to quantify the progressive structural damage (Aglietti and Potto Lopez, 1992). This index included the background and peak intensities, defining crystallinity as $C = B_0I/(I_0B) \times 100\%$, where C was the crystallinity, B_0 was the background intensity for ‘original’ material, I was the peak intensity for thermally treated material, I_0 was the peak intensity for ‘original’ material, and B was the background intensity for thermally treated material. The corresponding (001) plane crystallinities of the original, 200ºC, 300ºC, 400ºC, 500ºC, 600ºC, and 700ºC talc samples were 100, 63.4, 59.3, 52.7, 47.6, 36.8, and 32.2%, respectively. Moreover, decreasing d values were noted at increasing temperatures from 200 to 700ºC (Table 2), *e.g.*

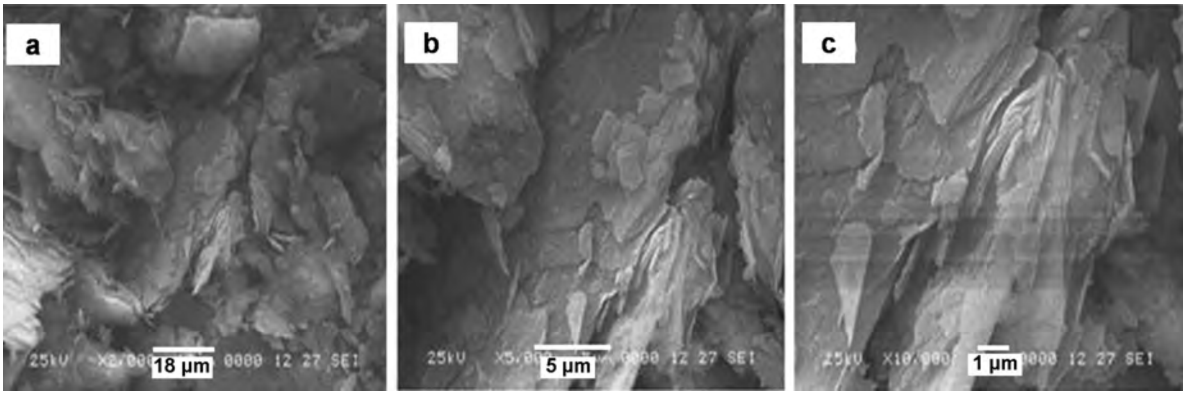

Figure 1. SEM images of the ‘original’ talc sample.

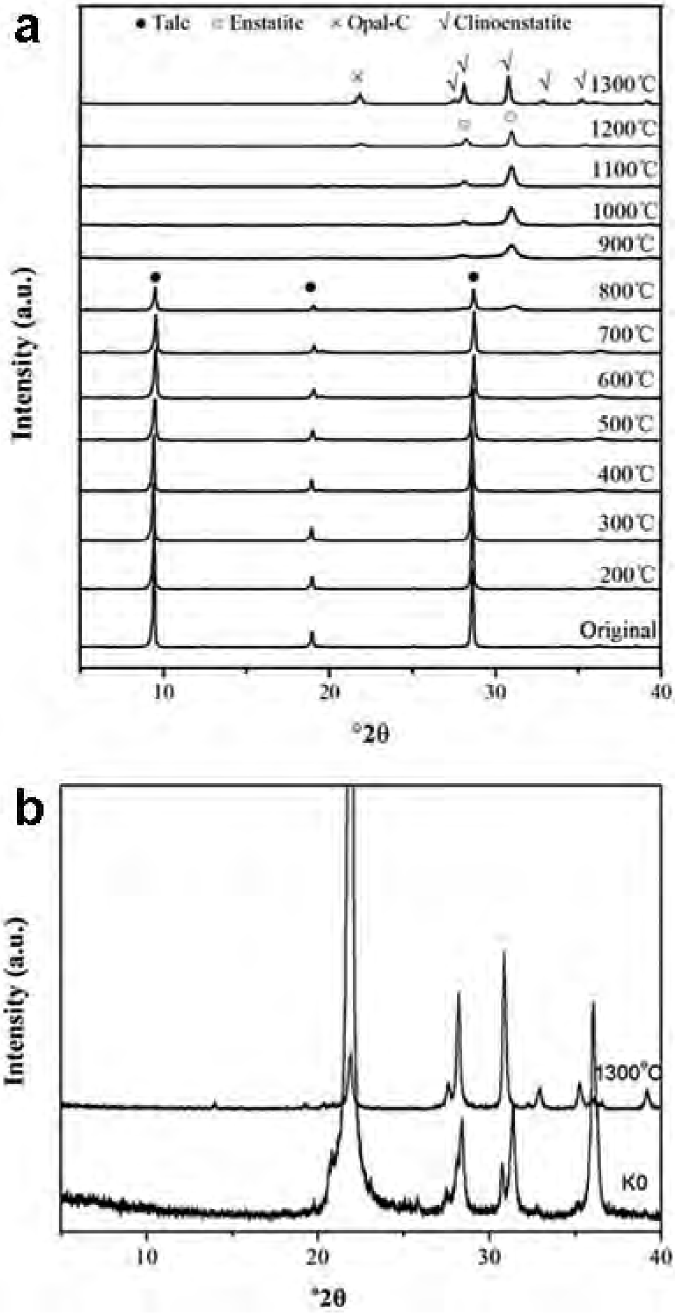

Figure 2. XRD patterns of various samples (a) and of samples at 1300ºC and the K0 sample (b).

d_{001} changed from 0.94 to 0.92 nm and d_{002} from 0.47 to 0.46 nm. Dehydration of talc occurred over the temperature range from 200 to 700ºC.

One new peak was observed at 30.7º2θ in the 800ºC sample, due to enstatite, according to the JCPDS 19-0768 powder diffraction file. The appearance of enstatite indicated that dehydroxylation of talc had begun at 800ºC. The intensity of this new peak increased during and after the dehydroxylation process, especially the (610) plane of enstatite (the intensity of the (610)

Table 2. The basal *d* values of peaks for different samples.

Samples	d_{001} (nm)	d_{002} (nm)	d_{208} (nm)
'Original' talc	0.94	0.47	0.19
200ºC	0.94	0.47	0.19
300ºC	0.94	0.47	0.19
400ºC	0.94	0.47	0.19
500ºC	0.93	0.47	0.19
600ºC	0.92	0.47	0.19
700ºC	0.92	0.47	0.19

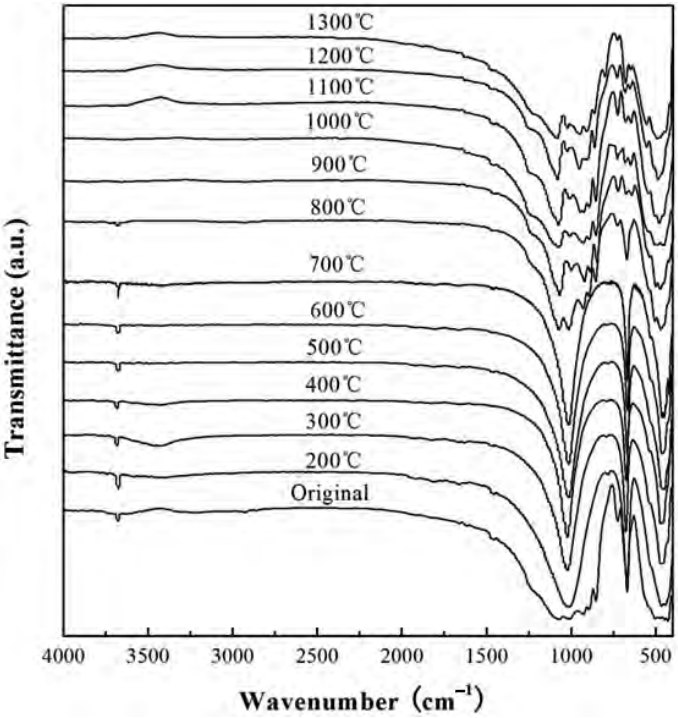

Figure 3. FTIR spectra of various samples.

plane increased from 44 to 530 counts over the temperature range 800 to 1200ºC), which was attributed to the increasing crystallization and crystallite size of enstatite which enlarged from 15.0 to 43.2 nm over that temperature range. As the calcination temperature increased, another new, weak peak occurred at 21.9º2θ in the 1200ºC sample; according to the JCPDS 39-1425 powder diffraction file, this peak is characteristic of paracrystalline opal (Elzea *et al.*, 1994; Sarıkaya *et al.*, 2000; Önal and Sarıkaya, 2007). The corresponding 'K0' sample produced an XRD pattern with the characteristic paracrystalline opal (opal-C) peak, d_{101} = 0.41 nm. After heating at 1050ºC for 24 h, the full width at half-maximum (FWHM) of the 101 reflection was unchanged, shifted from 21.9 to 21.8º2θ, and intensified by a factor of at least two (Figure 2b), clearly indicating that opal-C had been formed (Önal *et al.*, 2007). The enstatite phase was transformed to clinoenstatite in the 1300ºC sample. The peak at 30.7º2θ shifted to 31.7º2θ and a new peak at 27.5º2θ appeared, characteristic of clinoenstatite according to JCPDS 35-0610.

The FTIR spectra of talc samples at different calcination temperatures (Figure 3) revealed that the increasing temperature had a great effect on the structure of talc (detailed assignments of each band shown in Table 3). The 'original' talc sample possessed obvious signals as reported by Mollah *et al.* (1999) and Castillo *et al.* (2013), such as 428 (Si−O), 465 (Si−O−Si), and 671 cm^{-1} (Si−O−Mg). As the temperature increased from 200 to 700ºC, the Si−O−Si stretching vibration shifted from 1013 to 1019 cm^{-1} with the progressive intensity caused by the dehydration of talc (Jamil and

Table 3. The assignments of bands for different samples.

Vibrational frequency (cm^{-1})	Assignment
3678	Stretching vibration of Mg−OH
~3429−3474	OH-stretching vibration of absorbed water
~1635−1654	OH-bending vibration of absorbed water
~1017−1094	Stretching vibration of Si−O−Si
671	Stretching vibration of Si−O−Mg
~465−472	Bending vibration of Si−O−Si
428	Stretching vibration of Si−O

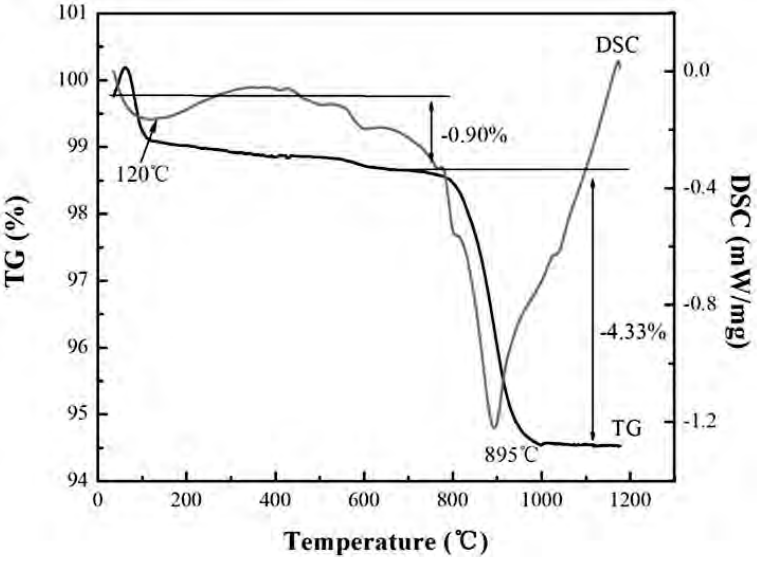

Figure 4. TG-DSC curves of the 'original' talc sample.

Palaniandy, 2011). Compared to the 700ºC sample, the IR spectrum of the 800ºC sample displayed two weaker bands at 672 and 1016 cm^{-1} and they originated from the stretching vibrations of Si−O−Mg (Jamil and Palaniandy, 2011) and Si−O−Si, respectively (Dellisanti *et al.*, 2009). The decreasing intensity of these two bands was attributed to the dehydroxylation of talc at 800ºC. The new peaks at 1072, 929, 895, 855, 727, and 505 cm^{-1} were assigned to enstatite in accordance with previous studies (Goel *et al.*, 2009) and indicated that enstatite had been generated at 800ºC as shown by the XRD results. The intensity of the asymmetrical stretching vibration of Si−O−Si at 1072 cm^{-1} increased as the temperature increased from 800 to 1300ºC and the position shifted from 1072 to 1076 cm^{-1}, possibly related to changes in the molecular structure of enstatite after heating at temperatures in excess of 800ºC (Goel *et al.*, 2009). Moreover, an indication of the formation of amorphous silica was observed in the 800ºC sample by the new absorption bands at ~895 and ~929 cm^{-1}, which were consistent with a transparent silica window (~860−960 cm^{-1}) (Inaki *et al.*, 2002). The intensity of bands at 895 and 928 cm^{-1} increased from 800 to 1200ºC, and then decreased at 1300ºC. The Mg−OH stretching vibration band at 3678 cm^{-1} weakened gradually from 200 to 1000ºC and disappeared after 1000ºC, indicating that dehydroxylation of talc is completed after heating to 1000ºC. The transformation of amorphous silica to opal-C occurred from 1200 to 1300ºC as the band at 794 cm^{-1}, attributed to opal-C, appeared at 1300ºC (Mollah *et al.*, 1999).

The TG-DSC curves of 'original' talc samples (Figure 4) showed that a small weight loss of ~0.9% at 120ºC was due to the loss of absorbed water (Dellisanti and Valdrè, 2010; Wang and Karato, 2013). In the TG curves of talc, a significant weight loss occurred over the temperature range from 800 to 1000ºC with a broad endothermic DSC signal peak at 894ºC related to the dehydroxylation of talc (equation 1), consistent with previous results of dehydroxylation of talc from 800 to 1000ºC (Smykatz-Kloss, 1974; Ward, 1975; Paterson and Swaffield, 1987; Okada *et al.*, 2009). Enstatite, amorphous silica, and water were formed during this process and the total weight loss was ~4.3%. The diffraction lines of enstatite appeared on the XRD plot in this temperature range. Opal-C ($SiO_2 \cdot nH_2O$) originated from the silica phase at 1200ºC. The following reaction may take place at high temperature:

$$2Mg_3Si_4O_{10}(OH)_2 \rightarrow 3Mg_2(Si_2O_6)\text{ (enstatite)} + 2SiO_2\text{ (amorphous)} + 2H_2O(g) \quad (1)$$

$$Mg_2(Si_2O_6)\text{ (enstatite)} + SiO_2\text{(amorphous)} + nH_2O(g) \rightarrow Mg_2(Si_2O_6)\text{ (clinoenstatite)} + SiO_2 \cdot nH_2O\text{ (opal-C)} \quad (2)$$

The reaction temperatures of equations 1 and 2 were ~800 and 1200ºC, respectively, in accordance with the results obtained by Wesolowski (1984), who reported that the decomposition of talc was accompanied by the formation of enstatite and amorphous silica. The inversion of enstatite to clinoenstatite took place gradually, both phases being observed in the material heated at 1200ºC. The presence of clinoenstatite alone had been detected at temperatures as high as 1300 to 1435ºC.

All kinetic studies envisage one of two methods: differential or integral. All the methods are based on the kinetic equation (Tang *et al.*, 2003):

$$d\alpha/dt = k(1-\alpha)^n = A\exp(-E/RT)(1-\alpha)^n \quad (3)$$

Table 4. Relation between the transformation rate (α) of talc samples and the reaction temperature (*T*).

β (K·min^{-1})	*T* (K)										
	α = 0%	α = 10%	α = 20%	α = 30%	α = 40%	α = 50%	α = 60%	α = 70%	α = 80%	α = 90%	α = 100%
12	1065	1102	1122	1138	1150	1160	1171	1181	1195	1214	1408

where $d\alpha/dt$ was the decomposition rate; n, the degree of the decomposition reaction; A, the frequency factor; E, the activation energy of the decomposition; T, the absolute temperature; R, the gas constant; α, the transformation rate; and k, the decomposition rate constant.

The integral method approach to the kinetic study was more convenient, reliable, and accurate than the differential method (Tang *et al.*, 2003). In the present investigation, therefore, the Coats-Redfern method, an integral approach, was followed to investigate the decomposition kinetics of talc. The Coats-Redfern method is based on the equation (Qin *et al.*, 2005):

$$\ln[g(\alpha)/T^2] = \ln[AR(1-2RT/E)/\beta E] - E/RT \qquad (4)$$

where $g(\alpha) = -\ln(1-\alpha)$, for $n = 1$; $g(\alpha) = [1-(1-\alpha)^{1-n}]/(1-n)$, for $n \neq 1$. Different n values were substituted into equation 4 and $\ln[g(\alpha)/T^2]$ was plotted *vs.* $1/T$. The n value that gave the best fit (maximum correlation coefficient) was taken as the reaction order (Qin *et al.*, 2005). The Coats-Redfern method has been used successfully to analyze the decomposition of ammonium pentaborate (Şahin *et al.*, 2001), poly(ethylene terephthalate)/clay nanocomposites (Xu *et al.*, 2010), and $BaCO_3$ (Maitra and Bandyopadhyay, 2008). The decomposition of talc was a typical example of a solid-state reaction. The reaction followed first-order kinetics. In order to confirm the mechanism function, the data for the relation between the transformation rate of the talc samples (α) and reaction temperature (*T*) were used in the Coats-Redfern-method calculations. The variation in α as a function of temperature is shown in Table 4.

By making some mathematical approximations to the above equation and taking its integral, the following Coats-Redfern equation for $n = 1$ was obtained.

$$\ln[-\ln(1-\alpha)/T^2] = \ln[AR(1-2RT/E)/\beta E] - E/RT \qquad (5)$$

The slope of the plot of $\ln[-\ln(1-\alpha)/T^2]$ *vs.* $1/T$ yields $-E/R$, meaning that if the plot is linear the activation energy can be calculated. The graph of $\ln[-\ln(1-\alpha)/T^2]$ *vs.* $1/T$ (Figure 5) indicates good linearity, suggesting it as a suitable model for this process. The value of E was calculated to be 69 kcal/mol.

CONCLUSIONS

TG-DSC was used to investigate the thermal decomposition process of talc at constant heating rate under an N_2 atmosphere; data from XRD and FTIR analyses were used to confirm this determination. Talc transformed to enstatite after heating to 800ºC and the dehydroxylation peak temperature was ~895ºC. After 1000ºC, talc dehydroxylated completely. The XRD and FTIR results indicated that the enstatite and amorphous silica phases were transformed to clinoenstatite and opal-C phases, respectively, after dehydroxylation at 1200ºC. The

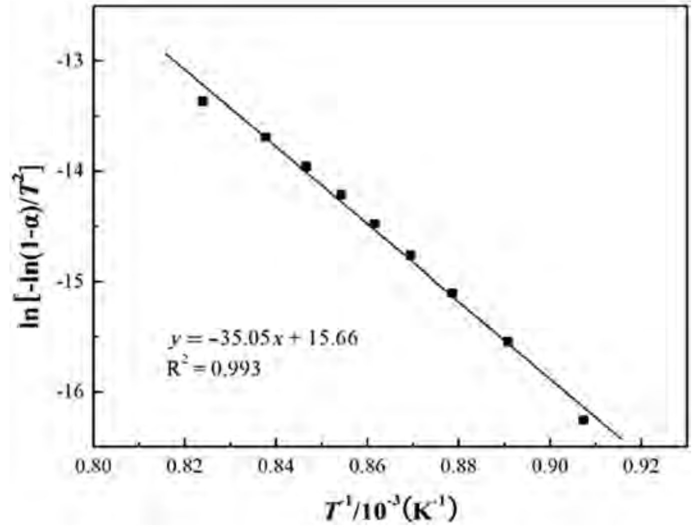

Figure 5. Calculation of the activation energy of talc samples using the Coats-Redfern integral method.

reaction kinetics model of talc decomposition in a solid-state reaction was researched based on a chosen mechanism function – the Coats-Redfern method. The mechanism of talc decomposition was confirmed and the activation energy was calculated to be 69 kcal/mol.

ACKNOWLEDGMENTS

The present study was supported by the National Twelfth Five-year Science and Technology Support Program (2012BAB10B00) and the China Scholarship Council (CSC).

REFERENCES

Agarwal, R., Paul, A.S., Aggarwal, A.N., Gupta, D., and Jindal, S.K. (2011) A randomized controlled trial of the efficacy of cosmetic talc compared with iodopovidone for chemical pleurodesis. *Respirology*, **16**, 1064–1069.

Aglietti, E.F. and Potto Lopez, J.M. (1992) Physicochemical and thermal properties of mechanochemically activated talc. *Materials Research Bulletin*, **27**, 1205–1216.

Akhtar, M.J., Ahamed, M., Khan, M.A.M., Alrokayan, S.A., Ahmad, I., and Kumar, S. (2012) Cytotoxicity and apoptosis induction by nanoscale talc particles from two different geographical regions in human lung epithelial cells. *Environmental Toxicology*, doi:10.1002/tox.21766.

Avgustinik, A.I. and Vigdergauz, V.S. (1948) Properties of talc during heating. *Ogneupory*, **13**, 218–227

Castillo, L., López, O., López, C., Zaritzky, N., García, M.A., Barbosa, S., and Villar, M. (2013) Thermoplastic starch films reinforced with talc nanoparticles. *Carbohydrate Polymers*, **95**, 664–674.

Christidis, G.E., Makri, P., and Perdikatsis, V. (2004) Influence of grinding on the structure and colour properties of talc, bentonite and calcite white fillers. *Clay Minerals*, **39**, 163–175.

Dellisanti, F. and Valdrè, G. (2010) On the high-temperature structural behaviour of talc ($Mg_3Si_4O_{10}(OH)_2$) to 1600ºC: effect of mechanical deformation and strain. *Philosophical Magazine*, **90**, 2443–2457.

Dellisanti, F., Valdrè, G., and Mondonico, M. (2009) Changes of the main physical and technological properties of talc due to mechanical strain. *Applied Clay Science*, **42**, 398–404.

Dellisanti, F., Minguzzi, V., and Valdrè, G. (2011) Mechanical and thermal properties of a nanopowder talc compound produced by controlled ball milling. *Journal of Nanoparticle Research*, **13**, 5919–5926.

Dritis, V.A., Guggenheim, S., Zviagina, B.B., and Kogure, T. (2012) Structures of the 2:1 layers of pyrophyllite and talc. *Clays and Clay Minerals*, **60**, 574–587.

Elzea, J.M., Odom, I.E., and Miles, W.J. (1994) Distinguishing well ordered opal-CT and opal-C from high temperature cristobalite by X-ray diffraction. *Analytica Chimica Acta*, **286**, 107–116.

Ewell, R.H., Bunting, E.N., and Geller, R.F. (1935) Thermal decomposition of talc. *Journal of Research of the National Bureau of Standards*, **15**, 551–556.

Goel, A., Tulyaganov, D.U., Shaaban, E.R., Knee, C.S., Eriksson, S., and Ferreira, J.M.F. (2009) Structure and crystallization behaviour of some $MgSiO_3$-based glasses. *Ceramics International*, **35**, 1529–1538.

Gökçe, H., Ağaoğulları, D., Öveçoğlu, M.L., Dumana, İ., and Boyraz, T. (2011) Characterization of microstructural and thermal properties of steatite/cordierite ceramics prepared by using natural raw materials. *Journal of the European Ceramic Society*, **31**, 2741–2747.

Inaki, Y., Yoshida, H., Yoshida, T., and Hattori, T. (2002) Active sites on mesoporous and amorphous silica materials and their photocatalytic activity: an investigation by FTIR, ESR, VUV-UV and photoluminescence spectroscopies. *Journal of Physical Chemistry B*, **106**, 9098–9106.

Jamil, N.H. and Palaniandy, S. (2010) Acid medium sonication: A method for the preparation of low density talc nanosheets. *Powder Technology*, **200**, 87–90.

Jamil, N.H. and Palaniandy, S. (2011) Comparative study of water-based and acid-based sonications on structural changes of talc. *Applied Clay Science*, **51**, 399–406.

Kedesdy, H. (1943) Electron-microscope investigation of firing of talc and soapstone. *Berichte der Deutschen Keramischen Gesellschaft*, **24**, 201–232.

Lee, P., Sun, L., Lim, C.K., Aw, S.E., and Colt, H.G. (2010) Selective apoptosis of lung cancer cells with talc. *European Respiratory Journal*, **35**, 450–452.

Mahadi, M.I. and Palaniandy, S. (2010) Mechanochemical effect of dolomitic talc during fine grinding process in mortar grinder. *International Journal of Mineral Processing*, **94**, 172–179.

Maitra, S. and Bandyopadhyay, N. (2008) Application of non-Arrhenius method for analyzing the decomposition kinetics of $SrCO_3$ and $BaCO_3$. *Journal of the American Ceramic Society*, **91**, 337–341.

Mollah, M.Y.A., Promreuk, S., Schennach, R., Cocke, D.L., and Güler, R. (1999) Cristobalite formation from thermal treatment of Texas lignite fly ash. *Fuel*, **78**, 1277–1282.

Okada, K., Ikawa, F., Isobe, T., Kameshima, Y., and Nakajima, A. (2009) Low temperature preparation and machinability of porous ceramics from talc and foamed glass particles. *Journal of the European Ceramic Society*, **29**, 1047–1052.

Önal, M. and Sarıkaya, Y. (2007) The effect of heat treatment on the paracrystallinity of an opal-CT found in a bentonite. *Journal of Non-Crystalline Solids*, **353**, 4195–4198.

Önal, M., Kahraman, S., and Sarıkaya, Y. (2007) Differentiation of α-cristobalite from opals in bentonites from Turkey. *Applied Clay Science*, **35**, 25–30.

Palaniandy, S. and Azizli, K.A.M. (2009) Mechanochemical effects on talc during fine grinding process in a jet mill. *International Journal of Mineral Processing*, **92**, 22–33.

Paterson, E. and Swaffield, R. (1987) Thermal analysis. Pp. 99–132 in: *A Handbook of Determinative Methods in Clay Mineralogy* (M.J. Wilson, editor). Chapman & Hall, London.

Prasad, B.K., Rathod, S., Modi, O.P., and Yadav, M.S. (2010) Influence of talc concentration in oil lubricant on the wear response of a bronze journal bearing. *Wear*, **269**, 498–505.

Ptáček, P., Lang, K., Šoukal, F., Opravil, T., Bartoníčková, E., and Tvrdík, L. (2014) Preparation and properties of enstatite ceramic foam from talc. *Journal of the European Ceramic Society*, **34**, 515–522.

Qin, H.L., Zhang, S.M., Zhao, C.G., and Yang, M.S. (2005) Zero-order kinetics of the thermal degradation of polypropylene/clay nanocomposites. *Journal of Polymer Science Part B: Polymer Physics*, **43**, 3713–3719.

Şahin, Ö., Özdemir, M., Aslanolu, M., and Beker, Ü.G. (2001) Calcination kinetics of ammonium pentaborate using the Coats-Redfern and genetic algorithm method by thermal analysis. *Industrial and Engineering Chemistry Research*, **40**, 1465–1470.

Sarıkaya, Y., Önal, M., Baran, B., and Alemdaroğlu, T. (2000) The effect of thermal treatment on some of the physicochemical properties of a bentonite. *Clays and Clay Minerals*, **48**, 557–562.

Schumann, D., Hartman, H., Eberl, D.D., Sears, S.K., Hesse, R., and Vali, H. (2013) The influence of oxalate-promoted growth of saponite and talc crystals on rectorite: testing the intercalation-synthesis hypothesis of 2:1 layer silicates. *Clays and Clay Minerals*, **61**, 342–360.

Şener, S. and Özyılmaz, A. (2010) Adsorption of naphthalene onto sonicated talc from aqueous solutions. *Ultrasonics Sonochemistry*, **17**, 932–938.

Smykatz-Kloss, W. (1974) *Differential Thermal Analysis, Application and Results in Mineralogy*. Springer, Berlin.

Tang, W.J., Liu, Y.W., Zhang, H., and Wang, C.X. (2003) New approximate formula for Arrhenius temperature integral. *Thermochimica Acta*, **408**, 39–43.

Terada, K. and Yonemochi, E. (2004) Physicochemical properties and surface free energy of ground talc. *Solid State Ionics*, **172**, 459–462.

Wang, D.J. and Karato, S.-i. (2013) Electrical conductivity of talc aggregates at 0.5 GPa: influence of dehydration. *Physics and Chemistry of Minerals*, **40**, 11–17.

Ward, J.R. (1975) Kinetics of talc dehydroxylation. *Thermochimica Acta*, **13**, 7–14.

Wesolowski, M. (1984) Thermal decomposition of talc: a review. *Thermochimica Acta*, **78**, 395–421.

Xu, X.F., Ding, Y.F., Wang, F., Wen, B., Zhang, J.H., Zhang, S.M., and Yang, M.S. (2010) Effects of silane grafting on the morphology and thermal stability of poly(ethylene terephthalate)/clay nanocomposites. *Polymer Composites*, **31**, 825–834.

Yang, H.M., Du, C.F., Hu, Y.H., Jin, S.M., Yang, W.G., Tang, A.D., and Avvakumov, E.G. (2006) Preparation of porous material from talc by mechanochemical treatment and subsequent leaching. *Applied Clay Science*, **31**, 290–297.

Yu, Y., Xue, G., Gu, C., Lou, J., and Li, S. (2013) Preparation of chitosan modified talc and its application in high filler content paper. *Journal of Applied Polymer Science*, **129**, 2692–2698.

Zulumyan, N.H., Papakhchyan, L.R., Isahakyan, A.R., Beglaryan, H.A., and Aloyan, S.G. (2012) The influence of mechanical treatment on the silicate network of talc. *Russian Journal of Physical Chemistry A*, **86**, 1008–1013.

(*Received 24 December 2013; revised 21 April 2014; Ms. 831; AE: S. Kadir*)

Clays and Clay Minerals, Vol. 62, No. 2, 145–152, 2014.

STABILITY OF IRON IN CLAYS UNDER DIFFERENT LEACHING CONDITIONS

Barbora Dousova[1,*], Lucie Fuitova[1], David Kolousek[1], Miloslav Lhotka[1], Tomas Matys Grygar[2], and Petra Spurna[1]

[1] Institute of Chemical Technology in Prague, Technicka 5, 166 28 Prague 6, Czech Republic
[2] Institute of Inorganic Chemistry AS CR, 250 68 Řež, Czech Republic

Abstract—The iron chemistry of aluminosilicates can markedly affect their adsorption properties due to possible changes in surface charge upon exposure to a variety of processes in the environment. One of these processes is chemical leaching, but to date little has been reported on the susceptibility of structural Fe to chemical leaching. The purpose of the current study was to determine the effects of solution pH on the stability of structural Fe in kaolinites, illite, and bentonite and the potential for formation of ancillary (oxyhydr)oxides. Structurally bound Fe does not participate in sorption properties but Fe that is released and phase transformed during leaching could take part in adsorption processes and form complexes and/or covalent bonds *via* Fe ions. Five different Fe-bearing clay minerals were treated in 0.5 M and 2 M HCl, distilled H_2O, 0.1 M KCl, and 0.5 M $KHCO_3$ for 24 h. The amount of Fe leached varied from 10 $\mu g\ g^{-1}$ (for 0.1 M KCl) to 10^4 $\mu g\ g^{-1}$ (for 2 M HCl) depending on the leaching agents. Acidic and water treatments indicated a relative independence of leached Fe on the initial Fe content in the clay and, conversely, a heavy dependence on the crystallinity of initial Fe phases. Well crystallized Fe(III) was stable during the leaching process, while poorly crystallized and amorphous Fe(III) phases were less stable, forming new ion-exchangeable Fe^{3+} particles. Under alkaline conditions, no relation between Fe crystallinity and mobility was found. The structural and surface changes resulting from leaching processes were identified by equilibrium adsorption isotherms. In kaolinite, the specific surface area (S_{BET}) and porosity changed independently of Fe leaching due to the stability and crystallinity of Fe. In bentonite, the number of micropores was reduced by their partial saturation with Fe^{3+} particles caused by poorly crystallized and more reactive Fe forms during the leaching process. Potential phase transformations of Fe were characterized by the voltammetry of microparticles; well crystallized Fe(III) oxides remained stable under leaching conditions, while poorly crystallized and amorphous Fe(III) phases were partially dissolved and transformed to reactive Fe^{3+} forms.

Key Words—Clays, Iron, Leaching Stability, Structure, Surface Properties.

INTRODUCTION

Iron chemistry controls most surface and subsurface geochemical processes due to the variability of Fe species, their widespread occurrence, pH/Eh sensitivity, and, initially, a high sorption affinity in the solid−liquid interface. Iron cations in the two main structural groups of clay minerals mostly occupy the octahedral sheets (Stucki *et al*., 1988); their form and oxidation states vary according to the mineralogical and environmental conditions. In kaolinites, most Fe is present in the structure; some has been identified as the Fe(II) form (Bonin *et al*., 1982, Hassan and Salem, 2002). Free oxides and hydroxides have also been recognized as discrete particles or as coatings bound to the particle surface, typically at the rate of ~0.5 g of Fe_2O_3/kg of kaolin (Ferris and Jepson, 1975). Most 2:1 clay minerals contain some structural iron in the octahedral sheets, both in the Fe(II) and Fe(III) forms (Stucki *et. al*., 1988). Structural Fe provides a significantly greater binding stability than surface Fe phases (Ferris and Jepson, 1975). The equilibrium between Fe^{3+} and Fe^{2+} particles in layer silicates can be considered responsible for important physical-chemical properties of these materials (Favre *et al*., 2006; Komadel *et al*., 2006; Manceau *et al*., 2000).

The chemical and/or bacterial reduction of structural Fe also modifies some properties (Pentráková *et al*., 2013), including the layer charge and the cation exchange capacity (CEC), which are closely related to adsorption/desorption processes on the surface. In natural environments, especially in soils, structural Fe in clay minerals and Fe (oxyhydr)oxides (usually denoted as HFO) coexist (Favre *et al*., 2006) and can be present as individual particles; most commonly, they form stable organomineral species or HFO-coated particles. Though the presence of Fe (oxyhydr)oxides in relation to clay minerals can contribute significantly to their sorption properties, little evidence of the transformation of structurally bound Fe to a surface-coating of hydrated Fe^{3+} particles has been found (Sei *et al*., 2002).

Over the past ten years, surface modification of aluminosilicates with Fe ions has opened up new possibilities in adsorption technologies due to the change in the surface charge (pH_{ZPC}) of aluminosilicates and, thus, a strong affinity for anionic contaminants (Doušová *et al*., 2009; Izumi *et al*., 2005). Through the

* E-mail address of corresponding author:
Barbora.Dousova@vscht.cz
DOI: 10.1346/CCMN.2014.0620207

interaction of raw clay mineral and Fe-salt solution, reactive ion-exchangeable forms of amorphous and/or poorly crystalline HFO particles in a stable oxidation state, Fe(III), are fixed on the clay-mineral surface forming active adsorption sites. The considerable variability in growing Fe phases (hydrated Fe_2O_3, non-specific Fe^{3+} particles, ferrihydrite) resulted from the different types of minerals and the treatment conditions (Doušová *et al.*, 2009). According to Burleson and Penn (2006), most of the newly created active sites can subsequently be fixed in surface complexes during adsorption processes, while unoccupied sites tend to be transformed to more stable and/or crystalline mineral Fe phases (*e.g.* goethite).

The above-described processes also take place in the natural environment (Dávila-Jiménez, 2008). Even dissolved Fe ions can participate *in situ* in adsorption/desorption processes; during co-adsorption, hydrated Fe particles are bound preferentially to active sites due to their excellent sorption affinity for clay mineral surfaces. Reactive Fe(II/III) particles form new active sorption sites which mostly attract anionic particles from aqueous systems (Doušová *et al.*, 2011; Yang *et al.*, 2007).

Generally, a surface-fixed and/or structurally bound Fe affects the surface properties of clay minerals (adsorption/desorption, transformation of particles to more or less stable forms, and mobility of surface-fixed particles, depending on pH/Eh changes). The main aim of the present study was, therefore, to determine the stability of Fe in selected types of clay minerals under various chemical leaching conditions; specifically, to measure the effects of changes in structural Fe content on the clay-mineral structure and crystallinity and to correlate such changes with the initial iron content and the leaching agent used.

MATERIALS AND METHODS

Clays with large bound-Fe contents

Five different types of Fe-rich clays were studied: kaolinite from Király Hill in Hungary (KH); illite from an illite pit in Tokai, Hungary (IH); smectite known as 'Red Clay' from a lignite pit in Visonta, Hungary (RCH); kaolinite from a clay deposit in West Bohemia, Czech Republic (KCR); and bentonite with a large smectite content from a bentonite pit in West Bohemia, Czech Republic (BCR). These materials were washed with distilled water, dried at 60ºC, homogenized using a mortar and pestle, and finally sieved to 0.355 mm.

The main chemical and mineralogical characteristics of the clays used are summarized in Table 1.

Leaching agents

For leaching experiments, five different solutions or leaching agents were used: (*a*) 0.5 M HCl (pH = 1.1), (*b*) 2.0 M HCl (pH = 0.7), (*c*) 0.1 M KCl (pH = 6.3), (*d*) 0.5 M $KHCO_3$ (pH = 8.3), and (*e*) H_2O (pH = 5.6). The solutions were prepared from chemicals of analytical-reagent grade (Merck, Penta, Czech Republic) and distilled water at ambient temperature (25ºC).

Leaching procedure

Experiments were run in a batch manner at a solid:liquid ratio of 1:10, laboratory temperature (20ºC), and leaching times of 1 h, 2 h, 5 h, 8 h, and 24 h. The leaching products were separated by filtration; the filtrate was analyzed for residual Fe content, while the solid part was tested using the methods described below (S_{BET} and pore distribution, voltammetry of microparticles).

Analytical methods

The concentration of Fe_{tot} in aqueous solutions was measured with a UV/VIS spectrophotometer (UNICAM 5625, Richmond Scientific, Ltd., Lancashire, UK) using the Fe^{3+} chelate complex method (with EDTA) at 520 nm (Malat, 1973).

The amount of Fe(II) present in the clay minerals was determined by the manganometric titration method (Alvarez Querol, 1952); 200 mg of solid sample was exposed to a mixture of acids (10 mL of 10% H_2SO_4 and 5% H_3PO_4), distilled water (30 mL), and $(NH_4)_2SO_4$ (100 mg) under an inert atmosphere (N_2) for 20 min. The

Table 1. Mineralogical and chemical properties of the clays used in the present study.

Sample	Fe_{tot} (mg g^{-1})	Fe^{2+} (mg g^{-1})	Mineralogical composition	Fe crystallinity*
KH	21.3	10.4	kaolinite, quartz, pyroxene	Very high (~90%)
IH	12.2	1.0	illite, quartz, goethite	High (>60%)
RCH	48.0	6.4	montmorillonite, quartz, kaolinite, hematite	Low (~20%)
KCR	62.4	12.5	montmorillonite, illite, kaolinite, quartz	Moderate (50%)
BCR	106.4	1.3	montmorillonite, kaolinite, quartz, K-feldspar	Moderate (~30%) nanocrystals

KH: kaolinite from Király Hill, Hungary; IH: illite from a pit in Tokai, Hungary; RCH: smectite known as 'Red Clay' from a lignite pit in Visonta, Hungary; KCR: kaolinite from a clay deposit in west Bohemia, Czech Republic; BCR: bentonite with a large smectite content from a bentonite pit in west Bohemia, Czech Republic.

* determined by Mössbauer spectroscopy

suspension was titrated quickly with 0.02 M $KMnO_4$ to the end point, as given by reaction 1.

$$MnO_4^- + 8\ H^+ + 5e^- \rightarrow Mn^{2+} + 4\ H_2O \qquad (1)$$

X-ray diffraction (XRD) of powder samples was done using a Seifert XRD 3000P diffractometer (Seifert, Ahrensburg, Germany) with CoKα radiation (λ = 0.179026 nm, graphite monochromator, goniometer with Bragg-Brentano geometry) over the range 5–60°2θ, step size 0.05°2θ.

X-ray fluorescence (XRF) analyses of the solid phase were done using an ARL 9400 XP+ spectrometer (ARL, Ecublens, Switzerland); voltage 20–60 kV, probe current 40–80 mA; effective area 490.6 mm^2. *UniQuant* software was used to evaluate the data (Thermo ARL, Switzerland).

Transmission ^{57}Fe Mössbauer spectra were collected in constant acceleration mode using a $^{57}Co(Rh)$ source (1.85 GBq). Powdered samples were prepared as conventional absorbers (~5 mg Fe cm^{-2}) and measured at room temperature and 25 K. The isomer shift (δ) was calibrated against an α-Fe foil at room temperature. Spectra were folded and fitted by Lorentz functions using the program *CONFIT2000* (Žák and Jirásková, 2006). The proportions of Fe phases were determined from the integral area of absorption subspectra.

Equilibrium adsorption isotherms of nitrogen were measured at 77 K using a static volumetric adsorption system (ASAP 2020 analyzer, Micromeritics, Norcross, USA), using samples leached for 24 h. The adsorption isotherms were fitted using the Brunauer-Emmett-Teller (BET) method for specific surface area (Brunauer *et.al.*, 1938), the micropore volume by the t-plot method (Webb and Orr, 1997), and the pore-size distribution by the Barrett-Joyner-Halenda (BJH) method (Barrett *et al.*, 1951).

Voltammetry of microparticles was performed using a conventional paraffin-impregnated graphite electrode in a 1:1 acetate buffer with total acetate concentration of 0.2 M in linear sweep mode from open circuit potential in the negative direction at a scan rate of 3 mV/s (Grygar *et al.*, 2002). The potentials are given with respect to a saturated calomel reference electrode (SCE) and interpreted through comparison with the peak potentials, E_p, of reference oxides (Grygar *et al.*, 2002), free Fe^{3+} ions, and oligomeric Fe(III) hydroxo-oxide species (Grygar *et al.*, 2007).

The parameters of Fe leaching were calculated according to first- and second-order kinetics (Sultana *et al.*, 2014). The reproducibility of leaching experiments was checked by parallel measurements; the standard deviation, which resulted from 10 experimental sets, did not exceed 7%.

RESULTS AND DISCUSSION

Stability of Fe under different leaching conditions

The rate and extent of dissolution of clay minerals is generally influenced by the mineral type, layer structure, and chemical composition (Madejová *et al.*, 2009). The reactions governing leaching in acid or water were, respectively:

$$Fe_2O_3 + 6\ HCl \rightarrow 2\ Fe^{3+} + 6\ Cl^- + 3\ H_2O \qquad (2)$$

$$Fe_2O_3 + 15\ H_2O \rightarrow 2\ [Fe(H_2O)_6]^{3+} + 6\ OH^- \qquad (3)$$

The maximum amount of Fe (μg g^{-1}) leached from the samples in different environments at equilibrium are given in Table 2. Measurements of the release of Fe (Figure 1) revealed that the amount of Fe leached varied from ~10 μg for 0.1 M KCl to ~10^4 μg for 2 M HCl (Table 2).

Kinetics data (Table 3) for acidic leaching of BCR and KCR, which have the largest amounts of total Fe and moderate Fe crystallinity (see Table 1), were evaluated in light of reaction 2, which depended on the concentration of hydrogen ions according to a first-order rate equation. At increasing concentration of hydrogen ions, the rate of reaction increased. In the case of water leaching (reaction 3), second-order kinetics was involved because of a complex reaction mechanism with hydrolyzed products which resulted in a significantly slower reaction rate.

Regardless of the total Fe content, the stability of structural Fe in the clay minerals decreased in the following order for the respective leaching agents (*a*–*e*; Table 2):

acidic, *a*,*b*: KH > IH > KCR > RCH > BCR
water, *e*: KH > IH ≈ RCH > KCR > BCR
alkaline, *d*: KCR ≈ RCH > KH > BCR
greater ionic strength, *c*: KH ≈ IH > BCR > RCH > KCR

Table 2. Fe released from the clay minerals (μg g^{-1}) and the corresponding percentage decline in structural Fe_{tot} (%).

Sample	0.5 M HCl (*a*)	%	2 M HCl (*b*)	%	0.5 M $KHCO_3$ (*d*)	%	H_2O (*e*)	%	0.1 M KCl (*c*)	%
KH	156	0.7	986	4.6	29.2	0.1	17.8	0.08	17.7	0.1
IH	161	1.3	647	5.3			61.2	0.5	18.34	0.2
RCH	3085	6.4	7499	15.6	20.8	0.04	50.0	0.1	29.9	0.1
KCR	1731	2.8	5221	8.4	22.3	0.03	100.1	0.2	39.6	0.1
BCR	7500	7.1	23476	22.1	33.3	0.03	200.0	0.2	20.0	0.02

Sample names as in Table 1.

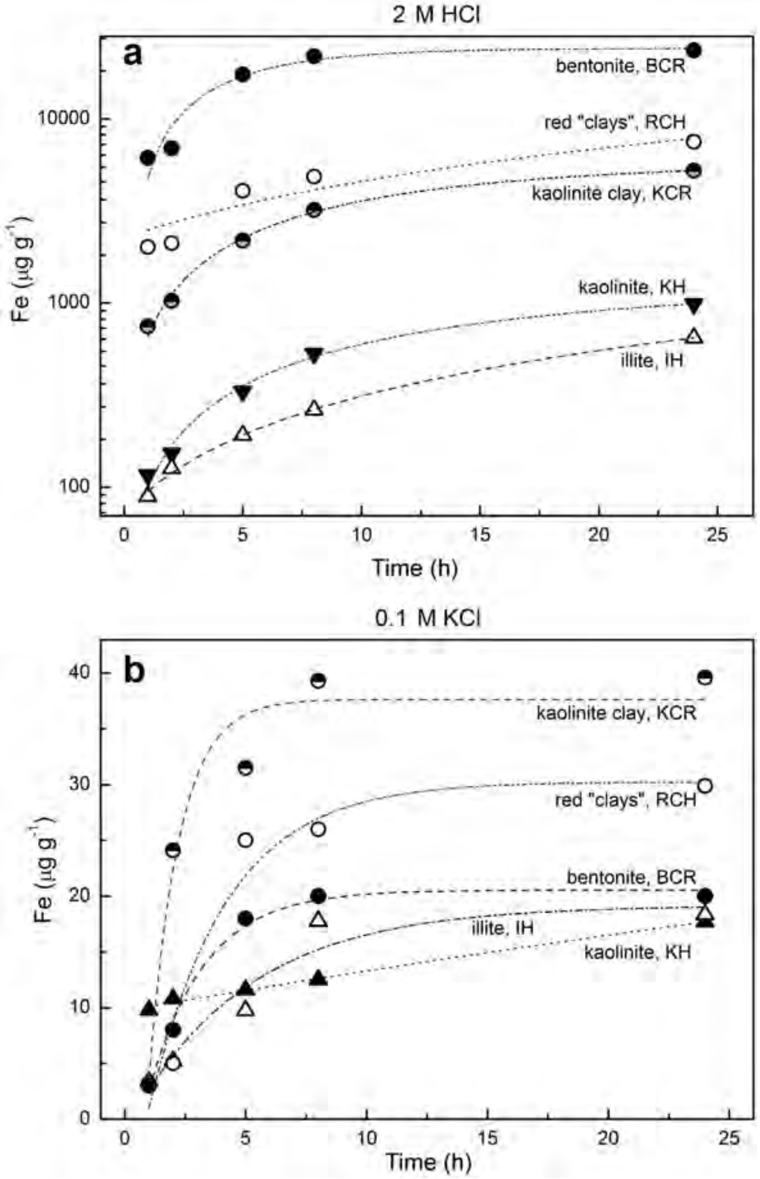

Figure 1. Time dependence of Fe release from clays during leaching processes: (a) 2 M HCl, (b) 0.1 M KCl.

Table 3. Kinetic data for acidic and water leaching.

	Kaolinite clay, KCR				Bentonite, BCR			
Leaching agent	Order	R^2	k^1 (h^{-1})	k^2 (g µg^{-1} h^{-1})	Reaction order	R^2	k^1 (h^{-1})	k^2 (g µg^{-1} h^{-1})
0.5 M HCl (1)	1st	0.995	0.046	–	1st	0.987	0.049	–
2 M HCl (2)	1st	0.992	0.114	–	1st	0.987	0.344	–
H_2O (5)	2nd	0.964	–	2.7	2nd	0.999	–	2.2

k^1 – rate constant for 1st order reaction
k^2 – rate constant for 2nd order reaction

Except for alkaline leaching, the results indicated uniform trends in Fe stability; they proved the relative independence of Fe stability from the total Fe in initial samples, in contrast to strong dependence on the crystallinity of separate (oxyhydr)oxide Fe phases. Well crystallized phases (in KH and IH) were stable in acidic and water ionic and non-ionic environments, as evidenced by the different amounts of Fe released (see Table 2). Under alkaline conditions, no relation between Fe crystallinity and dissolution was found because of the stability of structural Fe(III) in alkaline solution, with possible destruction of Al and Si bonds in the clay mineral structure.

Structural changes in leached clays

The structural and surface changes of clay minerals that occurred during the leaching process were determined *via* equilibrium adsorption isotherms, thereby allowing description of appropriate fluctuations in porosity and specific surface area. The adsorption isotherms of well crystallized kaolinite (KH) and moderately crystallized bentonite (BCR) were measured before and after acidic and water leaching. The characteristic curves of pore-volume distribution obtained by the BJH method to nitrogen at 77 K (Figure 2), and the total porosity and S_{BET} (Table 4),

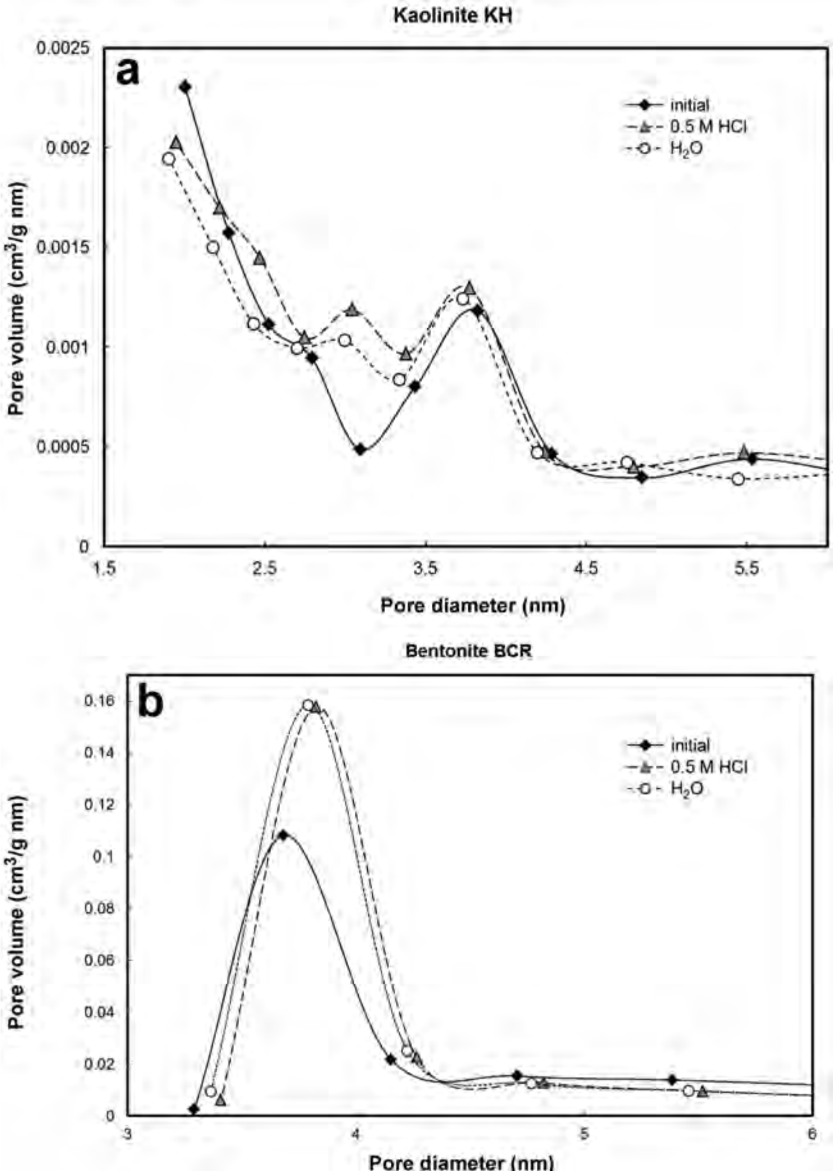

Figure 2. BJH pore-volume distribution of kaolinite KH (a) and bentonite BCR (b), leached for 24 h.

Table 4. Specific surface area and pore volume of initial and leached clay-mineral samples.

Sample	— Surface area, S_{BET} (m^2 g^{-1}) — Initial	0.5 M HCl	H_2O dist.	— Micropore volume $V_{\mathrm{t\text{-}plot}}$ (cm^3 g^{-1}) — Initial	0.5 M HCl	H_2O dist.
Kaolinite, KH	5.59	6.69 (+19.7%)*	5.50 (−1.6%)	0.013	0.015 (+15.4%)	0.013 (±0%)
Bentonite, BCR	82.35	93.57 (+13.6%)	90.23 (+9.6%)	0.115	0.114 (–0.9%)	0.111 (−3.5%)

* relative difference from initial value

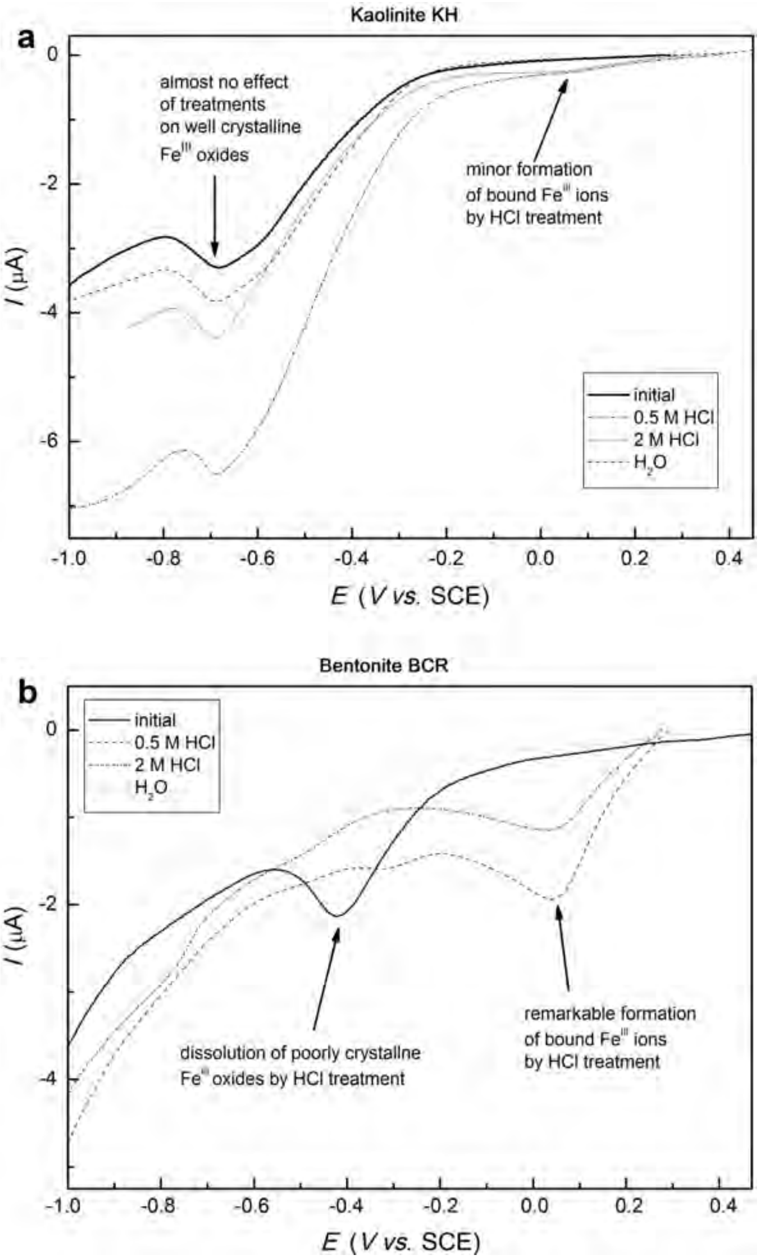

Figure 3. Voltammetric curves of kaolinite KH (a) and bentonite BCR (b) before and after acidic and aqueous leaching.

indicated that the bentonite has a relatively homogeneous pore structure, with the prevalent pore diameter being ~4 nm, whereas kaolinite pore space is more heterogeneous and of smaller diameters. The porosity in the bentonite is also larger than in the kaolinite. The variations in S_{BET} and pore volume observed during the leaching processes were not statistically significant, but indicated a direct correlation between the crystallinity and stability of Fe phases, leaching agent, and clay mineral type. The acidic leaching of kaolinite resulted in an apparent increase in S_{BET} and total micro-porosity, which denoted the formation of additional porosity at lower pore diameters (Figure 2a) (Lhotka *et al.*, 2012). The greater porosity and surface area after acidic leaching were probably caused by partial destruction of the kaolinite structure in the acidic environment. The distribution of porosity after neutral leaching of KH and BCR followed the acidic process (Figure 2a,b), but the data in Table 4 illustrate some changes compared to the acidic leaching. Water leaching did not modify the kaolinite structure. A greater mobility of Fe in bentonite (Table 2) resulted in a decline in micro-porosity due to the partial saturation of micropores with activated Fe^{3+} particles which were generated during the leaching process (Gil and Adamski, 2010).

Phase transformation of Fe due to the leaching process

Evaluation of equilibrium adsorption isotherms revealed changes in micro-porosity and surface area; voltammetry of microparticles can identify Fe phases in the clay structure, and give their oxidation state and phase transformations during the leaching process. This method was applied for quick and simple characterization of different HFO phases in clay minerals, alloys, and archeological objects (Cepriá *et al.*, 2003; Doménech *et al.*, 2013; Grygar *et al.*, 2002). As discussed above, kaolinite (KH) and bentonite (BCR) were chosen for comparison of their Fe characteristics *via* a voltammetric method. The voltammograms (Figure 3) showed possible variations in Fe phases during acidic and water leaching. According to Grygar *et al.* (2002) and van Oorschot *et al.* (2001), who identified small concentrations of Fe oxides in minerals, the peak at ~−0.75 V in Figure 3a can be assigned to well crystallized Fe(III) oxides in KH. This phase did not change markedly under the acidic leaching, but a partial chemical dissolution and phase transformation of Fe(III) microparticles may be indicated by the peaks at ~0 V (Figure 3a) (Cepriá *et al.*, 2003), which denoted the formation of reactive Fe^{3+} particles. Poorly crystallized Fe(III) oxides in BCR, which are characterized by the peak potential of −0.50 V (Figure 3b) (Cepriá *et al.*, 2003; Grygar *et al.*, 2002), were dissolved by acidic leaching. The process resulted in the remarkable formation of reactive Fe^{3+} particles as indicated by the prominent peaks at ~0.10 V. A similar run of initial and H_2O voltammetric curves (Figures 3a, 3b) illustrated minor changes in Fe forms by water leaching. These results correspond well with those of Maqueda *et al.* (2008), who examined the behavior of Fe phases in untreated and acid-treated vermiculite. That study showed visible structural changes and a very small proportion of leached Fe in 0.25 M HCl.

CONCLUSIONS

The stability and phase transformations of structural Fe in clay minerals were mostly affected by the crystallinity of Fe particles. The total Fe and mineralogical characterization of clays were less important in leaching processes. Well crystallized Fe phases (60−90% of crystallinity) in kaolinite and illite were more stable in acidic, water ionic, and non-ionic environments compared to poorly crystallized Fe forms (20% to <50 % of crystalline Fe) in bentonite, kaolinite clay, and smectite clays (‘red clays’). No relation between Fe crystallinity and mobility was observed under alkaline leaching due to Fe(III) stability in alkaline conditions. Micro-porosity and surface parameters related to leaching processes were affected markedly by the crystallinity of Fe particles; the changes in S_{BET}/pore volume in material with highly crystallized Fe related to a partial structural disturbance in acidic environment and were slightly affected by Fe changes. Materials containing less stable and poorly crystallized Fe forms demonstrated the participation of Fe released in the surface structure by the saturation of micropores with activated Fe^{3+} particles. Well crystallized Fe(III) oxides maintained their original structures with almost no effect by the leaching process. Poorly crystallized and amorphous Fe(III) phases were partially dissolved and transformed to much more mobile, ion-exchangeable Fe^{3+} ions forming active binding sites. The iron chemistry and phase transformation in clays influence their surface changes and adsorption properties.

ACKNOWLEDGMENTS

The authors acknowledge funding for the present study as part of project no. 13-24155S from the Grant Agency of the Czech Republic.

REFERENCES

Alvarez Querol, M.C. (1952) Manganometric microtitration of iron. *Microchimica Acta*, **39(2)**, 126−132.

Barret, E.P., Joyer, L.G., and Halenda, P.P. (1951) The determination of pore volume and area distributions in porous substances. I. Computations from nitrogen isotherms. *Journal of the American Chemical Society*, **73**, 373−380.

Bonnin, D., Miller, S., and Calas, G. (1982) Iron in kaolins: studies by EPR, Mössbauer, X-ray absorption, EXAFS. *Bulletin de Mineralogie*, **105**, 467−475.

Brunauer, S., Emmet, P.H., and Teller, F. (1938) Adsorption of gases in multimolecular layers. *Journal of the American Chemical Society*, **60**, 309−319.

Burleson, D.J. and Penn, R.L. (2006) Two-step growth of goethite from ferrihydrite. *Langmuir*, **22**, 402−409.

Cepriá, G., Usón, A., Pérez-Arantegui, J., and Castillo, J.R. (2003) Identification of iron(III) oxides and hydroxy-oxides by voltammetry of immobilised microparticles. *Analytica Chimica Acta*, **477**, 157−168.

Dávila-Jiménez, M.M., Elizade-González, M.P., Mattusch, J., Morgenstern, P., Pérez-Cruz, M.A., Reyes-Ortega, Y., Wennrich, R., and Hee-Madeira, H. (2008) In situ and ex situ study of the enhanced modification with iron of clinoptilolite-rich zeolitic tuff for arsenic sorption from aqueous solutions. *Journal of Colloid and Interface Science*, **322**, 527−536.

Doménech, A., Lastras, M., Rodrígues, F., and Osete, L. (2013) Mapping of corrosion products of highly altered archeological iron using voltammetry of microparticles. *Microchemical Journal*, **106**, 41−50.

Doušová, B., Fuitová, L., Grygar, T., Machovič, V., Koloušek, D., Herzogová, L., and Lhotka, M. (2009) Modified aluminosilicates as low-cost sorbents of As(III) from anoxic groundwater. *Journal of Hazardous. Materials*, **165**, 134−140.

Doušová, B., Lhotka, M., Grygar, T., Machovič, V., and Herzogová, L. (2011) In situ co-adsorption of arsenic and iron/manganese ions on raw clays. *Applied Clay Science*, **54**, 166−171.

Favre, F., Bogdal, C., Gavillet, S., and Stucki, J.W. (2006) Changes in the CEC of a soil smectite-kaolinite clay fraction as induced by structural iron reduction and iron coatings dissolution. *Applied Clay Science*, **34**, 95−104.

Ferris, A.P. and Jepson, W.B. (1975) The exchange capacities of kaolinite and the preparation of homoionic clays. *Journal of Colloid and Interface Science*, **51**, 245−259.

Gil, B. and Adamski, A. (2010) Complementary use of IR and EPR spectroscopies for characterization of iron species in thermally treated MFI-type zeolites. *Microporous and Mesoporous Materials*, **127**, 82−89.

Grygar, T., Bezdička, P., Hradil, D., Doménech-Carbó, A., Marken, F., Pikna, L., and Cepriá, G. (2002) Voltammetric analysis of iron oxide pigments. *Analyst*, **127**, 1100.

Grygar, T., Hradil, D., Bezdička, P., Doušová, B., Čapek, L., and Schneeweiss, O. (2007) Fe(III) modified montmorillonite and bentonite: Synthesis, chemical and UV-VIS spectral characterization, arsenic sorption, and catalysis of oxidative dehydrogenation of propane. *Clays and Clay Minerals*, **55**, 165−176.

Hassan, M.S. and Salem, S.M. (2002) Distribution and influence of iron phases on the physico-chemical properties of phyllosilicates. *Chinese Journal of Geochemistry*, **21**, 29−39.

Izumi, Y., Masih, D., Aika, K., and Seida, Y. (2005) Characterization of intercalated iron(III) nanoparticles and oxidative adsorption of arsenite on them monitored by X-ray absorption fine structure combined with fluorescence spectrometry. *The Journal of Physical Chemistry B*, **109**, 3227−3232.

Komadel, P., Madejová, J., and Stucki, J.W. (2006) Structural Fe(III) reduction in smectites. *Applied Clay Science*, **34**, 88−94.

Lhotka, M., Machovič, V., and Doušová, B. (2012) Preparation of modified sorbents from rehydrated clay minerals. *Clay Minerals*, **47**, 251−258.

Malat, M. (1973) *Absorption Inorganic Photometry*. Academia, Prague (in Czech), pp. 684−709.

Madejová, J., Pentrák, M., Pálková, H., and Komadel, P. (2009) Near-infrared spectroscopy: A powerful tool in studies of acid-treated clay minerals. *Vibrational Spectroscopy*, **49**, 211−218.

Manceau, A., Drits, V.A., Lanson, B., Chateigner, D., Wu, J., Huo, D., Gates, W.P., and Stucki, J.W. (2000) Oxidation-reduction mechanism of iron in dioctahedral smectites: 2. Crystal chemistry of reduced Garfield nontronite. *American Mineralogist*, **85**, 153−172.

Maqueda, C., Santas Romero, A., Morillo, E., Pérez-Rodríguez, J.L., Lerf, A., and Wagner, F.E. (2008) The behavior of Fe in ground and acid-treated vermiculite from Santa Olalla, Spain. *Clays and Clay Minerals*, **56**, 380−388.

Pentráková, L., Su, K., Pentrák, M., and Stucki, W. (2013) A review of microbial redox interactions with structural Fe in clay minerals. *Clay Minerals*, **48**, 543−560.

Sei, J., Jumas, J.C., Olivier-Fourcade, J., Quiquampoix, H., and Staunton, S. (2002) Role of iron oxides in the phosphate adsorption properties of kaolinites from the Ivory Coast. *Clays and Clay Minerals*, **50**, 217−222.

Stucki, J.W., Goodman, B.A., and Schwertmann, U. (1988) *Iron in Soils and Clay Minerals*, pp. 447−480, 625−642. D. Riedel Publishing Company, Dordrecht, The Netherlands.

Sultana, U.K., Gulshan, F., and Kurny, A.S.W. (2014) Kinetics of leaching of iron oxide in clay in oxalic acid and hydrochloric acid solutions. *Materials Science and Metallurgy Engineering*, 2, 5−10.

van Oorschot, I.H.M., Grygar, T., and Dekkers, M.J. (2001) Detection of low concentrations of fine-grained iron oxides by voltammetry of microparticles. *Earth and Planetary Science Letters*, **193**, 631−642.

Webb, P.A. and Orr, C. (1997) *Analytical Methods in Fine Particle Technology*. Micromeritics Instrument Corporation, Norcross, Georgia, USA.

Yang, L., Donahoe, R.J., and Redwine, J.C. (2007) *In situ* chemical fixation of arsenic contaminated soils: An experimental study. *Science of the Total Environment*, **387**, 28−41.

Žák, T. and Jirásková, Y. (2006) CONFIT: Mössbauer spectra fitting program. *Surface and Interface Analysis*, **38**, 710−714.

(*Received 2 January 2014; revised 26 May 2014; Ms. 832; AE: J. Miehé-Brendlé*)

Clays and Clay Minerals, Vol. 62, No. 2, 153–160, 2014.

FIRST PRINCIPLES *AB INITIO* STUDY OF CO_2 ADSORPTION ON THE KAOLINITE (001) SURFACE

MAN-CHAO HE, JIAN ZHAO*, AND YANG LI

State Key Laboratory for Geomechanics and Deep Underground Engineering, China University of Mining and Technology, Beijing 100083, China

Abstract—The capture and storage of carbon dioxide (CO_2) have considerable potential for mitigating climate change. Adsorption is one of the most popular methods for the storage of CO_2. The adsorption of CO_2 molecules on the hydroxylated (001) surface of kaolinite was investigated using density-functional theory within the generalized gradient approximation and a supercell approach. The coverage dependence of the adsorption structures and energetics was studied systematically for a wide range of coverage, Θ [from 0.11 to 1.0 monolayers (ML)], and adsorption sites. The CO_2 was adsorbed on the two-fold bridge-x (see the text for a definition) and the one-fold top-x sites in the bent, recumbent configuration, and on the three-fold hollow-z, two-fold bridge-z site, and the one-fold top-z sites in the vertical configuration. The surface-adsorbed binding site of CO_2 was strongest at the bridge-x site and weakest at the top-z site. The adsorption energy increased with coverage, thus indicating the greater stability of surface adsorption and a tendency to form CO_2 islands (clusters) with increasing coverage. The other properties of the CO_2/kaolinite (001) system, including the different charge distribution, the lattice relaxation, and the electronic density of states, were also studied and are discussed in detail.

Key Words—Adsorption, Carbon Dioxide, First-principles Calculations, Kaolinite.

INTRODUCTION

The control of greenhouse gases is arguably the most challenging environmental policy issue facing the world today. Carbon dioxide is considered to be the major greenhouse gas (GHG) (He *et al.*, 2012). The average concentration of CO_2 in the atmosphere has increased significantly from 280 ppm (parts per million) in about 1850 to 379 ppm in 2005 and as a result, the average global temperature has increased by 0.6−1ºC during this period (Li *et al.*, 2013). The technology of CO_2 capture and storage (CCS) can provide a medium-term solution to mitigate environmental impacts (Kaya, 1995; Li *et al.*, 2013; Luis *et al.*, 2012; Aspelund and Jordal, 2007; Waldo, 2011). The technology of CCS usually consists of three parts: CO_2 capture, transport, and storage. Capture and storage have, by far, been the two most studied parts of the CCS chain, because transport has been considered to be the least technically challenging. As a result, many investigators have studied experimentally the storage of CO_2 using chemical and physical treatments. Adsorption is one of the most popular methods for the storage of CO_2 (Araki *et al.*, 2012; Lopez-Carreno *et al.*, 1997; Choe *et al.*, 2001; Do and Do, 2006; Baltrusaitis *et al.*, 2011; Smykowski *et al.*, 2013; Wood *et al.*, 2012). Natural clay minerals, in particular, have received much attention as a possible low-cost adsorbent in the storage of CO_2 taken from contaminated air. A number of studies concerning clay minerals used to store CO_2 have been reported (Volzone, 2007; Venaruzzo *et al.*, 2002; Xu *et al.*, 2005; Ketzer *et al.*, 2009). Due to the limitations of the experimental methods used, a theoretical analysis of the adsorption mechanism of CO_2 monomers on natural clay minerals from a microscopic point of view will improve understanding of the adsorptive properties of the clay mineral−CO_2 interface and the influence of CO_2 adsorbed on the structure of clay minerals. Computer simulation based on density-functional theory (DFT) has proven a powerful and reliable tool in the study of CO_2−solid interfaces at the molecular level. Kaolinite is one of the most abundant clay minerals and so a greater insight into the adsorption of CO_2 molecules on kaolinite surfaces through detailed first-principles analysis is needed.

Existing experimental (Adams, 1983; Benco *et al.*, 2001; Bish, 1993) and theoretical (Hayashi, 1997; Hess and Saunders, 1992; Hobbs *et al.*, 1997; Plançon and Giese, 1997; Teppen, *et al.*, 1997; Hu and Angelos, 2008) data for the kaolinite $Al_2Si_2O_5(OH)_4$ surface are often rationalized by modeling two surfaces as almost perfect 1:1 layer structures consisting of two different aluminosilicate surfaces. One side consists of a gibbsite-type sheet where Al ions are coordinated octahedrally by oxygen ions and hydroxyl groups; the other side of the layer consists of a silica sheet in which Si ions are coordinated tetrahedrally by oxygen ions only. Quantitative estimates indicate that gibbsite-sheet OH groups and adjoining silica-sheet O atoms in kaolinite have a certain degree of van der Waals attraction and hydrogen bonding (Sato *et al.*, 2005). While the silica-

---

* E-mail address of corresponding author:
zhaojian0209@aliyun.com
DOI: 10.1346/CCMN.2014.0620208

sheet side is saturated and hydrophobic, the hydroxyl at the Al (oxyhydr)oxide side is hydrophilic. Kaolinite microparticles exist as hexagonal plates with a dominant (001) basal surface with almost perfect cleavage; this is the plane mainly exposed in kaolinite crystals (Šolc *et al.*, 2011; Giese, 1973). The kaolinite (001) hydroxyl surface is of primary interest in adsorption studies. The objectives here were to investigate CO_2 adsorption sites, adsorption energies, charge transfer, CO_2 structure during adsorption, and the structure of the intermediate reaction complex.

METHODS

Calculations were performed using the local-density approximation (LDA) as implemented in the Vienna *ab initio* simulation package (VASP) (Kress and Furthmüller, 1996). Projector augmented wave (PAW) pseudopotentials (Blöchl, 1994; Kress and Joubert, 1999) and plane waves were used. The energy cutoff for the plane-wave basis was 400 eV, which was sufficient to ensure errors of <0.01 eV in the calculated values for adsorption energies and activation barriers. The so-called ‘repeated slab’ geometries were applied. The kaolinite (001) surface was modeled using a slab composed of six atomic layers and a vacuum region of 20 Å, which was found to be sufficiently convergent. During the calculations, all the H, O, and Al atoms in the outermost three layers (octahedral Al oxide surface), as well as the CO_2 molecules, were allowed to relax while the other three atomic layers (including the middle O and H atoms, the bottom silica, and the O atoms) of the slab were kept fixed at the calculated bulk positions. Unless otherwise mentioned, a $(3 \times 3 \times 1)$ *k*-point grid for the *p* (2×2) and *p* (3×3) surface cell with a Monkhorst-Pack (Monkhorst and Pack, 1976) scheme was used. A Fermi broadening of 0.02 eV/Å was chosen to smear the occupation of the bands around E_F by a finite-T Fermi function and extrapolating to $T = 0$ K. In the present study, calculations for adsorbed CO_2 molecules at surface coverages that ranged from 0.11 to 1.0 ML were performed for 12 adsorption sites (Figure 1). The 12 adsorption sites included three one-fold top sites (T_1–T_3), three two-fold bridge sites (B_1–B_3), and six three-fold hollow sites (H_1–H_6). The CO_2 coverages of 0.11, 0.33, 0.44, 0.67, 0.89, and 1.0 ML were calculated using the *p* (3×3) surface unit cell, while coverages of 0.25, 0.5, and 0.75 ML were calculated for the *p* (2×2) surface cell. The calculated lattice parameters of bulk kaolinite a = 5.155 Å, b = 5.155 Å, c = 7.405 Å, α = 75.14°, β = 84.12°, and γ = 60.18° were used throughout the study (Hess and Saunders, 1992).

RESULTS

One important quantity, E_{ads}, tailored for the present study, is the average adsorption energy of the CO_2 molecules on the kaolinite substrate, defined as:

$$E_{ads}(\Theta) = -\frac{1}{N_{CO_2}}\left[E_{CO_2/\mathrm{kaolinite}(001)} - E_{\mathrm{kaolinite}(001)} - N_{CO_2}E_{CO_2}\right] \quad (1)$$

Here N_{CO_2} is the total number of CO_2 molecules present in the supercell at the coverage Θ considered (Θ is defined as the ratio of the number of molecules

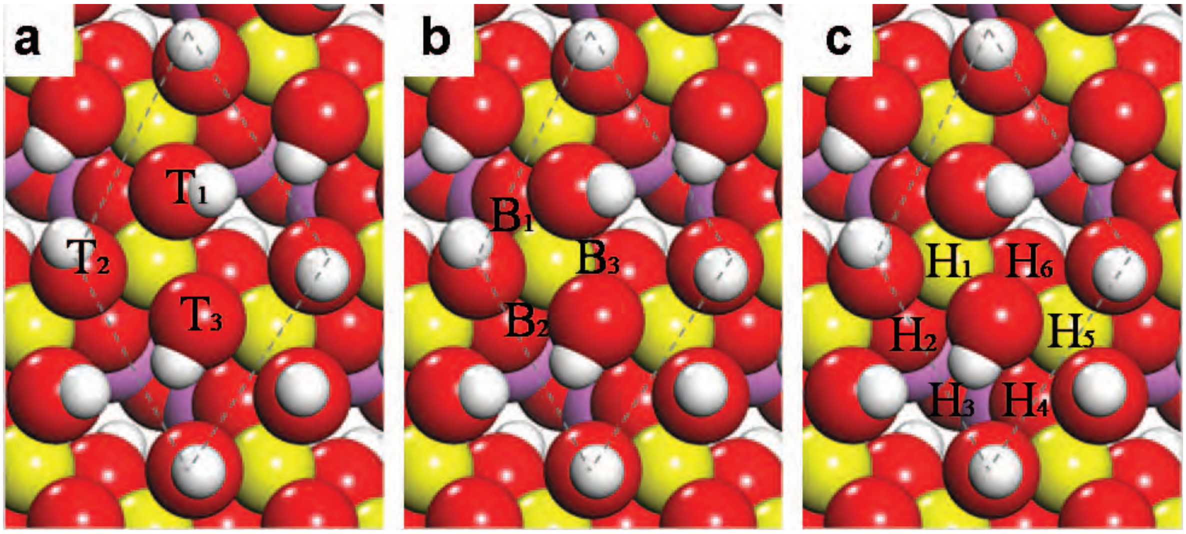

Figure 1. Top view of the kaolinite (001) surface with (a) three top adsorption sites (T_1–T_3), (b) three bridge adsorption sites (B_1–B_3), and (c) six hollow adsorption sites (H_1–H_6). White spheres = hydrogen; red spheres = oxygen; yellow spheres = aluminum; and purple spheres = silicon.

adsorbed to the number of molecules in an ideal substrate layer). The $E_{CO_2/\mathrm{kaolinite}\ (001)}$, $E_{\mathrm{kaolinite}\ (001)}$, and E_{CO_2} are the total energies of the slabs containing CO_2, of the corresponding clean kaolinite surface, and of a free CO_2 molecule, respectively. According to this definition, a positive value of E_{ads} indicates that the adsorption is exothermic (stable) with respect to a free CO_2 molecule and a negative value indicates an endothermic (unstable) reaction. The adsorbed CO_2 coverage was $0<\Theta\leqslant 1.0$. All of the three kinds of high-symmetry adsorption sites on the (001) surface were considered (Hu and Angelos, 2008). The x, y, and z were used to differentiate O−C−O orientations. As shown in Figure 1, 36 kinds of adsorption sites for CO_2 molecules on the kaolinite (001) surface were considered. By employing the notation used in Figure 1, the sites as top1 (top2, top3)-x, y, z, bridge1 (bridge2, bridge3)-x, y, z, and hollow1 (hollow2, hollow3, hollow4, hollow5, hollow6)-x, y, z were represented. For optimization, the three kinds of top-x and bridge-x adsorption states with the CO_2 molecule recumbent (laying) on the surface were stable (Figure 2a,c). The recumbent orientation represented a configuration with one C and two O atoms of CO_2 forming bonds with the surface. The end-down orientation represented a configuration in which one oxygen atom of CO_2 formed a bond with the surface (Figure 2b,d,e). The adsorption sites of the end-down configuration were all of the three kinds of the top-z, bridge-z, and six kinds of hollow-z sites after geometry optimization, respectively. The O−C−O bond of adsorbed CO_2 molecules on all six kinds of hollow-z site had an angle with the kaolinite (001) surface.

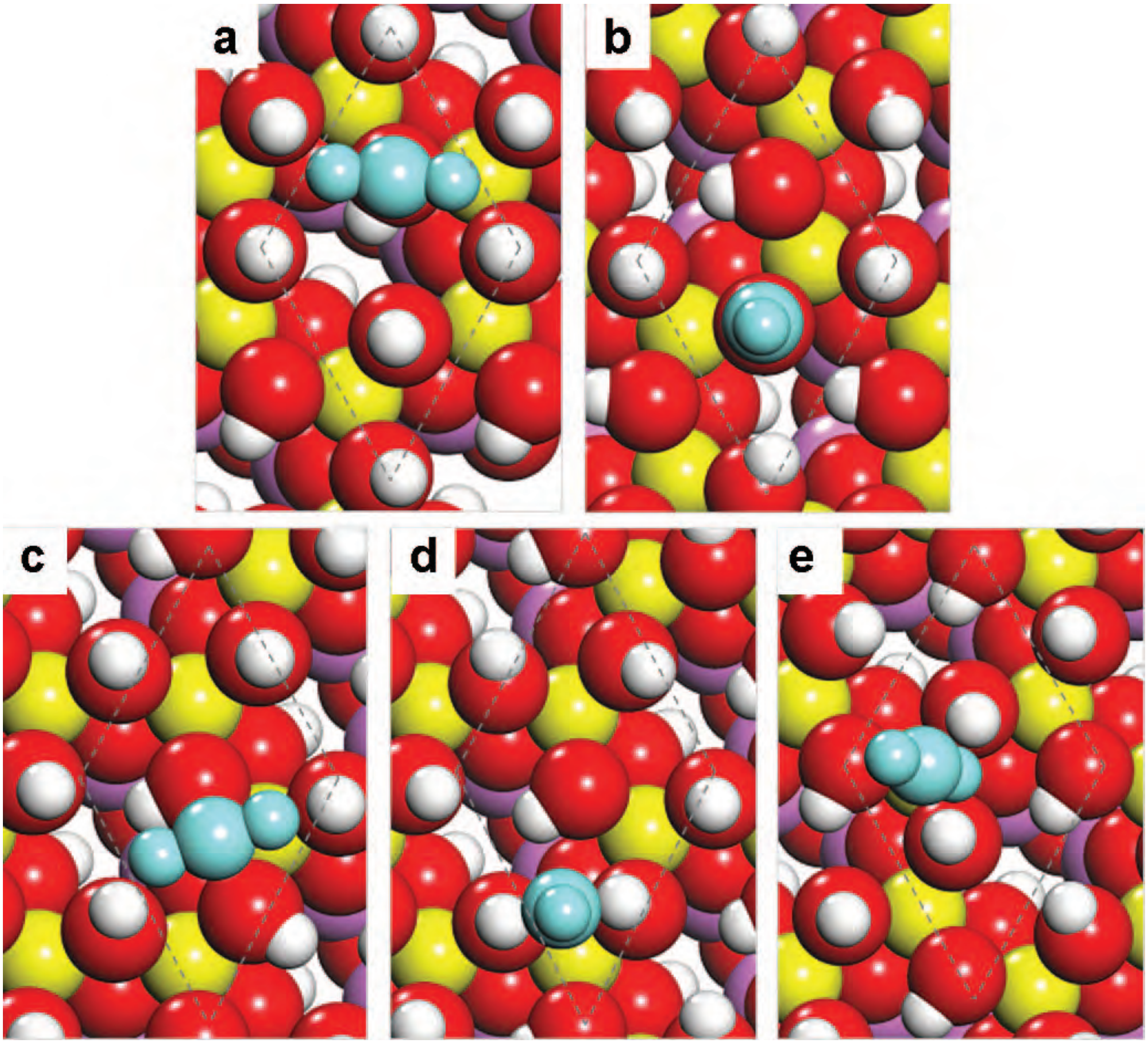

Figure 2. Top view of CO_2 molecule adsorbed on the (a) top-x, (b) top-z, (c) bridge-x, (d) bridge-z, and (e) hollow-z sites of kaolinite (001). The adsorbed CO_2 molecule is shown in blue for clarity.

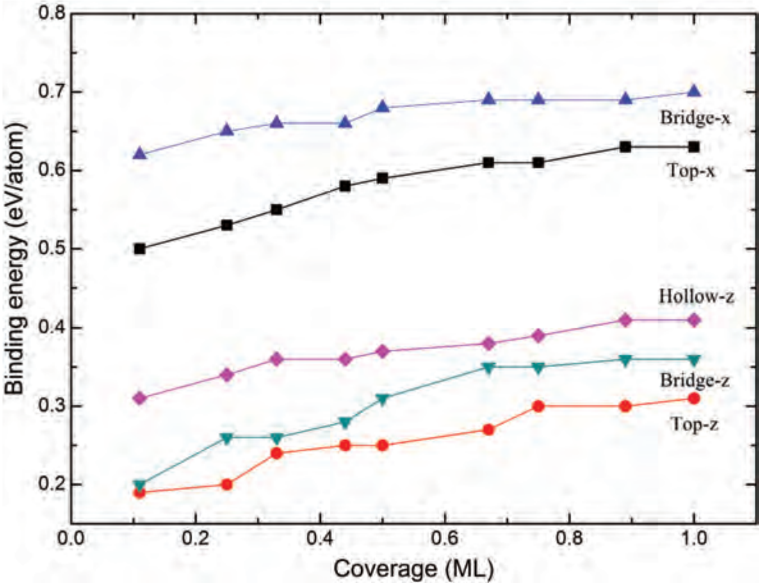

Figure 3. Calculated adsorption energy, E_{ads}, of the CO_2/kaolinite (001) system *vs*. the coverage for the CO_2 molecule adsorption in different sites. The solid lines connecting the calculated adsorption energies are used as visual guides.

Meanwhile, all three kinds of top-x, bridge-x, top-z, bridge-z, and six kinds of hollow-z adsorption sites for CO_2 molecules had similar adsorption energies in the coverage regime $0<\Theta\leqslant 1.0$. The calculated adsorption energies, E_{ads}, of CO_2 on these five kinds of surface sites with respect to the free molecule CO_2 are illustrated (Figure 3) and summarized (Table 1) for different CO_2 coverage in the regime $0<\Theta\leqslant 1.0$. The calculated adsorption energies (Figure 3) revealed that the x orientation adsorption was always greater than for the z orientation adsorption. For the x orientation adsorption, the bridge-x site was more stable than the top-x site while for the z orientation adsorption, the hollow-z was more favorable than the bridge-z and top-z sites in the coverage regime $0<\Theta\leqslant 1.0$. Meanwhile, the quantity for top-x, top-z, bridge-x, bridge-z, and hollow-z adsorption displayed a modestly increasing tendency with the CO_2 coverage (Figure 3), while the overall variation in the magnitude of E_{ads} was rather small in the range of coverage. The increasing adsorption with coverage indicated a significant attraction between the on-surface CO_2 molecules and implied a tendency to form CO_2 islands or clusters on the kaolinite (001) surface at $0<\Theta\leqslant 1.0$. In addition, the adsorption-energy difference between the top-x and bridge-x sites, as well as among the top-z, bridge-z, and hollow-z, displayed a notable increase with CO_2 coverage, which implied a substrate-induced anisotropy in the CO_2–solid chemical bonding.

Calculated geometries for CO_2-molecule adsorption on top-x, top-z, bridge-x, bridge-z, and hollow-z sites of kaolinite (001) at $\Theta = 0.25$, 0.5, 0.75, and 1.0, including the C–O bond lengths, d_{C-O} (Å), and bond angles, ∠OCO (°), are listed in Table 2. In the first row of that table, the calculated values for a gaseous CO_2 molecule are listed for comparison. For all the adsorption sites, the two C–O bond lengths, d_{C-O1} and d_{C-O2}, varied little around 1.17 Å with increasing Θ values. The values of the O–C–O internal angle (∠OCO) for all five types of adsorption sites decreased with increasing Θ. Compared with the gas-phase value, ∠OCO on the top-z and bridge-z sites decreased by 11° and 7° from 180°, respectively, while on the top-x, bridge-x, and hollow-z, ∠OCO varied little around 180°. For different CO_2 coverage values, Θ, the height, h_{CO_2-H}, of adsorbate CO_2 above the surface

Table 1. The calculated adsorption energy, E_{ads} (eV), as a function of molecular CO_2 coverage on the different sites of kaolinite (001).

Site	ML0.11	ML0.25	ML0.33	ML0.44	ML0.5	ML0.67	ML0.75	ML0.89	ML1.0
Top-x	0.50	0.53	0.55	0.58	0.59	0.61	0.61	0.63	0.63
Top-z	0.19	0.20	0.24	0.25	0.25	0.27	0.30	0.30	0.31
Bridge-x	0.62	0.65	0.66	0.66	0.68	0.69	0.69	0.69	0.70
Bridge-z	0.20	0.26	0.26	0.28	0.31	0.35	0.35	0.36	0.36
Hollow-z	0.31	0.34	0.36	0.36	0.37	0.38	0.39	0.41	0.41

Table 2. The calculated geometries for the CO_2 molecule adsorption on top-x, top-z, bridge-x, bridge-z, and hollow-z sites of kaolinite (001). The C−O bond lengths d_{C-O} (Å) and bond angles (∠OCO) (º) of CO_2 molecules are listed. The first row lists the calculated values for a gaseous CO_2 molecule for comparison.

Site	d_{C-O1} (Å)				d_{C-O2} (Å)				∠OCO			
	Ml0.25	Ml0.5	Ml0.75	Ml1.0	Ml0.25	Ml0.5	Ml0.75	Ml1.0	Ml0.25	Ml0.5	Ml0.75	Ml1.0
Free	1.16	1.16	1.16	1.16	1.16	1.16	1.16	1.16	180.0	180.0	180.0	180.0
Top-x	1.17	1.17	1.17	1.17	1.16	1.16	1.16	1.16	179.9	179.7	179.7	179.5
Top-z	1.18	1.18	1.18	1.17	1.18	1.18	1.17	1.17	169.1	168.1	168.0	171.2
Bridge-x	1.17	1.17	1.17	1.17	1.16	1.16	1.16	1.16	179.9	179.7	179.9	179.3
Bridge-z	1.17	1. 17	1.17	1.17	1.17	1.17	1.17	1.17	172.5	171.9	171.9	172.1
Hollow-z	1.17	1.17	1.17	1.17	1.17	1.16	1.16	1.16	179.9	179.6	179.2	179.2

and the topmost interlayer relaxation Δd_{12} with CO_2 in the top-x, bridge-x, top-z, bridge-z, and hollow-z sites are summarized in Table 3. The Δd_{12} value was calculated according to the equation $\Delta d_{12} = (d_{12}-d_0)/d_0$, where d_{12} and d_0 were the depth between the first and second layers of the relaxed surface and the corresponding depth between the first and second layers of the clean kaolinite (001) surface, respectively. The calculated results showed that the adsorption of CO_2 on kaolinite (001) induced notable changes in the interlayer distance of the substrate. In particular, for the top-x, top-z, bridge-z, and hollow-z adsorption, the value of Δd_{12} was negative and decreased with CO_2 coverage, which meant that the distance between the topmost two atomic layers of the kaolinite (001) surface had contracted with increasing CO_2 coverage. On the contrary, for bridge-x adsorption, the value of Δd_{12} was negative from −7.63% to −14.06% in the coverage regime $0.11 \leqslant \Theta \leqslant 1.0$, which meant the topmost interlayer had also contracted but became smaller with increasing CO_2 coverage. These changes reflected the strong influence of the CO_2 adsorbates on the neighboring O atoms and, thus, resulted from significant redistribution of the electronic structure. The results verified that CO_2 adsorption caused the outermost kaolinite (001) layer separation to relax back to something close to its 'ideal' bulk value. With respect to the height h_{CO_2-H} of adsorbate CO_2 above the surface, the results showed (Table 3) that, for all five types of adsorption sites, the values of h_{CO_2-H} decreased with increasing Θ. The short height h_{CO_2-H} implied a strong interaction between the CO_2 and kaolinite surfaces. Note that the bridge-x site was slightly shorter than the other four types of sites, consistent with the fact that the bridge-x site was the most stable.

To gain more insight into the precise nature of the chemisorbed molecular state in the CO_2/kaolinite (001) system, the electronic partial density of state (PDOS) of the CO_2 molecule and the neighboring O atoms were calculated. The results were analyzed by means of the electron density difference $\Delta\rho(r)$ which was obtained by subtracting the electron densities of non-interacting component systems, $\rho^{\text{kaolinite (001)}}(r) + \rho CO_2(r)$, from the density $\rho(r)$ of the CO_2/kaolinite (001) system, while retaining the atomic positions of the component system at the same location as in CO_2/kaolinite (001). Positive (blue) $\rho(r)$ indicated an accumulation of electron density upon binding, while a negative (yellow) corresponded to electron-density depletion. As a typical example, the PDOS for the two kinds of stable adsorption configuration of top-z and bridge-x were plotted (Figure 4); the electron-density differences are shown in Figure 4b,f (insets). For comparison, the PDOS of the free CO_2 molecule and the neighboring O atoms of clean kaolinite (001) were also calculated. After CO_2-molecule adsorption on the top-z site of kaolinite (001), the 3σ, 4σ, 1π, 5σ bonding, and 2π antibonding orbitals of CO_2 shifted down in energy by 3.70, 3.53, 3.85, 3.55, and 3.85 eV, respectively. Furthermore, the amplitudes of all bonding and antibonding orbitals were much weaker than those in

Table 3. The calculated adsorbate height (h_{C-O}) and the interlayer relaxation (Δd_{12}) for different coverage of atomic CO_2 adsorption on the kaolinite (001) surface.

Coverage Θ	h_{C-O}				Δd_{12} (%)			
	0.25 ML	0.5 ML	0.75 ML	1.0 ML	0.25 ML	0.5 ML	0.75 ML	1.0 ML
Top-x	2.13	2.13	2.08	2.03	−6.01	−5.38	−4.84	−4.63
Top-z	4.02	3.83	3.64	3.51	−7.77	−6.83	−6.53	−5.89
Bridge-x	2.29	2.27	2.27	2.26	−7.63	−10.62	−10.62	−14.06
Bridge-z	3.79	3.64	3.49	3.31	−7.13	−6.20	−5.19	−4.93
Hollow-z	3.78	3.49	3.26	3.12	−7.14	−6.34	−5.87	−5.64

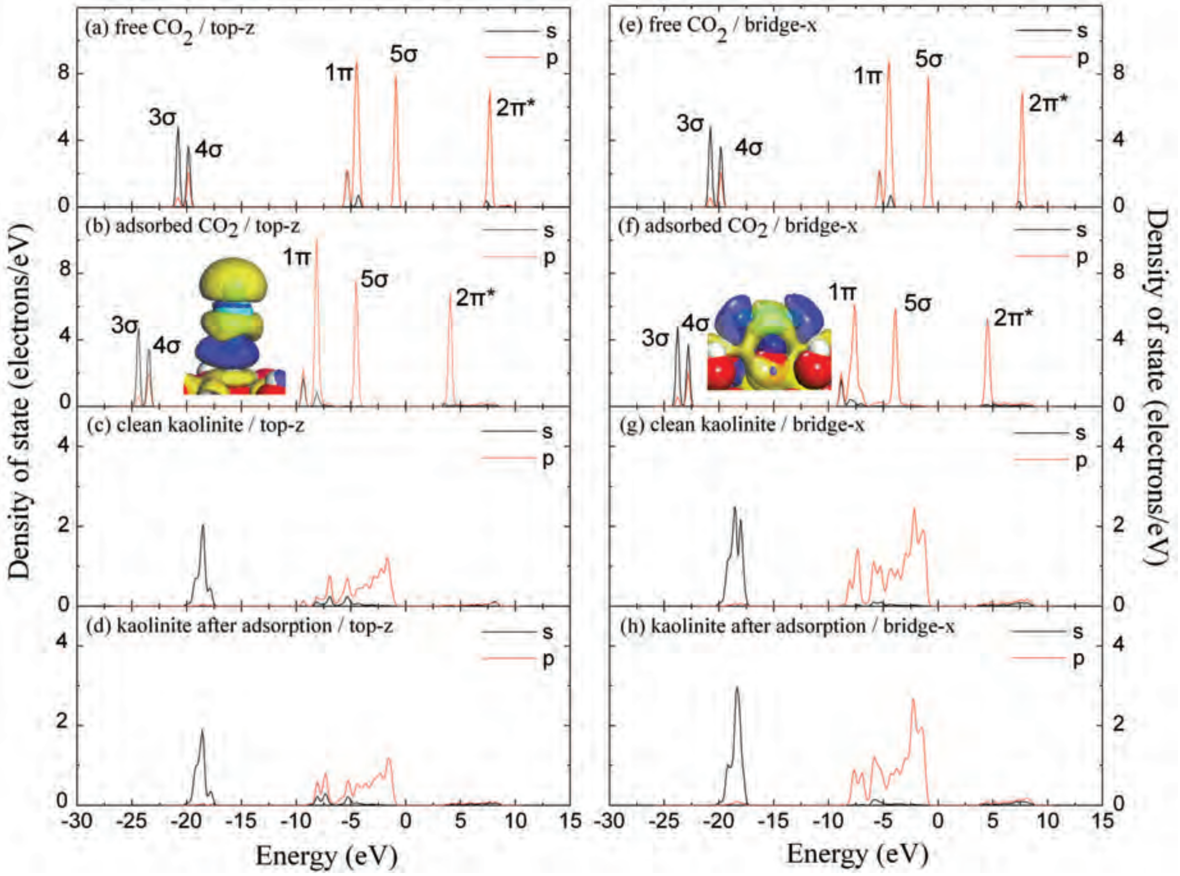

Figure 4. The PDOS plots for the CO_2 molecule and the neighboring O atoms bonded to CO_2 at the stable top-z and bridge-x adsorption sites on surface: (a,b) free and adsorbed CO_2 molecule at the stable top-z adsorption site; (c,d) clean and adsorbed kaolinite (001) surface at the stable top-z adsorption site; (e,f) free and adsorbed CO_2 molecule at the stable bridge-x adsorption site; (g,h) clean and adsorbed kaolinite (001) surface at the stable bridge-x adsorption site. The insets show the side view of electron density difference for the CO_2 atom at the stable (b) top-z and (f) bridge-x adsorption sites. The Fermi energy is set at zero.

the free CO_2. These features were essentially caused by the different electronegativities of kaolinite and CO_2 molecules, which induced charge redistribution and thus built a global electrostatic attraction between the CO_2 and neighboring O atoms. The result was substantiated by the 3D electron density difference. A large charge accumulation existed between the adsorbate and substrate; an O–O bond was formed, which donated electrons from a neighboring surface O atom to the CO_2 molecule. The PDOS for the most stable adsorption configuration of bridge-x was calculated (Figure 4e,h). The bonding and antibonding orbitals of the CO_2 molecule were shifted to a much lower energy and the amplitudes of 1π bonding and 2π antibonding were weaker than those in free CO_2 molecules, even in the adsorbed CO_2 on the top-z site. The sp electronic states of adsorbed CO_2, in particular, expanded in energy compared with free CO_2 and the adsorbed CO_2 on the top-z site. The overlap in energy between adsorbed CO_2 and neighboring O atoms of kaolinite (001) surface electrons ranged from −9.15 eV to −3.46 eV. From the 3D electron-density difference (Figure 4h, inset), one C–O and two H–O bonds were formed, among which two donate electrons from surface H atoms to the O atoms of the CO_2 molecule and donated electrons from the C atom of the CO_2 molecule to neighboring surface O atoms. These results illustrated that the bridge-x adsorption site was more stable than the top-z adsorption site for CO_2 molecules.

The orbital-resolved PDOS for CO_2 adsorption on the bridge-x site, and the neighboring O and H atoms at $\Theta = 0.11$ and $\Theta = 1.0$, are shown in Figures 5a and 5b, respectively. The Fermi energy was set at zero. At low coverage ($\Theta = 0.11$), the narrow, low-amplitude peak at ~−7.92 eV was denoted the 'CO_2 p state' (Figure 5a), which was largely hybridized with the p state of the neighboring O atoms; the hybridization between CO_2 p and O sp states was negligible. With increasing CO_2 coverage (Figure 5b for $\Theta = 1.0$ ML), three prominent changes involving the C–O chemical bonding occurred: (1) the peaks in the CO_2 3σ, 4σ, 1π, 5σ bonding, and 2π antibonding shifted down in energy; the amplitudes of all

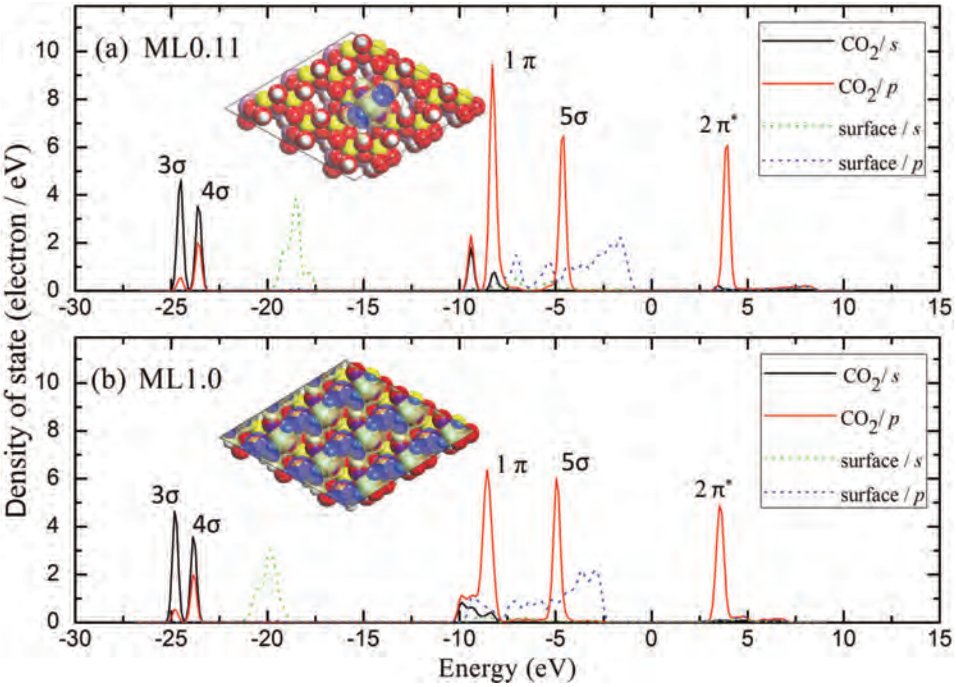

Figure 5. The PDOS for the bridge-x adsorption site on surface CO_2 molecules and the neighboring O atoms at (a) $\Theta = 0.11$ and (b) $\Theta = 1.0$ where the inset shows the top view of electron density difference for CO_2 atoms at $\Theta = 0.11$ and $\Theta = 1.0$, respectively. The Fermi energy is set at zero.

bonding and antibonding orbitals were much weaker than those in the case of $\Theta = 0.11$ ML. (2) Compared to the case where $\Theta = 0.11$ ML, the hybridization of CO_2 p and surface O p states was distinctly enhanced in the case of $\Theta = 1.0$ ML. The change in the CO_2 p PDOS was due to the fact that at high coverage for $\Theta = 1.0$ ML, the CO_2 adatom was highly coordinated, which drove the CO_2 p state to bond not only with the s states but also the p states of the O and H atoms. Because the O sp states lay mainly in the interior of the valence band, the CO_2 p state thus had to shift down in energy in order to overlap with the O p states. In particular, the main peak around $E = -8.6$ eV in the CO_2 p PDOS in Figure 5b was a result of the hybridization between CO_2 p states and O sp states. (3) The small CO_2 peak at -9.36 eV tended to vanish due to a large weight transfer of these states to a higher energy, caused by the formation of bonding states between CO_2 p and O p orbitals. This was most notable for surface O p states. In fact, in the $-9.7<E<-7.9$ eV energy interval (Figure 5b), a large number of surface O p states were empty in this energy region at low CO_2 coverage (Figure 5a) of the kaolinite (001) surface. The empty O p states will gain energy, which will overcompensate the energy lost by elevation of the CO_2 p state when adsorbed CO_2 coverage is increased. A top view of the electron density difference between CO_2 atoms at $\Theta = 0.11$ and $\Theta = 1.0$ (Figures 5a and 5b) reveals that the charge redistribution was mainly at the surface and involved the adsorbed CO_2 molecule and the topmost O atoms. The results further revealed that upon adsorption, electrons flowed from the O p state into the CO_2 p state, resulting in a depletion of the surface electrons. With increasing CO_2 coverage, more surface O sp electrons transferred to the localized CO_2 1π and 5σ orbitals, suggesting that the covalent character of the O–O bonding increased with CO_2 coverage (Figure 5b, inset).

SUMMARY

The adsorption of CO_2 molecules on the kaolinite (001) surface were investigated systematically using first-principles DFT-LDA calculations. A wide range of coverage from 0.11 to 1.0 ML was considered using different surface models [*i.e.* $p\ (3 \times 3)$ and $p\ (2 \times 2)$ surface unit cells] for adsorption in the surface top-x, top-z, bridge-x, bridge-z, and hollow-z sites. In the coverage range of $0<\Theta<1.0$, the most stable among all possible pure adsorbed sites was the bridge-x site, followed by the top-x, hollow-z, bridge-z, and top-z sites. The atomic geometry, the charge-density distribution, and the electronic structure upon the adsorbed CO_2 was also studied, which showed consistently the fundamental influence of covalent bonding between the CO_2 molecule and surface O atoms. Remarkably, this influence on the energy increased with increasing the CO_2 coverage. The increase in the CO_2 adsorption energy for all five types of sites with Θ in the coverage range $0<\Theta\leqslant 1.0$ implied the effective attraction between the CO_2 adsorbates and kaolinite (001) surface, making it favorable for the formation of CO_2 islands or clusters.

ACKNOWLEDGMENTS

The present research was supported by the Program for Changjiang Scholars and Innovative Research Team in the University of China under Grant No. IRT0656, and by the National Natural Science Foundation of China (Nos 40972196 and 41172263).

REFERENCES

Adams, J.M. (1983) Hydrogen atom position in kaolinite by neutron profile refinement. *Clays and Clay Minerals*, **31**, 352−358.

Araki, S., Kiyohara, Y., Tanaka, S., and Miyake, Y. (2012) Adsorption of carbon dioxide and nitrogen on zeolite rho prepared by hydrothermal synthesis using 18-crown-6 ether. *Journal of Colloid and Interface Science*, **388**, 185−190.

Aspelund, A. and Jordal, K. (2007) Gas conditioning – the interface between CO_2 capture and transport. *Greenhouse Gas Control I*, 343−354.

Baltrusaitis, J., Schuttlefield, J., Zeitler, E., and Grassian, V.H. (2011) Carbon dioxide adsorption on oxide nanoparticle surface. *Chemical Engineering Journal*, **170**, 471−481.

Benco, L., Tunega, D., Hafner, J., and Lischka, H. (2001) Orientation of OH groups in kaolinite and dickite: *ab initio* molecular dynamics study. *American Mineralogist*, **86**, 1057−1065.

Bish, D.L. (1993) Rietveld refinement of the kaolinite structure at 1.5 K. *Clays and Clay Minerals*, **41**, 738−744.

Blöchl, P.E. (1994) Projector augmented-wave method. *Physical Review B*, **50**, 17953−17979.

Choe, S.J., Kang, H.J., Park, D.H., Huh, D.S., and Park, J. (2001) Adsorption and dissociation reaction of carbon dioxide on Ni(111) surface: Molecular orbital study. *Applied Surface Science*, **181**, 265−276.

Do, D.D. and Do, H.D. (2006) Effects of potential models on the adsorption of carbon dioxide on graphitized thermal carbon black: GCMC computer simulations. *Colloids and Surface A*, **277**, 239−248.

Giese, R.F., JR. (1973) Interlayer bonding in kaolinite dickite and nacrite. *Clays and Clay Minerals*, **21**, 145−149.

Hayashi, S. (1997) NMR study of dynamics and evolution of guest molecules in kaolinite/dimethyl sulfoxide intercalation compound. *Clays and Clay Minerals*, **45**, 724−732.

He, M.C., Sousa, L.R., Elsworth, D., and Vargas, E. Jr., editors (2012) *CO_2 Storage in Carboniferous Formations and Abandoned Coal Mines*. CRC Press, Oxford, UK, pp. 1−68.

Hess, A.C. and Saunders, V.R. (1992) Periodic ab initio Hartree-Fock calculation of the low-symmetry mineral kaolinite. *The Journal of Physical Chemistry*, **11**, 4367−4374.

Hobbs, J.D., Cygan, R.T., Nagy, K.L., Schultz, P.A., and Sears, M.P. (1997) All-atom *ab initio* energy minimization of the kaolinite crystal structure. *American Mineralogist*, **82**, 657−662.

Hu, X.L. and Angelos, M. (2008) Water on the hydroxylated (001) surface of kaolinite: From monomer adsorption to a flat 2D wetting layer. *Surface Science*, **602**, 960−974.

Kaya, Y. (1995) The role of CO_2 removal and disposal. *Energy Conversion and Management*, **6–9**, 375−380.

Ketzer, J.M., Iglesias, R., Einloft, S., Dullius, J., Ligabue, R., and Lima, V.D. (2009) Water-rock-CO_2 interactions in saline aquifers aimed for carbon dioxide storage: Experimental and numerical modeling studies of the Rio Bonito Formation (Permian), southern Brazil. *Applied Geochemistry*, **24**, 760−767.

Kresse, G. and Furthmuller, J. (1996) Efficient iterative schemes for ab initio total-energy calculations using a plane-wave basis set. *Physical Review B*, **54**, 11169−11173.

Kresse, G. and Joubert, J. (1999) From ultrasoft pseudopotentials to the projector augmented-wave method. *Physical Review B*, **59**, 1758−1762.

Li, L., Zhao, N., Wei, W., and Sun, Y.H. (2013) A review of research progress on CO_2 capture, storage, and utilization in Chinese Academy of Sciences. *Fuel*, **108**, 112−130.

Lopez-Carreno, L.D., Heras, J.M., and Viscido, L. (1997) Adsorption and dissociation of CO_2 on polycrystalline Mo. *Surface Science*, **377−379**, 615−618.

Luis, P., Gerven, T.V., and Bruggen, B.V. (2012) Recent developments in membrane-based technologies for CO_2 capture. *Progress in Energy and Combustion Science*, **38**, 419−448.

Monkhorst, H.J. and Pack, J.D. (1976) Special points for Brillouin-zone integrations. *Physical Review B*, **13**, 5188−5192.

Plançon, A., Giese, R.F. Jr., Snyder, R., Drits, V.A., and Bookin, A.S. (1997) Stacking faults in the kaolinite-group minerals: defect structures of kaolinite. *Clays and Clay Minerals*, **37**, 195−198.

Sato, H., Ono, K., Johnston, C.T., and Yamagishi, A. (2005) First-principles studies on the elastic constants of a 1:1 layered kaolinite mineral. *American Mineralogist*, **90**, 1824−1826.

Smykowski, D., Szyja, B., and Szczygiel, J. (2013) DFT modeling of CO_2 adsorption on Cu, Zn, Ni, Pd/DOH Zeolite. *Journal of Molecular Graphics and Modelling*, **41**, 89−96.

Šolc, R., Gerzabek, M.H., Lischka, H., and Tunega, D. (2011) Wettability of kaolinite (001) surfaces – Molecular dynamics study. *Geoderma*, **169**, 47−54.

Teppen, B.J., Rasmussen, K., Bertsch, P.M., Miller, D.M., and Schäfer, L. (1997) Molecular dynamics modeling of clay minerals. 1. Gibbsite, kaolinite, pyrophyllite, and beidellite. *The Journal of Physical Chemistry B*, **101**, 1579−1587.

Venaruzzo, J.L., Volzone, C., Rueda, M.L., and Ortida, J. (2002) Modified bentonitic clay minerals as adsorbents of CO, CO_2, and SO_2 gases. *Microporous and Mesoporous Materials*, **56**, 73−80.

Volzone, C. (2007) Retention of pollutant gases: comparison between clay minerals and their modified products. *Applied Clay Science*, **36**, 191−196.

Waldo, P. (2011) Clay minerals, carbon storage, and effects of observational scale on computational models. *Applied Clay Science*, **78**, 4059−4062.

Wood, B.C., Bhide, S.Y., Dutta, D., Kandagal, V.S., Pathak, A.D., Punnathanam, S.N., Ayappa, K.G., and Narasimhan, S. (2012) Methane and carbon dioxide adsorption on edge functionalized graphene: A comparative DFT study. *The Journal of Chemical Physics*, **137**, 054702.

Xu, T.F., Apps, J.A., and Pruess, K. (2005) Mineral sequestration of carbon dioxide in a sandstone-shale system. *Chemical Geology*, **217**, 295−318.

(*Received 18 April 2013; revised 26 May 2014; Ms. 761; AE: J.W. Stucki*)